Investigating the chemistry of stars in the Large Magellanic Cloud

Wei Shen Oh

A thesis submitted for the degree of

Doctor of Philosophy

The Australian National University

Research School of Astronomy & Astrophysics

Australian National University

January 2024

When I consider your heavens,
the work of your fingers,
the moon and the stars,
which you have set in place,
what is mankind that you are mindful of them,
human beings that you care for them?

Psalms 8:3-4 (NIV)

Disclaimer

I hereby declare that the work undertaken in this thesis has been conducted by me alone, except where indicated in the text. I conducted this work between March 2020 and December 2023, during which period I was a PhD student at the Australian National University. This thesis, in whole or any part of it, has not been submitted to this or any other university for a degree.

This thesis has been compiled as a Thesis by Compilation in accordance with relevant ANU policies. Chapters 4 and 5 in this thesis have been published in peer reviewed journals, while Chapter 6 is currently under review. I have made significant contribution to each of these journal articles and have written the text of the papers myself, except where indicated otherwise.

Wei Shen Oh

1 January 2024

Acknowledgements

Firstly, I would like to thank my supervisors, Thomas Nordlander, Gary Da Costa, and Dougal Mackey, for their guidance and support throughout the past 3.5 years of my PhD. I really learnt a lot from all the meetings that we had, not just in terms of Galactic Archaeology but also in terms of general skills, like different ways of approaching a problem and how to write or present things clearly and concisely. It has been a memorable experience being supervised by them and I can't ask for anything more.

I also want to thank other people who have helped me greatly in my research, in one way or another. Some examples are Professor Mike Bessell, who helped me with the spectrophotometric analysis of the WiFeS spectra, Dr. Chris Onken who provided me with an important plot for my EMP study, Madeleine McKenzie who taught me how to fit equivalent widths and Dr. David Yong, who taught me how to use MOOG to measure chemical abundances. Thank you all so much for this.

And finally, a big thank you to my family, including my fiancé Lily, for their unwavering support and care. I want to also thank my parents especially for being fully supportive of my decision to study astronomy in University, and not forcing me to study medicine, law or engineering, which are more common and traditional fields to pursue in Singapore. To my mum, thank you so much for giving me an opportunity to learn about all things in space even when I was as young as 9 or 10, by buying books and telescopes for me, or by bringing me to Astro camps. I hope I have made you proud by reaching the tail end of my PhD program in Astrophysics.

This research was supported by the Australian Research Council Centre of Excellence for All Sky Astrophysics in 3 Dimensions (ASTRO 3D), through project number CE170100013.

Abstract

The Large Magellanic Cloud (LMC) is one of the Milky Way's most prominent dwarf galaxy satellites. Positioned within the Milky Way's gravitational influence, the LMC offers a unique opportunity to explore near-field cosmology in the context of stellar evolution, star formation, interstellar medium behaviour, and galaxy evolution. This thesis presents detailed abundance measurements for various elements in stars within the LMC, shedding light on their chemical composition and evolution.

The first study presents a search for multiple populations in a 1.95 Gyr old LMC star cluster NGC 1846, which is a direct test of the 2 Gyr minimum boundary for the age of massive star clusters exhibiting chemical abundance spread. High-resolution VLT/FLAMES spectra, complemented by HST photometric data and non-local thermodynamic equilibrium corrections, reveal a lack of intrinsic star-to-star spread in Na and O abundances, implying no evidence of multiple populations in NGC 1846. However, a significant spread in carbon abundances indicates varying evolutionary mixing on the red giant branch. This work enhances our understanding of the existence of multiple populations in intermediate-age massive star clusters in galaxies.

The second study presents a search for extremely metal-poor (EMP) stars in the LMC, crucial for unraveling information about the earliest stars and conditions during the initial stages of star formation in dwarf galaxies. Utilising photometric data from SkyMapper DR3 and kinematic data from Gaia DR2, a selection of EMP candidates was made using various photometric and kinematic cuts. A low-resolution spectroscopic follow-up observation was done using ANU 2.3/WiFeS. The study identifies seven stars with [Fe/H] $\leq$ –2.75, including two with [Fe/H] $\leq$ –3. The radial velocities of these stars are consistent with the LMC's outer rotation curve, firmly establishing them as members of the LMC. These stars represent the most metal-poor stars discovered in the LMC to date.

The third study delves into detailed abundance results for the seven LMC stars mentioned in the previous study. Based on UVES high dispersion spectra, the stars are confirmed as the most metal-poor stars ever found in the Magellanic Clouds. While their element abundance ratios are generally consistent with Milky Way halo stars of similar [Fe/H], only two of the more metal-rich stars in the sample exhibit enhancements in r-process elements. The absence of r-process enrichment in stars with lower [Fe/H] values implies a minimum timescale of $\sim$100 Myr for the neutron star binary merger process to generate substantial r-process enhancements in the

LMC. We find that the occurrence rate of r-process enhancement (r-I or r-II) in our sample of very and extremely metal-poor stars is statistically indistinguishable from that found in the Milky Way's halo, although including stars from the Reggiani et al. (2021) sample hints at a larger r-II frequency the LMC. Overall, our results shed light on the earliest epochs of star formation in the LMC that may be applicable to other galaxies of LMC-like mass.

Together, these studies contribute valuable insights into the chemical composition, evolutionary history, and early star formation processes within the LMC, advancing our understanding of stellar and galactic evolution.

Contents

List of Figures

List of Tables

Chapter 1

Introduction

1.1 Galaxy formation and dwarf galaxies

Galaxy formation and evolution is a key research topic in modern astrophysics. The quest to understand where galaxies come from and how they change over time has a rich history that dates back to the 18th century. The famous German philosopher, Immanuel Kant, first suggested in his work "The Universal Natural History and Theories of the Heavens" (1755), that galaxies formed when clouds of gas and dust collapsed under the force of gravity. For nearly two centuries, many believed that galaxies emerged from solitary, uniform structures. This idea gained support when Eggen et al. (1962) studied the movements of stars in our Milky Way and found evidence that seemed to support the idea of a single, grand collapse event. In this picture, chemical enrichment due to stellar formation and evolution should result in a metallicity gradient encoded in the stellar component that condensed out of the contracting gas cloud. Both the mean metal abundance and its range should drop as we move into the outskirts of the galaxy. However, a significant challenge to this view emerged from the work of Searle & Zinn (1978). By studying globular clusters in the outer parts of our Milky Way (> 8 kpc from the galactic centre), instead of obtaining the expected metallicity gradient pattern, they found that the abundance of metals in these clusters did not change much with their distance from the centre of the galaxy.

Since then, astronomers have made great efforts to create detailed models of how galaxies form and evolve. Computer simulations like Illustris, EAGLE, and FIRE (Nelson et al. 2015; McAlpine et al. 2016; Chan et al. 2015) have been used to explore the processes that shape galaxies. Most astronomers now believe that large galaxies like the Milky Way are formed through a combination of mergers with other galaxies, the addition of smaller subsystems, and the gradual accumulation of gas from the space between galaxies (White & Rees 1978; White & Frenk 1991). This view fits well with the prevailing theory known as the Λ Cold Dark Matter

(ΛCDM) cosmological model (Primack 1984). In this model, dark matter halos, which are invisible but have mass, grow by gathering material from smaller halos. The ΛCDM model has become a fundamental part of modern cosmology, helping us understand how the universe's structure forms and how galaxies like the Milky Way behave.

One critical way of constraining and testing these models is by studying galaxies other than our Milky Way. The main advantage of this method is the ability to get improved statistics from a larger sample size. It also removes tricky line-of-sight projection and extinction effects (i.e. differential reddening) which must be taken into account for our own Galaxy. Although high redshift galaxies can be studied in terms of global properties and degree of variation in large statistically robust samples, their great distances mean that we can only obtain very crude information about individual objects, meaning that the fundamental properties of their stellar populations, such as metal abundances and ages, are often poorly constrained.

In contrast, for the local universe, although the number of nearby galaxies located within is relatively small, it offers an ideal channel for understanding galaxy formation and evolution because they provide concrete endpoints of the evolutionary process that can be studied in exquisite detail. In line with that, we are fortunate to be located in the Local Group, which is a galaxy group consisting of two giant galaxies (our Milky Way and the Andromeda Galaxy), each with its own retinue of smaller dwarf satellites, plus a handful of more isolated dwarf systems. Altogether, the Local Group has a diameter of $\sim$ 3 Mpc and a total mass of 2–5 $\times$ $10^{12} M_{\odot}$, and comprises at least 100 galaxies (McConnachie 2012). These constitute probes of a wide range of masses and environments. With current technology such as the Advanced Camera for Surveys (ACS) and Wide Field Camera 3 (WFC3) found on the Hubble Space Telescope (HST), and the UVES spectrograph on the Very Large Telescope (VLT), we are able to get precise photometric and spectroscopic measurements on a star-by-star basis. This has allowed us to categorise their diverse stellar populations by expanding our knowledge of stellar mass and kinematics, and elemental abundances for other galaxies such as M31 and M33 (Shetrone et al. 2003; Williams et al. 2009; Johnson et al. 2017).

A particular subset of nearby galaxies that we want to understand better are dwarf galaxies. For the past few decades, detailed observations of dwarf galaxies have been essential for astronomers to test various theories in near-field cosmology. This is because dwarf galaxies are the most common type of galaxy in the universe, and therefore a critical ingredient in any galaxy formation model. Specifically, the dwarf galaxies orbiting our Milky Way are a valuable source of information. They serve

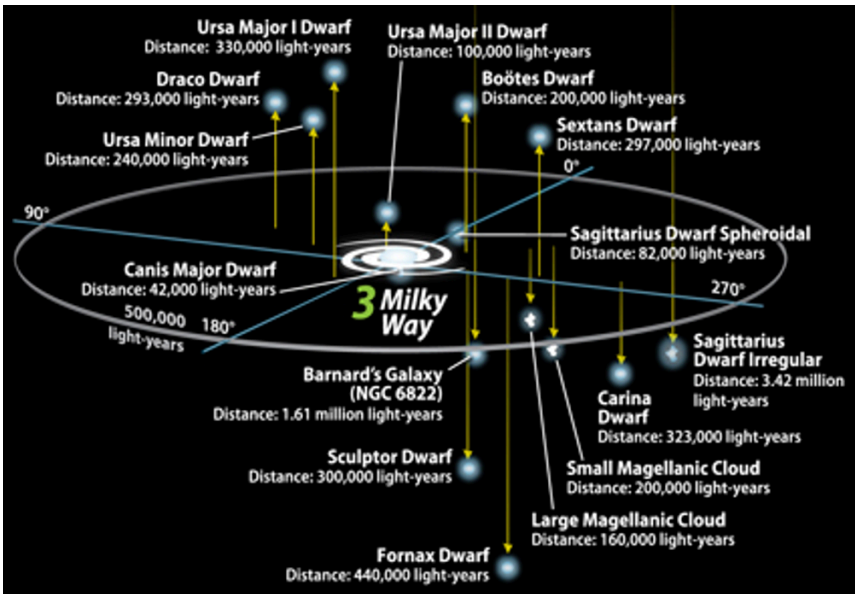

Figure 1.1: Map illustrating the spatial distribution of nearby dwarf galaxies within the Local Group, situated near the Milky Way.
Image Credit: Astronomy Magazine/Roen Kelly

as remnants of ancient galaxy formation processes, enriched with insights into the events that shaped the expansive dark matter halo surrounding our galaxy (e.g., Kallivayalil et al. 2018).

One notable example of such an event is the Sagittarius Dwarf Spheroidal Galaxy, an elliptical satellite galaxy that is being partially absorbed by the Milky Way (Ibata et al. 1994). As the much larger Milky Way exerts its gravitational influence on the Sagittarius Dwarf Galaxy, the smaller dwarf galaxy gradually disintegrates, leaving behind a trail of stars known as the Sagittarius Stream. This galactic cannibalism event has left lasting imprints on the Milky Way, revealing our galaxy's complex formation history through its disrupted stars. N-body simulations have shown how the Sagittarius dwarf galaxy is tidally disrupted, which has resulted in better estimates for its motion and mass (Law & Majewski 2010; Martínez-Barbosa & Casas 2011; Bennett et al. 2022).

Dwarf galaxies also offer valuable insights into galaxy formation processes, which can be studied by examining the chemical compositions of their metal-poor population. These stars, characterised by their low metallicities and old ages, provide valuable clues about the early stages of galaxy formation and the underlying physical processes governing stellar evolution. More information on this class of objects will be covered in Chapter 3. Venn et al. (2012) showed that there is strong evidence for inhomogeneous mixing in the Carina dwarf galaxy based on its metal-poor population, indicating a poor statistical sampling of supernova contributions during

star formation. Notably, a significant dispersion in [Mg/Fe], which represents the logarithm of the ratio of the abundance of Mg to that of Fe, pointed to poor mixing in the metal-poor population, while a disparity in [α/Fe] ratios between the old and intermediate-aged populations indicates that the latter's formation was influenced by α-enriched gas. However, the results from Lucchesi et al. (2020) suggest that this phenomenon is not consistent across all dwarf galaxies. Their study revealed that the metal-poor population in the Sextans dwarf spheroidal galaxy follows a Milky Way halo-like plateau at approximately [α/Fe] = 0.4 with a typical level of dispersion, indicating homogeneity in the early stages of the dwarf galaxy's chemical evolution.

Another way through which the chemical compositions of dwarf galaxies contribute significantly to our understanding of galaxy formation processes is by studying the ratio of alpha elements to iron, commonly denoted as [α/Fe]. In particular, a "knee" in the plot of [α/Fe] vs [Fe/H] indicates the onset of SNIa contributions to the chemical evolution of a galaxy, occurring around 100 Myr to 1 Gyr after the first star formation episode (Kobayashi et al. 2020a; Kobayashi et al. 2020b). For example, the knee position in the Sculptor dwarf spheroidal galaxy is well defined at [Fe/H] $\sim$ -1.8, indicating the time SNIa enrichment started, which was shorter than 1 Gyr (Boer et al. 2012). Other dwarf galaxies like the Sagittarius dwarf galaxy and Carina dwarf galaxy show different knee positions due to their distinct star-formation histories (de Boer et al. 2014a; de Boer et al. 2014b; Norris et al. 2017). Studies have also shown that the position of the knee appears to correlate with the galaxy's luminosity and mean metallicity, suggesting that more luminous galaxies formed stars earlier and retained metals more efficiently (e.g., Nidever et al. 2020)

Finally, ultra-faint dwarf galaxies (UFDs), with luminosities below 10^5 times that of the Sun, offer a unique perspective for investigating environments that differ from those observed in classical dwarf galaxies. As they are "the oldest, most dark matter-dominated, most metal-poor, and least chemically evolved stellar systems known" (Chiti et al. 2018), these objects help us understand the processes that govern the emergence of early galaxies and the characteristics of dark matter at smaller scales (Simon 2019). For elements up to the iron-peak, stellar abundances in UFDs closely align with the trends observed in the Milky Way's halo, implying that nucleosynthesis and chemical evolution during early stages are relatively uniform across different galactic environments. However, the most significant differences between UFDs and MW halo stars are found in the heaviest elements, particularly barium and strontium abundances, where UFDs typically exhibit notably lower ratios than halo stars (Ji et al. 2019).

Figure 1.2: Optical image of the Large and Small Magellanic Clouds.
Image Credit: ESO/S. Brunier

1.2 The Magellanic Clouds

Within the Milky Way's sphere of influence, we have 2 prominent dwarf galaxies, known as the Large and Small Magellanic Clouds (LMC and SMC). They are the largest satellites of the Milky Way (Besla et al. 2012). Located at about 50 and 60 kpc away from the centre of the Milky Way, the LMC and SMC are situated deep inside our galaxy's gravitational well (De Grijs & Bono 2015). This proximity makes them ideal locations to study various near-field astrophysical processes, including general problems regarding stellar evolution, the formation of stars, interstellar medium dynamics, and galaxy evolution. (Nidever et al. 2017).

For the past few decades, astronomers have attempted to understand the interaction histories between the LMC, SMC and the Milky Way. Although the Magellanic Clouds are two of the nearest dwarf galaxies to the Milky Way, it was only recently that we have started to piece together a detailed picture of the entire system. In the past, it was theorised that the Magellanic Clouds had orbited around the Milky Way several times and the tidal forces of the Milky Way had been the primary cause of the Magellanic Stream (Gardiner & Noguchi 1996), which comprises long streams of stripped HI gas connecting the LMC and SMC to each other, via the "Magellanic Bridge", and to the Milky Way (Nidever et al. 2010).

However, in the last two decades, proper motion measurements have uncovered that the Magellanic Clouds only entered the Milky Way potential recently ($\sim$4 Gyr ago),

also known as the first in-fall (Besla et al. 2007; Kallivayalil et al. 2006; Kallivayalil et al. 2013). There is also a possibility that a single earlier encounter (up to 10 Gyr ago) occurred at large distances (>100 kpc) (Vasiliev 2023). However, the LMC-SMC pair has "likely been gravitationally bound to each other for more than several Gyr and possibly for a Hubble time" (Besla et al. 2007). Models also show that the Clouds most likely experienced at least one close encounter or direct collision with each other $\sim$ 150 Myr ago (Zivick et al. 2018), giving rise to enhanced star formation due to "the tidal compression of gas clouds and their efficient conversion into stars" (Bekki et al. 2004; Belokurov & Koposov 2016). Furthermore, the study by Cullinane et al. (2022) showed that several parts in the southern region of the LMC, including two claw-like shapes and a long arm-like structure in the southeast, are mainly made up of LMC material, not debris from the SMC. Additionally, these areas exhibit noticeable disturbances in their motion. By comparing these observations with computer models, it suggests that the western part of the LMC's disk was significantly influenced by an event where the SMC crossed through the plane of the LMC's disk approximately 400 Myr ago. Thus, the primary features of the Clouds likely exist predominantly due to interactions between the LMC-SMC pair rather than either of them with the Milky Way. Since the Magellanic Clouds have spent almost all their lifetimes away from a large galaxy like the Milky Way, their star formation histories consequently probe a much different environment than our own Galaxy.

The Magellanic Clouds are also gas rich systems, unlike every other Milky Way satellite (McConnachie 2012). Thus, their star forming histories are essentially continuous over a Hubble time, which means that their stellar populations can act as continuous probes of evolution, including current star formation at slightly lower metallicities than the Milky Way ($[\mathrm{Fe/H}]_{\mathrm{LMC}} \sim -0.4, [\mathrm{Fe/H}]_{\mathrm{SMC}} \sim -0.7$) (Cioni 2018). As a result, the Magellanic Clouds possess a variety of objects, such as gravitationally bound massive star clusters of young to intermediate age, that are essentially absent from the Milky Way, where massive star clusters (which I refer to as globular clusters) are all generally older than 11.5 Gyr (Forbes et al. 2018), with only lower-mass open clusters formed more recently. These Magellanic clusters constitute the closest laboratories for directly testing the evolutionary processes shaping massive star clusters at different ages.

Past studies on the chemical composition of the LMC have significantly contributed to our understanding of its evolutionary history. Van der Swaelmen et al. (2013) conducted an extensive comparative analysis of the LMC and the Milky Way, focusing on the relationship between the LMC's bar and inner disc and their implications

for bar formation. They found that the LMC compared to the Milky Way exhibited lower abundance ratios for the light α-elements O and Mg, while heavier α-elements (Si, Ca, Ti) were comparable, suggesting significant contribution from type Ia supernovae and a relatively smaller contribution from massive stars compared to the Milky Way. Moreover, disparities between the LMC's bar and inner disc were observed in terms of [α/Fe], [Na/Fe] and [V/Fe]. This supports the occurrence of enhanced star formation several Gyr ago in the central regions of the LMC, culminating in the formation of the bar, which aligns with recent estimates of the LMC's star formation history.

Van der Swaelmen et al. (2013) also found other interesting chemical abundance results, specifically in terms of the heavy elements. In particular, the s-process elements, which can be further classified into light-s (e.g. Y, Zr) and heavy-s (e.g Ba, La) elements, are predominantly synthesised through the slow neutron capture process within stars. Based on their results, heavy element ratios such as [Ba/Eu] and [La/Eu] displayed significant increase with rising metallicity from approximately [Fe/H] ~ -0.8 dex, and the LMC demonstrated lower [Y + Zr/Ba + La] ratios relative to the Milky Way. These results indicate that the LMC's chemical history was significantly influenced by strong s-process enrichments from metal-poor AGB winds.

More recently, using abundance results from APOGEE, a spectroscopic survey, Nidever et al. (2020) discovered a slight elevation in the [α/Fe] ratio around $-1.0 <$ [Fe/H] < -0.5, indicating a recent surge in star-formation activity within the Magellanic Clouds. This trend was effectively reproduced via a comprehensive chemical evolution model incorporating a recent "starburst" event. Moreover, the study determined the "α-knee" position to be at [Fe/H] < -2.2 in both Magellanic Clouds, pointing to a relatively low star-formation efficiency of approximately $0.01\,\mathrm{Gyr}^{-1}$. Significantly, the observed position of the α-knees in the Magellanic Clouds appears more metal poor compared to those of smaller Milky Way dwarf galaxies, implying a potentially lower-density environment for the formation of the Magellanic Clouds. Therefore, their results align with the proposition that the Magellanic Clouds were more recently integrated into the gravitational influence of the Milky Way.

This PhD project focused on exploiting the diverse properties of the LMC to explore new angles on several contemporary problems in stellar and galactic astrophysics, as well as understanding in more detail the evolution of the LMC itself. I have chosen to direct my research focus towards the LMC instead of the SMC due to its proximity, facilitating the acquisition of detailed chemical abundance information.

By concentrating on the LMC, I intend to enhance the precision of my comparative analysis with data from the Milky Way, enabling a more insightful and meaningful comparison.

The thesis outline is as follows. Chapter 2 introduces massive star clusters and delves into the intriguing phenomenon of multiple populations within these clusters, with a focus on how understanding massive intermediate-age LMC clusters can help explain the existence of multiple populations. Chapter 3 introduces extremely metal-poor (EMP) stars and discusses their importance in helping us understand the star formation history and galactic evolution, especially in dwarf galaxies. This chapter also explores the existence of EMP stars within the LMC and the various methodologies used for their search. Chapter 4 presents a high-resolution spectroscopic search for multiple populations in an intermediate-age massive star cluster (NGC 1846) to confirm if the 2 Gyr minimum age for the existence of multiple populations exists. Chapter 5 shifts the focus to the search for EMP stars in the LMC using SkyMapper photometry and low-resolution spectroscopy. Chapter 6 presents the results of a high-resolution spectroscopic follow-up of EMP stars in the LMC, including key chemical abundance findings and comparisons with the Milky Way halo. Finally, a summary of results, their implications in the context of understanding the chemistry of stars in the LMC, and directions for future work, are given in Chapter 7.

Chapter 2

Massive Star Clusters

2.1 Introduction to Massive Star Clusters and their importance in astronomy

Massive star clusters ($> 10^{4.5}$ solar masses), including globular clusters found in the Milky Way, are notable for their dense and tightly bound configurations. They consist of thousands to millions of stars densely packed within a relatively small region of space, and the stellar density in these clusters can be several orders of magnitude higher than in the surrounding galactic field (Gratton et al. 2019). Due to their tightly knit structure, massive star clusters are able to withstand disruptive forces from external gravitational sources, such as passing giant molecular clouds or tidal forces from their host galaxies. As a result, these star clusters are among the oldest surviving objects in the universe, surpassing 10 billion years in age (Gratton et al. 2019). This allows us to test different astrophysical processes as outlined below.

The long history of such star clusters makes them useful probes into the conditions of the early universe, as they offer a unique glimpse into star formation processes at high redshift. Through comprehensive analyses of their colour-magnitude diagrams (CMDs) and spectroscopic observations, the ages, metallicities, and distribution of stars in massive star clusters can be obtained, allowing astronomers to reconstruct the star formation histories of different galaxies, including our own (e.g. Peng et al. 2008; Chilingarian & Asa'd 2018; Sakari 2019).

Beyond their utility in studying individual galaxies, massive star clusters also act as probes for tracing the signatures of dwarf galaxy accretion events. Studies of the Andromeda Galaxy (M31) exemplify this role, where the analysis of star clusters and associated substructures in the halo revealed perturbed disk features and accreted dwarf galaxies (McConnachie et al. 2018). This integrated approach has crucially revealed a direct connection between the star clusters and the now disrupted dwarf galaxies, highlighting how these clusters were part of the accreted material, thereby

Figure 2.1: Optical image of a Globular Cluster M2.
Image Credit: NASA, ESA, STScI, and A. Sarajedini (University of Florida)

contributing to our understanding of the hierarchical growth of galaxies and the significant role of mergers and interactions in shaping their structures.

2.2 Multiple Populations in Massive Star Clusters

On the surface, massive star clusters appear to be straightforward chemical specimens of the Universe to study since they have been theorised to form from a chemically homogeneous gas cloud contracting and fragmenting into stars. This implies that stars within these clusters were previously believed to belong to single stellar populations, sharing identical ages and chemical compositions. However, high-resolution and high signal-to-noise spectroscopic studies first revealed more than 50 years ago that massive star clusters such as M4, 47 Tucanae and NGC 6752 exhibit anomalous chemical abundance patterns. In particular, the abundances of light elements generated by proton capture processes (e.g. C, N, O, Na, Mg, Al) were found to vary significantly in these clusters (Osborn 1971; Kraft 1979; Cottrell & Da Costa 1981; Norris 1981; Carretta et al. 2009), suggesting chemically distinct stellar populations within a cluster.

In recent decades, these patterns were also seen indirectly via UV/blue-photometry. As part of the Hubble Space Telescope UV Legacy Survey of Galactic Globular Clusters, a trio of photometric filters (F275W, F336W, and F438W) found in the WFC3/UVIS instrument were used to observe ~ 60 globular clusters in the Milky Way. These filters are useful for identifying different groups of stars within globular clusters because they capture specific molecular features. For example, the F275W and F336W filters show molecular bands related to OH and NH, while the F438W filter highlights CN and CH bands (Milone et al. 2012). This method proved to be exceptionally effective in discerning and characterising unusual CMD patterns, such as multiple red-giant branches (RGBs), sub-giant branches (SGBs), horizontal brances (HBs) and even split main sequences (e.g. Milone et al. 2012; Piotto et al. 2015). This gave further evidence that many massive clusters in our Milky Way could not be represented by a single stellar population model.

More recently, a new method to study the various groups of stars in massive star clusters has emerged, known as the chromosome map (ChM). The ChM is a special two-colour diagram that uses photometric data from the previously mentioned trio of filters along with the F814W filter. What sets the ChM apart from a simple two-colour diagram is that it arranges the sequence of main sequence (MS), red giant branch (RGB), or asymptotic giant branch (AGB) stars vertically in both

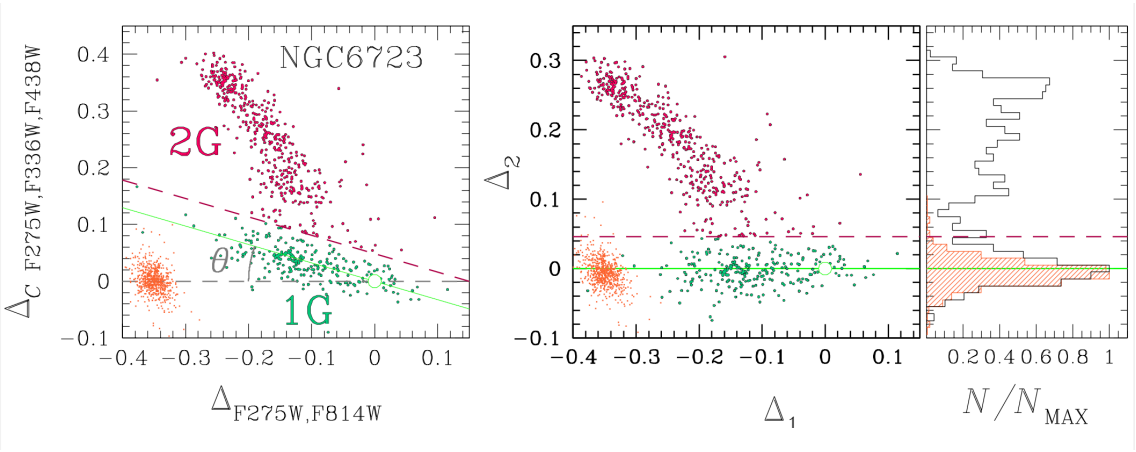

Figure 2.2: The diagram from Milone et al. (2017) illustrates the technique employed for identifying first generation (1G) and second generation (2G) red giant branch stellar members within NGC 6723. In the left panel, the $\Delta_{F275W,F336W,F438W}$ vs $\Delta_{F275W,F814W}$ diagram is reproduced, with a green line indicating the fitted sequence of candidate 1G stars at an angle of $\theta = 18°$ relative to the horizontal line. The middle panel displays the $\Delta 2$ vs $\Delta 1$ plot, generated by rotating counterclockwise by an angle θ with respect to the left panel. The right panel depicts the distributions of the $\Delta 2$ values. The distribution of observational errors in the left and middle panels are represented by the orange points, while the $\Delta 2$ distribution is indicated via the shaded orange histogram in the right panel. In the left and middle panels, the aqua and magenta colour-coding represent the selected 1G and 2G stars respectively, separated by dashed magenta lines.

dimensions (Milone et al. 2017). To illustrate, the ChM depicted in Fig. 2.2 for RGB and MS stars of the NGC 6723 cluster are formed by plotting a pseudo-colour $C_{F275W,F336N,F438W}$, which is mainly sensitive to the nitrogen abundance of multiple populations, against $m_{F275W} - m_{F814W}$, which reflects differences in helium content and possibly metallicity variations among the stellar populations (e.g., Legnardi et al. 2022).

It is now known that nearly every massive cluster within the Milky Way contains multiple stellar populations. (Gratton et al. 2012). Specifically, they exhibit two main stellar populations, comprising a first generation[1] (1G) composed of stars exhibiting chemical characteristics akin to those observed in halo stars, and a second generation (2G), encompassing stars marked by elevated He, N, Na and Al abundances, while displaying relative deficiencies in C, O and Mg compared with their 1G counterparts (Gratton et al. 2012; Piotto et al. 2015). Fig. 2.3 shows the common anti-correlations between the abundances of light-element pairs, such as Na/O and Mg/Al. Correlations for Na/N and Al/N light-element pairs are shown as well. While most of these clusters exhibit minimal variations in iron abundance, as in-

[1]The use of the word 'generation' does not imply a temporal sequence.

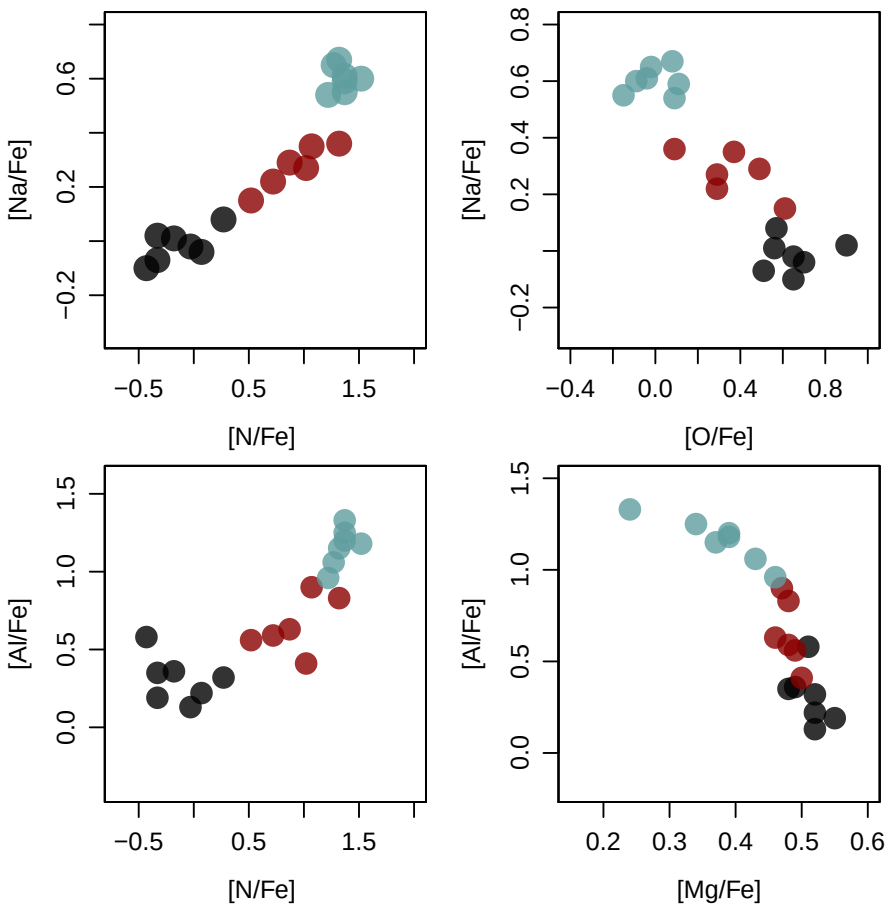

Figure 2.3: The diagram from Bastian & Lardo (2018) illustrates the typical light-element correlations and anti-correlations associated with multiple populations found in a cluster. The cluster that was studied in this case was NGC 6752.

ferred from their narrow RGB sequences, there are some exceptions, as seen for example in M22 and Omega Centauri, among others, that exhibit significant metallicity dispersions (e.g., Freeman & Rodgers 1975; Norris & Freeman 1983; Norris & Da Costa 1995; Da Costa et al. 2009; Marino et al. 2012). Based on HST photometric data, the most extreme example, Omega Centauri, was found to display "at least four different populations covering a wide range of chemical abundances and age across the subgiant branch in the CMD" (Fig. 2.4), as well as a main-sequence bifurcation (Villanova et al. 2007), implying the presence of a strongly helium-enriched population (Norris 2004; Piotto et al. 2005). One potential theory for such characteristics is that these clusters are the residual nuclei of former dwarf galaxies which were disintegrated by the Milky Way (e.g., Majewski et al. 2000; Pfeffer et al. 2020).

However, the source and underlying mechanisms governing these varying chemical abundances remain poorly understood, as they diverge from the fundamental prin-

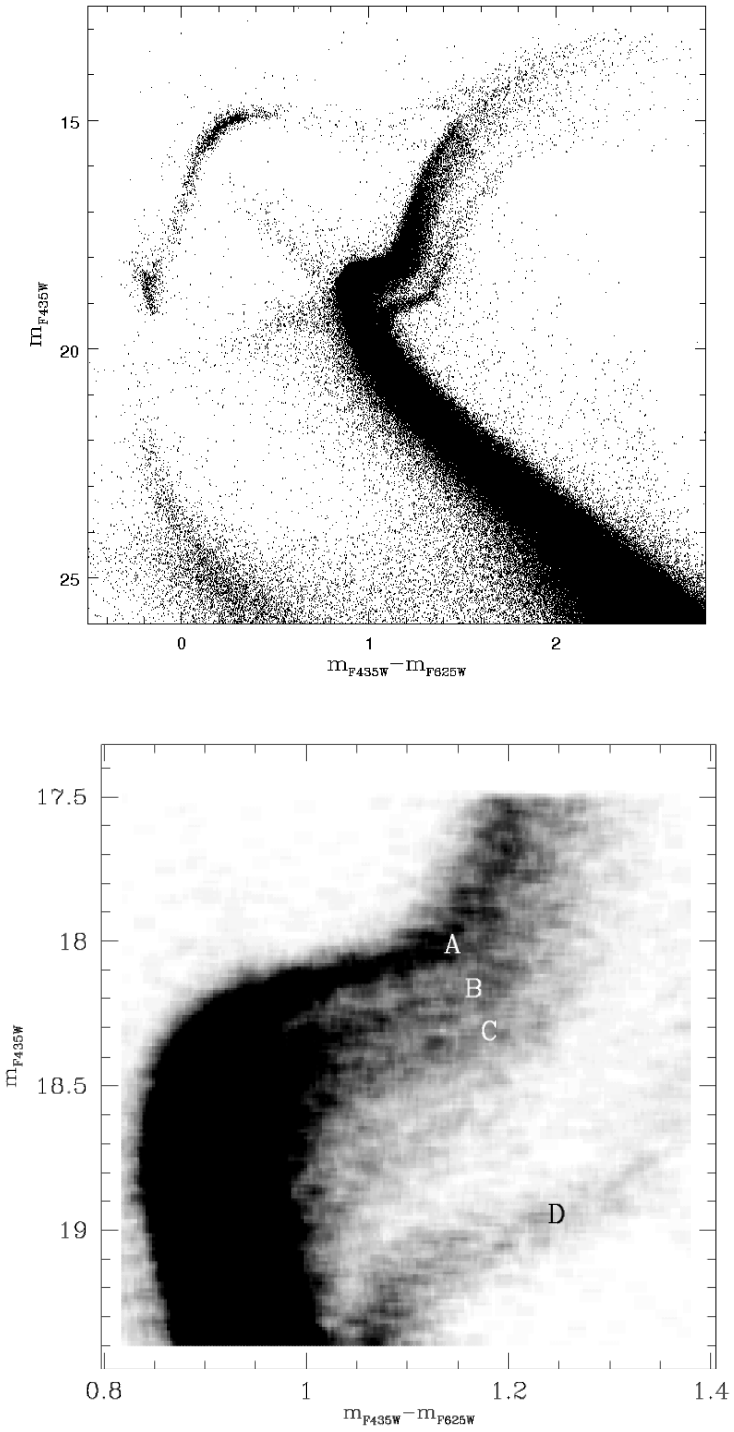

Figure 2.4: Top: Overall CMD of Omega Centauri, from the photometry of more than a million stars in the central $3' \times 3'$ HST ACS fields. Bottom: Hess Diagram of the subgiant branch region of Omega Centauri. At least 4 different populations of stars can be observed here. Both figures were taken from Villanova et al. (2007).

ciples of star cluster formation. Much effort has been undertaken to determine the cause of these distinct light-element abundance patterns, and a detailed review of this topic can be found in the work by Bastian & Lardo (2018). One hypothesis involves the transformation of material from first-generation stars at high temperatures (e.g. in intermediate-mass AGB stars), which is then combined with a certain amount of unprocessed material with pristine composition via a suitable gas reservoir, forming the second generation of stars (e.g. D'Ercole et al. 2008; Conroy & Spergel 2011).

An alternative theory involves massive rotating stars. Since massive stars also experience intense H-burning within their cores during the main sequence phase, they are able to generate enriched material required for the formation of multiple populations. Through rotation-induced mixing, enriched material found deep within the massive rotating star is able to be transported to the stellar surface, where it can gradually be released into the intracluster environment via outflows. This topic is discussed in depth by Bastian & Lardo (2018), and the interested reader is referred to that work and the references therein. Thus, this process can provide the necessary gas reservoir to create a subsequent generation of stars characterised by distinct light-element abundance patterns.

However, the existing theories put forward so far exhibit fundamental shortcomings. For instance, the two principal models, namely the AGB and massive rotating star enrichment, both imply the formation of multiple populations of stars, indicating a prolonged duration of star formation. Unfortunately, this is in conflict with the observed maximum internal age dispersion within young massive star clusters ($\leq$ 30 Myr; De Marchi et al. 2011) that is significantly lower than the time required for intermediate-mass stars to progress to the AGB phase and initiate the pollution for the formation of the second generation of stars, typically taking about 40–160 Myr. In contrast, this age spread greatly exceeds the relatively brief time interval ($\sim$ 6 Myr) needed between the pollution of massive rotating stars and their eventual supernova explosions (Gratton et al. 2012). A further issue, called the mass budget problem, is discussed in depth by the discussion by Renzini et al. (2015) regarding the mass budget problem.

As none of these explanations have succeeded in replicating the primary observed characteristics of multiple stellar populations without resorting to improvised assumptions, a comprehensive and internally consistent explanation for the physical mechanisms underpinning the phenomenon of multiple populations remains elusive. Additionally, we still lack a proper grasp of which properties of massive star clusters dictate whether they will exhibit chemical abundance patterns or not (Martocchia

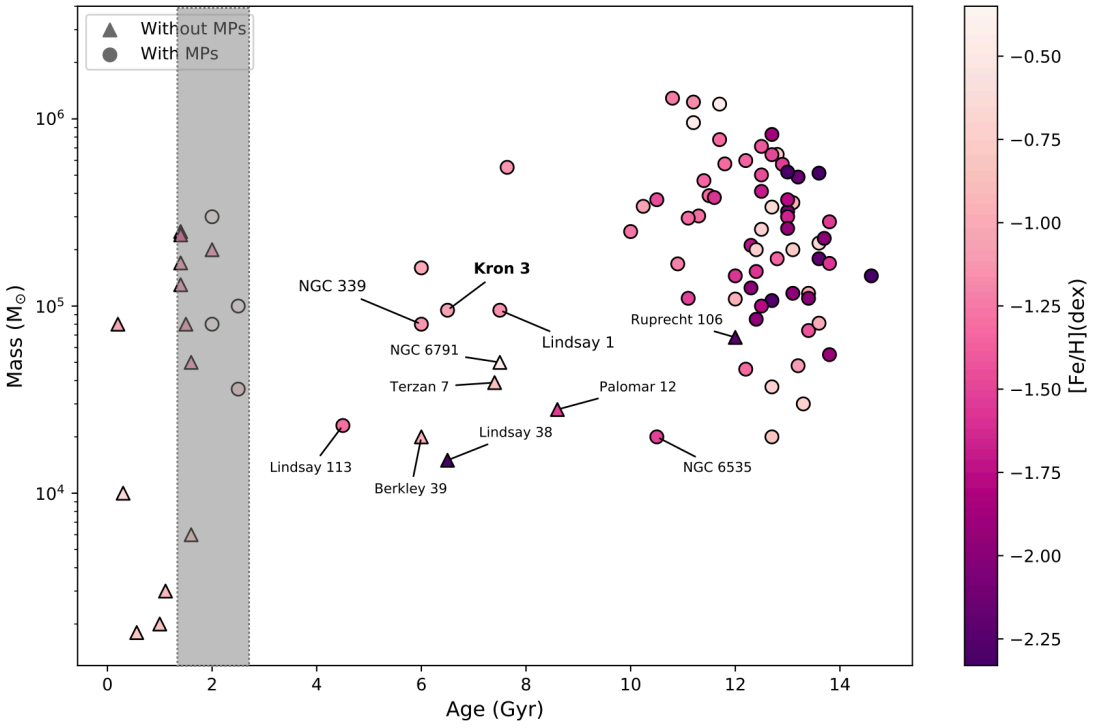

Figure 2.5: This illustrates the relationship between cluster mass, cluster age and the presence of multiple populations. The circles indicate clusters that contain multiple populations, while triangles symbolise clusters where multiple populations have not been found. The grey region shows the supposed 2 Gyr minimum age limit for the presence of multiple populations. Do note that this limit is shown as a grey region rather than just a line due to the age uncertainties of the clusters. Kron 3 is highlighted in bold and is positioned at the mass reported by Hollyhead et al. (2018). The data points are sourced from various studies, including those by Hollyhead et al. (2017, 2018, 2019); Krause et al. (2016); Martocchia et al. (2017, 2018, 2019); Niederhofer et al. (2017). This diagram was adapted from Salgado et al. (2022).

et al. 2018).

2.3 Massive Intermediate-Age Magellanic Cloud Clusters

For several decades, astronomers held the belief that multiple populations were exclusively present in ancient globular clusters. This perception primarily stemmed from the lack of readily accessible intermediate-age massive star clusters within our Milky Way, specifically those aged between 1 to 10 Gyr and with masses exceeding $10^{4.5}$ solar masses (Portegies Zwart et al. 2010). Furthermore, multiple populations

are notably absent in the Milky Way open clusters, which are considerably less massive than their globular counterparts.

To gain deeper insights into the primary factors influencing the occurrence of multiple populations in star clusters, a key method involves exploring younger massive star clusters in nearby galaxies, as summarised by Gratton et al. (2019). One example of such star clusters are the massive intermediate-age clusters in the Magellanic Clouds. These clusters serve as the nearest available analogs to systems with globular cluster-like masses while being significantly younger, thereby offering a crucial glimpse into the formation and evolution of star clusters across different epochs.

Previous research has delved into the possible correlation between chemical anomalies and the presence of an extended main-sequence turn-off (eMSTO) in CMDs of these young and massive intermediate-age massive clusters. This eMSTO phenomenon was initially associated with internal age spreads (Mackey et al. 2008; Bastian & Lardo 2018; Milone et al. 2018), and was theorised by some models to explain variations in light element abundances observed in globular clusters. However, recent findings propose that stellar rotation could significantly contribute to the emergence of the eMSTO. Research by Kamann et al. (2020) for example, have highlighted how stellar rotation influences internal stellar structure, altering evolutionary paths in the CMD by affecting temperature and colour relative to non-rotating stars of the same mass and composition.

Recently, splitting or dispersion in the subgiant and red giant branches have been observed in various LMC clusters using photometry (Martocchia et al. 2018). It is essential to note that the observed effects are distinct from those attributed to variations in metallicity, as commonly observed in clusters such as Omega Centauri. The LMC clusters exhibit uniform metallicity, and the variations are instead presumed to stem from fluctuations in nitrogen abundance within the individual stars. NGC 2173, a cluster with an age of 1.7 Gyr, represents the youngest known cluster displaying a split RGB (Kapse et al. 2022). Cadelano et al. (2022) also showed significant broadening (exceeding photometric errors by 50%) among main sequence stars within NGC1783, a cluster aged at 1.5 Gyr. As shown in Fig. 2.5, these examples are part of a broader collection of studies highlighting that multiple populations are not exclusive to ancient globular clusters (Salgado et al. 2022). In fact, past results also seem to suggest a 2 Gyr minimum threshold for the emergence of multiple populations within massive star clusters (Martocchia et al. 2018). However, the absence of high-resolution spectroscopic evidence for chemical abundance dispersions in LMC clusters younger than 2 Gyr remains an issue (Mucciarelli et al. 2008), leaving the

age dependence of multiple populations in massive clusters uncertain.

Chapter 4 will present a detailed analysis of chemical abundances including O, Na, and Mg in NGC 1846, an intermediate-age massive LMC cluster with a mass of approximately 6×10^4 solar masses (Song et al. 2019) and an age of 1.95 billion years (Goudfrooij et al. 2009). This research aims to directly assess the 2 Gyr threshold regarding the presence of chemical abundance dispersions in massive star clusters. Contrary to UV photometry, this method enables the direct determination of chemical abundance variations. Notably, the investigation of Na, which remains unaffected by evolutionary mixing in contrast to C and N, serves as a distinct indicator of the presence of multiple populations in RGB stars (e.g., Salgado et al. 2022).

Chapter 3

Earliest stellar generations

3.1 Introduction to Extremely Metal-Poor stars and their importance in astronomy

The properties of the oldest stars in the universe can potentially shed light on the history of the Galaxy, including its formation. One of the ways of studying these very old stars is by looking for extremely metal poor (EMP) stars in the galaxy field. Characterised by a low iron abundance ($[Fe/H] \leq -3.0$), EMP stars represent some of the most ancient observable stars in the universe. Although they do not constitute the initial generation of stars originating directly from the primordial gas of the Big Bang, EMP stars remain crucial in uncovering the characteristics of the universe's earliest stars. They also provide valuable insights into the processes governing the formation and development of galaxies during the early stages of stellar formation, since they are second generation stars that formed from gas enriched by the supernovae of their metal free predecessors. Their study offers a glimpse into the properties of the first stars and the initial conditions of star formation within early galaxies (e.g., Frebel & Norris 2015).

In recent decades, several spectroscopic and photometric surveys have been conducted to study metal-poor stars, including the Hamburg/ESO survey (Frebel et al. 2006; Christlieb et al. 2008). This survey, which targeted the CH G-band strengths, has been moderately successful in finding EMP stars. However, one of the most effective methods so far is currently through the analysis of photometric data from Pristine and SkyMapper. The latter is a wide-field survey telescope that conducts imaging programs covering a large proportion of the sky across multiple distinct filters (Starkenburg et al. 2017; Onken et al. 2019). As discussed in Keller et al. (2007) and Da Costa et al. (2019)), and as illustrated in Fig. 3.1, the distinctive v filter of Skymapper enables the identification of stars with [Fe/H] ≤ -2.5 through a metallicity sensitive colour-colour diagram (Fig. 3.1). This approach has proven highly efficient in the discovery of EMP stars within the Milky Way (e.g., Da Costa et al.

2019; Chiti et al. 2020; Yong et al. 2021a), with over 40% of photometrically-selected candidates exhibiting [Fe/H] ≤ -2.75. The utilisation of this method has led to the discovery of a couple of ultra-metal-poor stars, including the identification of the star with the lowest recorded iron abundance to date (SMSS J160540.18–144323.1; [Fe/H] $= -6.2$; Nordlander et al. 2019) and the most iron-deficient star known (SMSS J031300.36–670839.3; [Fe/H] ≤ -6.5; Keller et al. 2014). For these particular stars, the studies specifically saw a mapping between their (unusual) abundances and properties of progenitor Pop III stars + supernovae. For example, the star discovered by Nordlander et al. (2019) shows an absence of notable s- or r-process enrichment. This pattern is potentially explained by the explosion of Population III stars as fallback supernovae, with the model matches suggesting a progenitor star mass of about 10 $M_{\odot}$, indicating low kinetic energy in the supernova ejecta.

Regarding the rarity of the EMP population, it is noteworthy to consider the metallicity distribution function (MDF) presented in Da Costa et al. (2019) and Yong et al. (2021a). These studies revealed an abrupt decline in the number of stars below [Fe/H] $= -4.0$ dex, suggesting a scarcity of stars in this metallicity range. Above this metallicity, the MDF follows a power-law distribution, with a slope of approximately 1.5 ± 0.1 dex per dex for [Fe/H] $= -3$. Additionally, stars with notably low metallicities exhibit a range of distinct properties, and the detailed chemical compositions of EMP stars and their variety are discussed in, for example, Yong et al. (2021a), which demonstrates the importance of large sample of such stars.

3.2 EMP stars in Dwarf galaxies

Initially, efforts to search for EMP stars outside our Milky Way were focused on the classical dwarf galaxies, but no stars with [Fe/H] < -3.0 were found (Helmi et al. 2006). Following the development of a technique for fitting medium-resolution spectra with model atmosphere synthetic spectra to directly measure [Fe/H] abundances, 15 EMP stars with [Fe/H] < -3.0 were found in eight ultra-faint systems (Kirby et al. 2008). At that point, there were still very few EMP examples known in the classical dwarf satellites of the Milky Way (e.g., Draco, Fornax), and such stars seem relatively more common in the ultra-faint dwarf satellites of the Milky Way, which (by nature) are more metal-poor objects. More importantly, another reason for the lack of EMP discoveries was due to a shortcoming in previous calibrations of the Ca II Infrared Triplet metallicity index. Subsequently, there was a revision to those calibrations (Starkenburg et al. 2010), and soon a handful of stellar members with ultra-low metallicities ([Fe/H] $= -4.0$) were found in both the Sculptor and

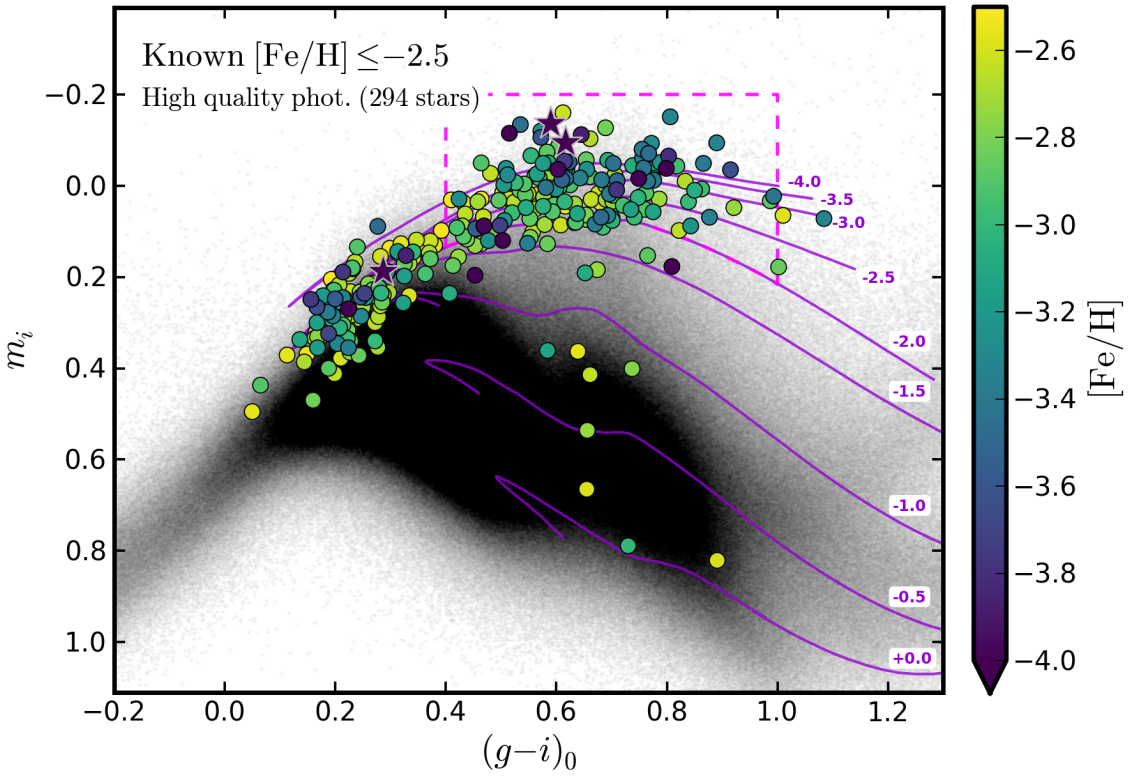

Figure 3.1: The colour-colour metallicity-sensitive diagram from Da Costa et al. (2019) illustrates the method used to identify EMP candidates using photometry from SkyMapper data release DR1.1. The formula to calculate the metallicity index m_i is given by: $(v - g)_0 - 1.5(g - i)_0$. The coloured circles represent known EMP stars with [Fe/H] ≤ -2.5, calibrated using high-dispersion spectroscopic studies. Most of the plotted stars (in circles) are located around the low metallicity isochrones from the Dartmouth Stellar Evolution Database. The right side of the figure shows a colour bar indicating the corresponding metallicities derived from high-dispersion spectroscopy. The final adopted selection window is depicted by the magenta dashed lines.

Fornax dwarf galaxies (Frebel et al. 2010; Tafelmeyer et al. 2010; Starkenburg et al. 2013; Jablonka et al. 2015; Skúladóttir et al. 2023).

The chemical signatures of EMP stars within dwarf galaxies offer valuable insights into the underlying mechanisms driving the evolution of these galaxies. Venn et al. (2012) showed that very metal-poor stars in the Carina dwarf galaxy did not exhibit enhancements in AGB or SN Ia products. As a result, their very low [Sr/Ba] ratios suggested a lack of chemical enrichment from early Type II supernovae. Low ratios of Na, Mn and Cr in two of these stars also supported this scenario. Intriguingly, the chemical composition of the metal-poor stars in Carina differed from that of the Galaxy, most other dwarf spheroidal galaxies, or ultra-faint dwarfs. This finding suggested that the Carina dwarf galaxy may be at a critical mass where certain chemical enrichments are lost due to supernova-driven winds (Venn et al. 2012).

Similarly, the chemical characteristics of EMP stars found in ultra-faint dwarf galaxies provide valuable insights into the fundamental processes steering the evolution of these galaxies. One example is shown in Reticulum II (Ret II), an ultra-faint dwarf galaxy. Due to its faint nature, only two dozen red giant stars have been documented for this object. Ji et al. (2016) studied the brightest nine, and found extremely low metallicities in them ($-3.5 <$ [Fe/H] < -2). Furthermore, they discovered that seven out of the nine stars studied exhibit notably elevated levels of r-process abundances ([Eu/Fe] ~ 1.7). This sets Ret II apart from all other ultra-faint dwarf galaxies studied thus far, which do not show significant r-process enrichment. This discovery supports the hypothesis that neutron star mergers represent the primary source of r-process elements during the early stages of the galaxy's evolution in not only Ret II but also in other r-process enhanced dwarf galaxies. Notably, the absence of r-process enhancement in the two most metal-poor stars in Ret II ([Fe/H] < -3), suggests the possibility that these stars were formed prior to substantial r-process enrichment events. Although the possibility of inhomogeneous metal mixing in these environments cannot be completely excluded, their results imply that significant r-process enrichment likely occured after the initial enrichment in the α and iron-peak elements.

More recently, Skúladóttir et al. (2021) identified an ultra-metal-poor star in the Sculptor dwarf spheroidal galaxy exhibiting $[\mathrm{Fe/H}]_{\mathrm{LTE}} = -4.11$, making it the most metal-poor star found in any external galaxy thus far. Unlike general Milky Way stars at similar metallicities, this star exhibited an unusual absence of carbon enhancement, having $[\mathrm{C/Fe}]_{\mathrm{LTE}} = -0.75$ and $\mathrm{A(C)} = +3.60$, which represents the lowest carbon abundance observed in any known star. Additionally,

the star's non-uniform α-element ratios, particularly $[\mathrm{Mg/Ca}]_{\mathrm{NLTE}} = -0.60$ and $[\mathrm{Mg/Ti}]_{\mathrm{NLTE}} = -0.86$, deviated significantly from the solar-like ratios found in stars with normal carbon abundances within the Milky Way halo. This distinctive abundance pattern suggests that the star's formation was influenced by material enriched by a $\sim 20 M_{\odot}$ progenitor star with an exceptionally high explosion energy of E = 10×10^{51} erg. Thus, the unique characteristics of this star provide valuable insights into the phenomenon of zero-metallicity hypernovae and offer a rare opportunity to explore the varied characteristics of Population III stars.

3.3 Investigation into the existence of EMP stars in the Magellanic Clouds

Despite being the largest satellites of the Milky Way, the Magellanic Clouds remain largely unexplored in terms of their EMP stellar populations. The documented metallicities of the Magellanic samples, although low, do not match the exceptionally low values observed in the Milky Way halo or smaller dwarf satellites. While results from low-resolution spectroscopy have found some very metal-poor stars in the LMC (Cullinane et al. 2022; Emptage 2023), the most metal-poor LMC star discovered so far using high-resolution spectroscopy only has a metallicity of [Fe/H] = −2.4 (Reggiani et al. 2021). More information on their star selection and analysis method can be found in that paper. Notably, all the metal-poor Magellanic stars within their sample, ranging from −2.4 to −1.5 in [Fe/H], exhibited r-process enhancements. This was highlighted by significantly higher europium abundances ([Eu/Fe] $\sim$ 0.9) relative to the Milky Way ([Eu/Fe] $\sim$ 0.3) at corresponding [Fe/H] levels, indicating prolonged r-process enrichment events in the Magellanic clouds. These findings may be indicative of the unique evolution and extended accretion history from the cosmic web of the Magellanic Clouds. This evolving field of chemical abundance analysis has prompted an extensive and meticulous exploration for EMP stars within the Magellanic Clouds, which will be covered in Chapter 5 and 6. The findings will provide significant knowledge regarding the initial phases of star formation in the LMC and offer the first comprehensive data on EMP stars and the lower end of the metallicity distribution function in galaxies of this mass.

Chapter 4

Paper I: A high-resolution spectroscopic search for multiple populations in the 2 Gyr old cluster NGC 1846

This chapter is published as W. S. Oh, T. Nordlander, G. S. Da Costa and A. D. Mackey, 2022. A high-resolution spectroscopic search for multiple populations in the 2 Gyr old cluster NGC 1846. MNRAS, 519, 831. The paper is reproduced here in full with minor formatting changes to make it consistent with the rest of the work in this thesis. The original data used in this study are available in the ESO archive (https://archive.eso.org/eso/eso_archive_main.html) under program ID 082.D-0387 (PI: Mackey). I have re-reduced the data, and the coadded spectra are available upon request. The ACS/WFC photometric data of NGC 1846 targets only were obtained from Mackey et al. (2013); they originate in HST program GO9891 (PI: Gilmore) and GO10595 (PI: Goudfrooij). The subsequent analysis and composition of the research paper were undertaken by myself, incorporating valuable insights and contributions from co-authors.

4.1 Abstract

We present detailed C, O, Na, Mg, Si, Ca, Ti, V, Fe, Zr, Ba, and Eu abundance measurements for 20 red giant branch (RGB) stars in the LMC star cluster NGC 1846 ([Fe/H] = -0.59). This cluster is 1.95 Gyr old and lies just below the supposed lower age limit (2 Gyr) for the presence of multiple populations in massive star clusters. Our measurements are based on high and low-resolution VLT/FLAMES spectra combined with photometric data from HST. Corrections for non-local thermodynamic equilibrium effects are also included for O, Na, Mg, Si, Ca, Fe and Ba.

Our results show that there is no evidence for multiple populations in this cluster based on the lack of any intrinsic star-to-star spread in the abundances of Na and O: we place 95 % confidence limits on the intrinsic dispersion for these elements of ≤ 0.07 and ≤ 0.09 dex, respectively. However, we do detect a significant spread in the carbon abundances, indicating varying evolutionary mixing occurring on the RGB that increases with luminosity. Overall, the general abundance patterns for NGC 1846 are similar to those seen in previous studies of intermediate-age LMC star clusters and field stars.

4.2 Introduction

It has been known for decades that almost every globular cluster (GC) in the Milky Way possesses multiple stellar populations. This refers to a cluster having two main stellar groups: a first generation (1G), consisting of stars that are chemically similar to halo stars, and a second generation (2G), consisting of stars rich in He, N, Na and Al, and poor in C, O and Mg with respect to 1G. (Gratton et al. 2012; Piotto et al. 2015). UV and optical photometric data allows these stellar groups to be differentiated using colour-magnitude diagrams (CMD). Indeed, past studies have shown distinct CMD features for a large number of clusters (~ 60) such as multiple red-giant branches (RGBs), sub-giant branches (SGBs) and even main sequences (MSs) (Milone et al. 2009; Milone et al. 2017), indicating He and N variations (Milone et al. 2018). These findings have been complemented by spectroscopic observations indicating star-to-star variations in light elements. In particular, they occur in the form of abundance anti-correlations between Na and O, Mg and Al, and C and N (Bastian & Lardo 2018).

However, the origin and mechanism behind these variations are not well understood, since they are not predicted by the basic theory of star cluster formation. Various attempts have been made to explain the production of such abundance patterns, and a popular theory involves the processing of first-generation stellar material at high temperatures, with the processed material then incorporated into a second generation of star formation via a suitable gas reservoir, mixed with some amount of unprocessed material with 1G composition (e.g. D'Ercole et al. 2008; Conroy & Spergel 2011). Examples of such processing can be found in intermediate-mass asymptotic giant branch (AGB) stars and massive rotating stars. In both cases, enriched material is brought up to the stellar surface where it can be released into the intracluster medium. The mass lost from these stars would form the gas reservoir that is needed to form a second generation of stars with the 2G light-element

abundance patterns.

Unfortunately, these and other proposed theories to date have been shown to have at least one fundamental flaw (Renzini et al. 2015; Bastian & Lardo 2018). For example, the two key models (AGB enrichment and fast rotating massive star enrichment) mentioned above both require the formation of multiple generations of stars and hence star formation spanning some extended interval. However, the maximum internal age dispersion observed in young massive star clusters of ∼30 Myr (De Marchi et al. 2011) is not sufficient for intermediate-mass stars to evolve to the AGB and start polluting the next generation, as this typically takes around 40-160 Myr. On the other hand, this age spread is too large for the small time interval (∼6 Myr) required between the pollution from massive rotating stars and their supernova explosions (Gratton et al. 2012). Since none of the proposed models have been able to reproduce the main observational properties of multiple stellar populations without making ad hoc assumptions, a self-consistent explanation of the physical processes responsible for the multiple populations phenomenon is lacking, as well as an understanding of which (if any) cluster properties control whether a GC will host chemical anomalies or not (Martocchia et al. 2018; Milone et al. 2019).

Past studies have shown that the role of the estimated initial cluster mass is an important factor in determining whether clusters display multiple populations (Milone et al. 2019). Abundance inhomogeneities are rarely seen in clusters with present-day masses less than $\sim 10^5$ solar masses (Gratton et al. 2012), which explains why most of the Milky Way clusters that display multiple populations are globular clusters.

Another theory that has been studied in the past is the connection between chemical anomalies and the presence of an extended main-sequence turn-off (eMSTO) in CMDs of star clusters. The eMSTO feature is observed in young and intermediate-age massive clusters (20 Myr - 2 Gyr) (Mackey et al. 2008; Bastian & Lardo 2018; Milone et al. 2018), and was initially hypothesised to be due to internal age spreads of up to a few hundred Myr, as predicted by some of the previously-discussed models for the formation of light element abundance variations in globular clusters. While multiple populations in GCs have sometimes been inferred purely from the presence of broadened or split main-sequences and turn-offs in the CMDs of young/intermediate-age clusters, these features are not necessarily associated with chemical abundance variations. Recent work by Kamann et al. (2020) (but also see the discussion in Bastian & Lardo 2018) has shown that stellar rotation might be a significant factor in causing features such as the eMSTO to form. Rotation alters the internal stellar structure, because the centrifugal support and extra mixing in the core changes its

hydrostatic equilibrium compared to that of a non-rotating star of the same mass and composition. These factors cause the evolutionary path of the rotating star in the CMD to vary in temperature and colour relative to the equivalent non-rotating star. Hence, the relationship with multiple populations in younger clusters (if any) remains unknown.

Therefore, to determine the leading factor for the presence of multiple populations in star clusters, and to better understand the timescale of the multiple population process, one key method is to look for multiple populations in younger populous clusters in nearby galaxies (Gratton et al. 2019), since there are no such clusters in the Milky Way (Portegies Zwart et al. 2010). An example of such objects are the massive intermediate-age (2-8 Gyr) Magellanic Cloud clusters. These are the closest examples of systems with globular cluster-like masses but much younger ages, providing direct snapshots of the cluster formation and evolution process at different times.

Past studies have shown that LMC clusters are also found with an observed splitting or spread in the subgiant and red giant branches when certain photometric filter combinations are used (Martocchia et al. 2018). NGC 2173, with an age of 1.7 Gyr, is the youngest cluster discovered so far that exhibits a split RGB, which is a photometric signature of chemical abundance variations (Kapse et al. 2022). This is one example of a number of works (see Salgado et al. 2022 for further examples) that show that the abundance patterns are not restricted to ancient globular clusters. However, since no spectroscopic analysis of clusters in the LMC younger than 2 Gyr have so far found evidence of chemical abundance spreads (Mucciarelli et al. 2008), we are still unsure of the age dependence for the occurrence of multiple populations in massive clusters.

In this work, we present a high-resolution study of elements including O, Na and Mg in NGC 1846, a LMC massive cluster with a mass of $\sim 6 \times 10^4 M_\odot$ (Song et al. 2019) and an age of 1.95 Gyr (Goudfrooij et al. 2009). This will allow a direct test of the 2 Gyr boundary for the age of massive star clusters exhibiting chemical abundance spreads. Compared to UV photometry, our approach allows the chemical abundance variations to be directly determined. In addition, since Na is unaffected by evolutionary mixing unlike in C and N, its abundance variation is a clear indicator of the presence of multiple populations in RGB stars (e.g., Salgado et al. 2022).

We present the observational material for the NGC 1846 RGB stars in Section 4.3, and our photometric and spectroscopic analysis methods in Section 4.4. In Section 4.5, we present results of the abundance measurements based on both low and high-resolution spectroscopy. We also analyse the lack of any clear anti-correlation

abundance signatures, and present statistical limits on the star-to-star abundance dispersion that may be present.

4.3 Observations and Data Reduction

4.3.1 NGC 1846 RGB stars

The candidate cluster members were selected by Mackey et al. (2013) on the basis of CMD location, distance from the cluster centre and radial velocity. As shown in their Figure 4, there is a well-defined group of candidate members centred on the known cluster velocity of $\sim$240 km s^{-1}(e.g., Grocholski et al. 2006) and lying within the 161 arcsec truncation radius (Goudfrooij et al. 2009) for the cluster. In contrast, non-members in the same field have radial velocities in the wide range of 210–340 km s^{-1}. Furthermore, Mackey et al. (2013) calculated membership probabilities for the candidates, finding $P_{mem} \gtrsim 99\%$ in most cases; the lowest value is $P_{mem} = 92\%$ for ACS-053 (see their Table 2).

Spectroscopic observations of 20 NGC 1846 RGB stars were obtained during three nights, 2008-11-30, 2008-12-01 and 2008-12-02 under ESO programme 082.D-0387 (PI: Mackey). These were obtained with the FLAMES instrument, which is a fibre-fed multi-object spectrograph mounted on the 8m ESO/VLT telescope. A total of 4 wavelength settings were employed (Table 4.1), with three high-resolution settings (HR11, HR13, and HR14B) and one low-resolution one (LR02). The RGB stars observed, selected by Mackey et al. (2013) from their HST photometry, are sufficiently bright ($V \leq 19$) that sufficient S/N for high-precision abundance analysis is obtained. The CMD in Figure 4.1 shows the HST photometry from Mackey et al. (2013) for the NGC 1846 cluster members studied here. The data are well represented by a Dartmouth RGB isochrone assuming literature values for the cluster metallicity and age ([Fe/H] = -0.47, 1.95 Gyr; Goudfrooij et al. 2009). The lower panels in Figure 1 of Mackey et al. (2013) also show the location of additional stars in the cluster CMD.

We reduced the original raw FLAMES data with the standard ESO GIRAFFE pipeline (esoreflex, version 2.16.7; Blecha et al. 2000). It performs all the basic reduction steps (bias removal, spectrum tracing, flat fielding, and wavelength calibration) together with sky and cosmic-ray subtraction. We did not account for the telluric lines in our spectra as they did not seem to interfere with the abundance measurements of our stars. In the last step, all exposures taken for each star are

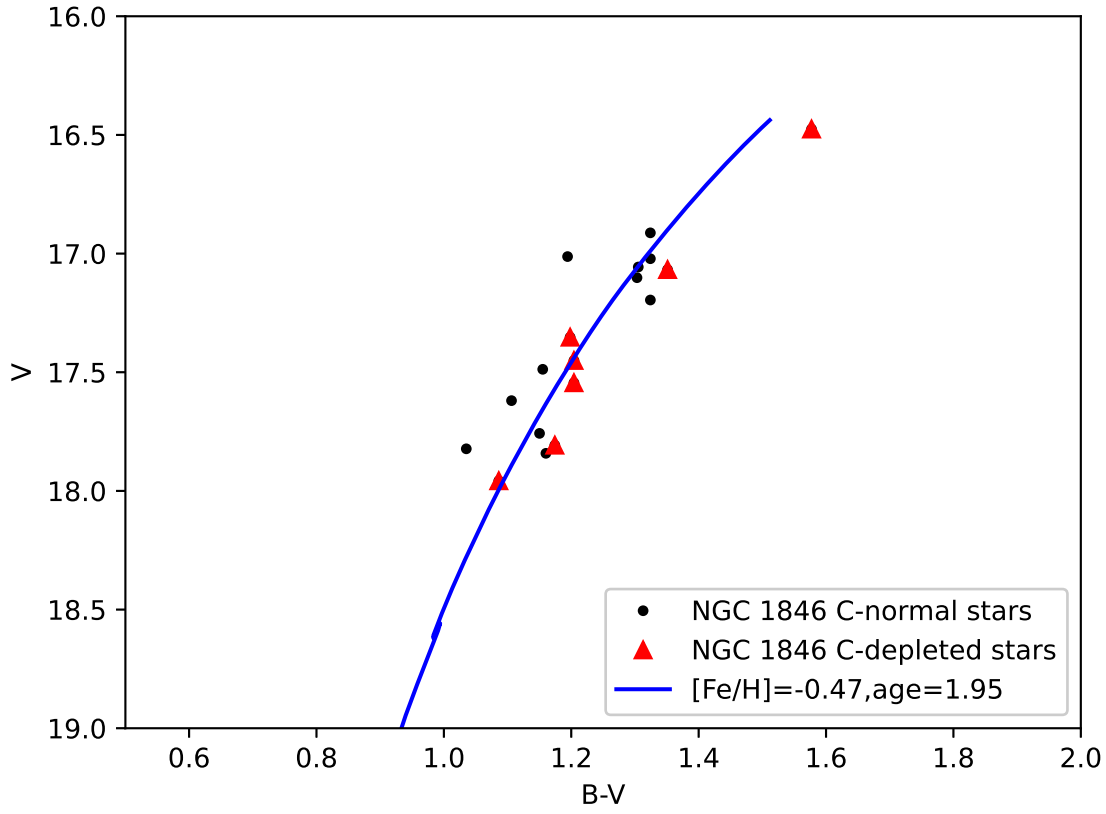

Figure 4.1: CMD of the NGC 1846 targets using B and V photometry from HST photometry presented by Mackey et al. (2013). ACS-043 and ACS-059 do not have B photometry, hence their values are omitted from the diagram. The red triangles indicate carbon depleted stars while the black points indicate carbon normal stars. This will be discussed in detail in Section 4.2. The Dartmouth RGB isochrone assumes literature values for the metallicity and age ([Fe/H] = −0.47, 1.95 Gyr; Goudfrooij et al. 2009) has been included for reference.

combined via simple addition to form the final spectra for analysis. [1]

4.3.2 Abundance zero-point correction using Arcturus

To obtain a reliable comparison of our measured abundances to the literature values, we must ensure that any systematic effects are accounted for. One way to do this is to apply our methods to the well-studied metal-poor Milky Way giant Arcturus (HD 124 897, α Boo) to obtain a zeropoint for our abundance scale. Since it has similar stellar parameters to the stars in the NGC 1846 sample ($T_{\rm eff} = 4286\,{\rm K}$, $\log g = 1.66$, [Fe/H] = −0.52) (Ramírez & Allende Prieto 2011) and has also been used in other studies comparing the abundances of LMC stars (Van der Swaelmen et al. 2013),

[1] As described in Mackey et al. (2013), the observations used the same optical fibre for the same star, and it was found that the change in barycentric correction during the period of observation is negligible.

Table 4.1: Observational setup for the spectroscopic data.

Setting	Wavelength range (Å)	Resolution
HR11	5597–5840	24200
HR13	6120–6405	22500
HR14B	6383–6626	28800
LR02	3964–4567	6000

Arcturus is a good choice as a benchmark for our study.

We simulated Arcturus spectra in the four settings (LR02, HR11, HR13 and HR14B) by using the high resolution (R $\sim$ 150,000) (Hinkle et al. 2000) spectral atlas of Arcturus. This was degraded according to the resolution required for each setting. The reference Arcturus abundances used are from Ramírez & Allende Prieto (2011) and Worley et al. (2009).

4.4 Photometric and Spectroscopic analysis method

4.4.1 Stellar parameters

The surface gravities ($\log g$) for our NGC 1846 sample were derived canonically as shown in Equation (4.1) below:

$$\log\left(\frac{g}{g_{\odot}}\right) = \log\left(\frac{M}{M_{\odot}}\right) + 4\log\left(\frac{T_{\rm eff}}{T_{\odot}}\right) + 0.4(M_{\rm bol} - M_{\rm bol\odot}). \tag{4.1}$$

The steps we took were: Assuming masses of $\sim 1.5 M_{\odot}$ for the RGB stars, calculating the bolometric magnitudes using the absorption corrected V magnitudes from HST (E(B-V) = 0.036; Mackey et al. 2013), bolometric corrections described in Alonso et al. (1999) and assuming the LMC distance modulus to be 18.52 ± 0.1 mag (Kovacs 2000). The solar bolometric reference value and effective temperature were taken to be 4.74 (Mamajek et al. 2015) and 5770 K respectively. An initial effective temperature ($T_{\rm eff}$) estimate was also provided using G–K_s colour-temperature calibrations (using extinction corrected Gaia G and 2MASS K_s magnitudes) from Casagrande et al. (2021).

$T_{\rm eff}$ was then derived by interpolating our $\log g$ values onto a Dartmouth $T_{\rm eff}$–$\log g$ isochrone (Dotter et al. 2008) using reddening corrected V magnitudes from HST photometry, assuming literature values for metallicity and age ([Fe/H] = -0.47,

Table 4.2: Stellar parameters for the NGC 1846 RGB stars. Coordinates and photometry are detailed in Mackey et al. 2013.

Name	$T_{\rm eff}$ (K)	$\log g$	[Fe/H]	$v_{\rm mic}$ ($\rm km\,s^{-1}$)
ACS-001	3940	0.89	-0.63	1.25
ACS-013	4166	1.27	-0.63	1.57
ACS-017	4250	1.42	-0.57	1.61
ACS-025	4291	1.48	-0.59	1.40
ACS-030	4357	1.59	-0.63	1.46
ACS-036	4431	1.72	-0.55	1.54
ACS-043	4462	1.77	-0.52	1.52
ACS-046	4547	1.92	-0.59	0.99
ACS-047	4516	1.86	-0.52	1.30
ACS-053	4534	1.89	-0.68	1.47
ACS-059	4588	1.99	-0.50	1.06
ACS-066	4638	2.08	-0.59	1.38
ACS-080	4212	1.35	-0.62	1.43
ACS-081	4216	1.36	-0.60	1.50
ACS-082	4231	1.38	-0.67	1.45
ACS-085	4236	1.39	-0.61	1.52
ACS-090	4395	1.66	-0.60	1.25
ACS-092	4410	1.68	-0.58	1.32
ACS-102	4540	1.90	-0.61	1.26
ACS-112	4468	1.78	-0.65	1.04

1.95 Gyr; Goudfrooij et al. 2009).[2] We tested the G–K_s colour-temperature calibrations as mentioned earlier and found good agreement with our derived temperatures, where our mean bias and standard deviation are 20 K and 90 K respectively. This dispersion is similar to the median uncertainty in $T_{\rm eff}$ from G–K_s ($\sim$ 120 K). Given our methodology, it is not straightforward to determine the precision in stellar parameters. To estimate the precision for $T_{\rm eff}$, we first interpolated the targets' V magnitude using the Dartmouth isochrone (from section 2.1) given a fixed B-V value. The new V magnitude was applied to recalculate the $\log g$ value, which was then used to determine a new $T_{\rm eff}$ value. After which, we derived the offset between the recalculated and the actual $T_{\rm eff}$ values, and its median absolute deviation was found to be 51 K.

Finally, the metallicities and $v_{\rm mic}$ values for the NGC 1846 RGB stars were determined spectroscopically by fitting Fe I & Fe II lines as described in the next section.

[2]The values from Goudfrooij et al. (2009) were obtained from fitting the CMD derived from the HST photometry.

4.4.2 Abundance analysis

High-resolution Abundance analysis

For our spectroscopic analysis, we used the spectrum synthesis code Spectroscopy Made Easy (SME) (version 536) (Piskunov & Valenti 2017) and 1D MARCS model atmospheres (Gustafsson et al. 2008). We implemented NLTE corrections using pre-tabulated grids of departure coefficients for O, Na, Mg, Si, Ca, Ba (Amarsi et al. 2020) and Fe (Amarsi et al. 2022). The rest of the elemental abundances were computed assuming LTE. We used atomic and molecular line data from VALD3 (Ryabchikova et al. 2015).

Continuum and line masks were defined mostly by hand, by inspecting a number of spectra to avoid features that appeared too blended or influenced by telluric contamination. The continuum was fitted by dividing the observations by a synthetic spectrum, and fitting a straight line in selected continuum windows. This was done for segments of ~ 50 Å in length. The Fe lines that were used to estimate [Fe/H] were carefully chosen depending on how well the synthetic spectra fit the observed ones. Since the Fe lines found in the HR13 setting were found to be of the best quality amongst all the high-resolution settings, we decided to use the $v_{\rm mic}$ values derived from that setting. As SME performs a global χ^2 fit between synthetic and observed spectra, we determined [Fe/H] individually from each setting and adopted their average as our final metallicity. We chose this approach on the basis that the other elements are located in the various spectrograph settings, and therefore the average Fe value is more representative than using the Fe value from one particular setting. For other elements, we implemented a similar approach to that of Fe. However, a key difference is that in cases where an element could be measured in several settings, we picked the setting that yielded the smallest formal errors.

Low-resolution Abundance analysis

A grid of synthetic spectra were used for our low-res spectroscopic analysis to measure carbon. Spectra were computed as described in Nordlander et al. (2019), using a grid of MARCS model atmospheres (Gustafsson et al. 2008), the synthesis code TurboSpectrum (v15.1; Plez 2012), atomic line data from VALD3 (Ryabchikova et al. 2015) and with molecular data for CH (Masseron et al. 2014) and CN (Brooke et al. 2014; Sneden et al. 2014) as well as numerous other molecules. We adopted a metallicity-dependent alpha enhancement based on typical values in the Milky Way's disk, $[\alpha/\mathrm{Fe}] = -0.4[\mathrm{Fe/H}]$, that matches the adopted model atmosphere grid (i.e. [alpha/Fe] ≈ 0.2 at [Fe/H] ≈ -0.5), and computed spectra over a range of $v_{\rm mic}$,

[C/Fe] and [N/Fe] values for each model atmosphere in the grid.

The same stellar parameters were used as for the high-res analysis. We fitted spectra using a χ^2 minimisation, and used a maximum likelihood analysis to ensure detections were significant above the noise level. The continuum and molecular absorption regions were carefully chosen, with the latter being the CH G-band found at ∼4300 Å. As for nitrogen, we were not able to obtain any reliable abundance measurements as tests on the CN band (4120–4216 Å) showed that it was not possible to provide meaningful constraints on the N abundance.

4.4.3 Error analysis

We estimated total uncertainties for the abundance measurements by combining statistical and systematic errors. We adopted statistical error estimates from the χ^2 minimisation routine for our high and low-res abundances measurements. Both use the Levenberg-Marquardt χ^2 optimisation and we take σ^2 from the diagonal of the covariance matrix.

The systematic errors are based on uncertainties in the stellar parameters. Due to the high precision in the V magnitudes, the scatter in $T_{\rm eff}$ itself is minimal. Hence, we assume the correlated error between $T_{\rm eff}$ and $\log g$ to be the leading error term, where $T_{\rm eff}$ and $\log g$ vary in tandem. Taking the error in $T_{\rm eff}$ to be 50 K as described in section 3.1, we find that a shift of 50 K in $T_{\rm eff}$ along the isochrone corresponds to a 0.1 dex change in $\log g$. We note that there is an additional error term in the $T_{\rm eff}$ and $\log g$ scales, due to uncertainties in the adopted reddening, distance modulus, mass and metallicity. But these are comparable to the precision that we derived earlier (∼0.1 dex for $\log g$ with a correlated 50 K error in $T_{\rm eff}$), and would have a similar impact on all stars, leading to negligible star-to-star abundance differences. The $v_{\rm mic}$ and [Fe/H] errors were calculated by adopting the standard deviations of the $v_{\rm mic}$ ($0.2\,{\rm km\,s^{-1}}$) and [Fe/H] measurements (0.05 dex) respectively. In comparison, we find that perturbing $T_{\rm eff}$ and $\log g$ leads to relatively minor changes in $v_{\rm mic}$ ($0.02\,{\rm km\,s^{-1}}$) and [Fe/H] (0.01 dex). These uncertainties were then used to perturb the stellar parameters and compute the change in abundance measurements, which were combined in quadrature to compute the total systematic uncertainty. Finally, the total error was calculated by simply combining the statistical and systematic errors in quadrature.

Table 4.3: The chemical composition estimated for Arcturus in this work, reference abundances by (Ramírez & Allende Prieto 2011) (1) and (Worley et al. 2009) (2), and the offsets we applied to match the literature abundance scale.

Element	This work	Literature	Offset	Ref
[C/Fe]	−0.08	0.42	−0.50	1
[O/Fe]	0.50	0.50	0.00	1
[Na/Fe]	0.33	0.11	0.22	1
[Mg/Fe]	0.68	0.37	0.31	1
[Si/Fe]	0.12	0.33	−0.21	1
[Ca/Fe]	0.09	0.11	−0.02	1
[Ti/Fe]	0.26	0.27	−0.01	1
[Fe/H]	−0.73	−0.52	−0.21	1
[V/Fe]	0.25	0.20	0.05	1
[Zr/Fe]	0.13	0.01	0.12	2
[Ba/Fe]	0.06	−0.19	0.25	2
[Eu/Fe]	0.36	0.36	0.00	2

4.4.4 Obtaining final abundance measurements

We provide both raw and calibrated abundances. The latter is to account for the systematic trend between the abundance and $T_{\rm eff}$ that occurs for some elements. This is done by fitting a straight line to the measurements and removing the slope while retaining the mean. The slopes are provided in appendix 4.6 in units of dex/1000K. Finally, offsets were applied to our measured abundances by using the Arcturus abundance measurements to obtain the zero-point corrections for each element as shown in Table 4.3. Unless otherwise specified, we will use the calibrated and zero-point corrected abundances in the rest of our analysis.

4.5 Constraining the presence of Multiple Populations in NGC 1846

In this section, we will present the results showing the lack of evidence for chemical inhomogeneities in Na and O in NGC 1846, indicating there is no evidence for multiple populations present in the cluster. We also present the upper limits for the star-to-star intrinsic abundance scatter for all elements measured.

4.5.1 Cluster mean abundances and star-to-star variations

Figure 4.2 and Table 4.4 indicate the observed star-to-star spreads and mean abundances respectively for all measured elements. To determine the intrinsic scatter of

Table 4.4: The mean calibrated abundances and the median absolute deviation (MAD) for all elements, plus the spectral regions in which the measured lines occur. The standard error of the mean is also given; systematic errors are not accounted for in these values.

Element	Mean	MAD	Spectral region(s)
[C/Fe]	0.10 ± 0.01	0.12	LR02
[O/Fe]	0.25 ± 0.02	0.06	HR13
[Na/Fe]	-0.24 ± 0.02	0.05	HR13
[Mg/Fe]	0.01 ± 0.02	0.07	HR13
[Si/Fe]	0.11 ± 0.02	0.11	HR13
[Ca/Fe]	-0.12 ± 0.01	0.03	HR14B
[Ti/Fe]	-0.03 ± 0.01	0.05	HR14B
[Fe/H]	-0.59 ± 0.01	0.04	HR11, HR13, HR14B
[V/Fe]	-0.32 ± 0.02	0.07	HR13
[Zr/Fe]	-0.13 ± 0.02	0.10	HR13
[Ba/Fe]	0.37 ± 0.02	0.05	HR13
[Eu/Fe]	0.39 ± 0.03	0.09	HR14B

the abundance measurements that may be hiding beneath the combined errors, we used a Markov Chain Monte Carlo (MCMC) code (Foreman-Mackey et al. 2013) to determine the maximum likelihood value of the intrinsic spread in abundance ratio [X/Fe] for each element. This was done by simulating the total spread in our measurements which combines the statistical, systematic and intrinsic dispersion in quadrature. A uniform prior was adopted. Contour plots were also generated for easier visualization of the data.

Outliers were removed from our data by applying statistical thresholds, which were either if the residual from a straight line fit exceeds 3 σ of the residual sample, or if the difference between the abundance and mean exceeds three times of the combined measurement error. We do not know the actual cause of the outliers even after inspecting the respective spectral regions, and they do not appear to be due to systematic errors in stellar parameters. We therefore choose a conservative approach of reporting the status of the outliers, but do not speculate further on the cause.

We have found that the star-to-star dispersion is comparable to the measurement uncertainties for most of the elements, which means that the intrinsic star-to-star spreads for these elements are small (median $\sigma_{\rm int} \leq 0.04$) as shown in Table 4.5. The only exceptions are for Zr, Si and C. For Zr and Si, we can attribute this to the relatively large measurement uncertainties based on the standard deviation of the intrinsic abundance dispersion (≥ 0.03), and note that is not unusual for a false positive at the 2 sigma confidence level to arise in a sample of 20 tests. C will be further elaborated in section 4.3.

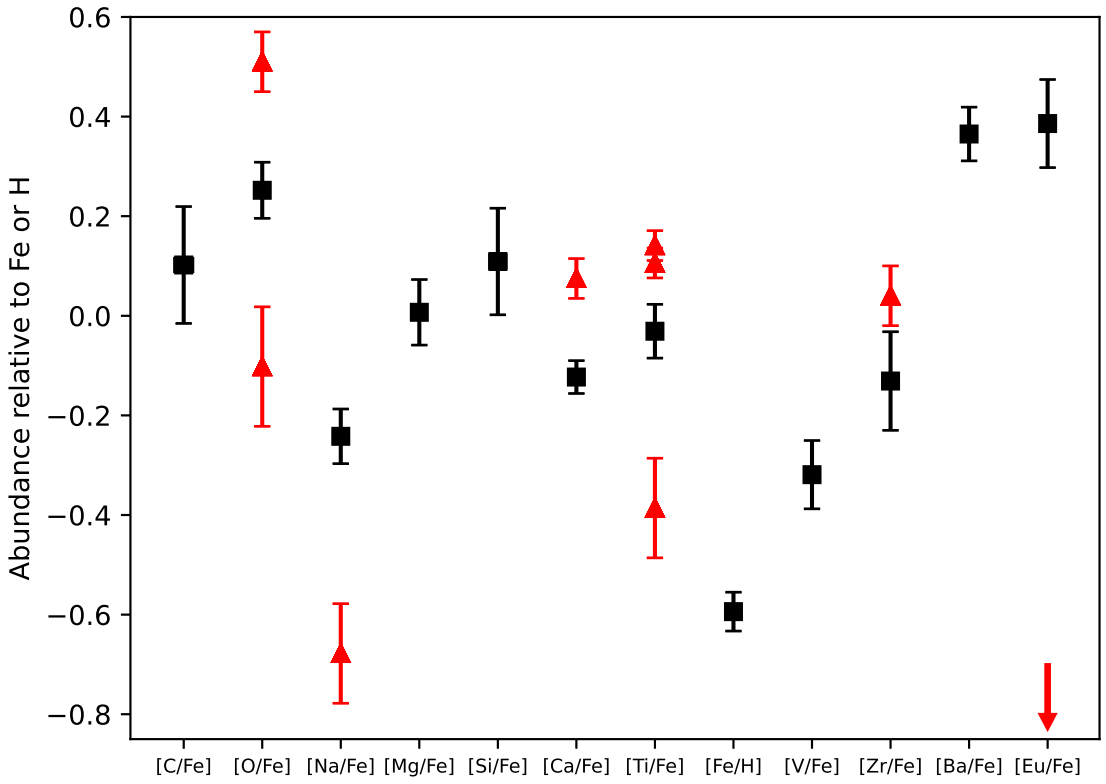

Figure 4.2: Results of the abundance analysis, represented as a scatter plot, where the black squares indicate the median abundance value and the error bars indicate the median absolute deviation. The red triangles represent outlier points together with their total measurement errors. The outlier for Eu has [Eu/Fe] $= -2 \pm 5$ and is indicated by the red arrow; this is not a genuine detection as indicated by the extremely large error estimate. The outlier stars are: O (ACS-059, ACS-066), Na (ACS-053), Ca (ACS-046), Ti (ACS-001, ACS-066, ACS-112), Zr (ACS-001) and Eu (ACS-059).

Table 4.5: Columns showing the median intrinsic dispersion ($\sigma_{\rm int}$), number of stars included in the sample, twice the standard deviation of the intrinsic dispersion (2 SD($\sigma_{\rm int}$)), and 95 % confidence limit on the maximum $\sigma_{\rm int}$ for each element measured.

Element	$N_{\rm stars}$	Median $\sigma_{\rm int}$	2 SD($\sigma_{\rm int}$)	95 % limit on $\sigma_{\rm int}$
[C/Fe]	20	0.14	0.05	≤ 0.19
[O/Fe]	18	0.04	0.05	≤ 0.09
[Na/Fe]	19	0.02	0.04	≤ 0.07
[Mg/Fe]	20	0.02	0.03	≤ 0.06
[Si/Fe]	20	0.07	0.08	≤ 0.13
[Ca/Fe]	19	0.02	0.03	≤ 0.05
[Ti/Fe]	17	0.04	0.04	≤ 0.07
[Fe/H]	20	0.02	0.03	≤ 0.05
[V/Fe]	20	0.02	0.04	≤ 0.07
[Zr/Fe]	19	0.05	0.07	≤ 0.12
[Ba/Fe]	20	0.02	0.03	≤ 0.05
[Eu/Fe]	19	0.04	0.06	≤ 0.10

The abundances of Na and O obtained from our high-res spectroscopy show no sign of any anti-correlation, as shown in Figure 4.3, which also shows literature data for Milky Way Globular Clusters from Carretta et al. (2009). The formal maximum-likelihood analysis constrains the spreads in O and Na to be $\sigma_{\rm int} \leq 0.09$ and ≤ 0.07 dex at 95 % confidence, respectively, as shown in Table 4.5. Corner plots for Na, Mg and O are included in Appendix 4.9. This confirms that there is no evidence for MPs in NGC 1846.

4.5.2 Carbon analysis

Our maximum-likelihood analysis indicates that C is the only element that exhibits a robust non-zero star-to-star spread, as shown in the corner plot in Figure 4.4. While some other elements in the scatter plot (Figure 4.2) apparently show a comparable spread, their measurement uncertainties are commensurately larger (Refer to Table 4.7 in the appendix).

To support our finding, we show in Figure 4.5 a spectral segment in the vicinity of the CH G-band for two NGC 1846 RGB stars (ACS-081 & ACS-082) that have similar stellar parameters but which have significantly different [C/Fe] (values of –0.25 vs 0.20).

We also observe a decreasing C abundance with decreasing log(g) based on Figure 4.6, which we interpret as a signature of evolutionary mixing. Potential mixing processes include thermohaline mixing and meridional circulation that occur as stars ascend the RGB, bringing up material from deeper layers that has been processed via thermonuclear CNO burning that converts C into N (Karakas & Lattanzio 2014). However, the spread in our measurements indicates that the degree of mixing varies from star to star, even at similar log(g). This suggests an additional parameter is involved in governing the mixing process.

It is not possible using our available photometry to distinguish whether a star belongs to the RGB or the AGB. Tests with a MIST isochrone indicate that the RGB:AGB ratio in our sample is likely to be 3:1 with an even distribution as a function of $\log g$. It is therefore possible that our most C-depleted stars are AGB, while the rest are RGB. We have marked the most C-depleted stars in Fig. 4.6 and in the CMD in Fig. 4.1, which indicates that the C-depleted stars have photometry that is fully compatible with the RGB isochrone. We note in particular that at the luminosities of our stars, AGB stars are double-shell source stars but have not yet reached the regime of third dredge-up where surface carbon abundances increase. Instead, the surface carbon in these stars is expected to be similarly depleted as for our most luminous RGB stars that are approaching the RGB tip.

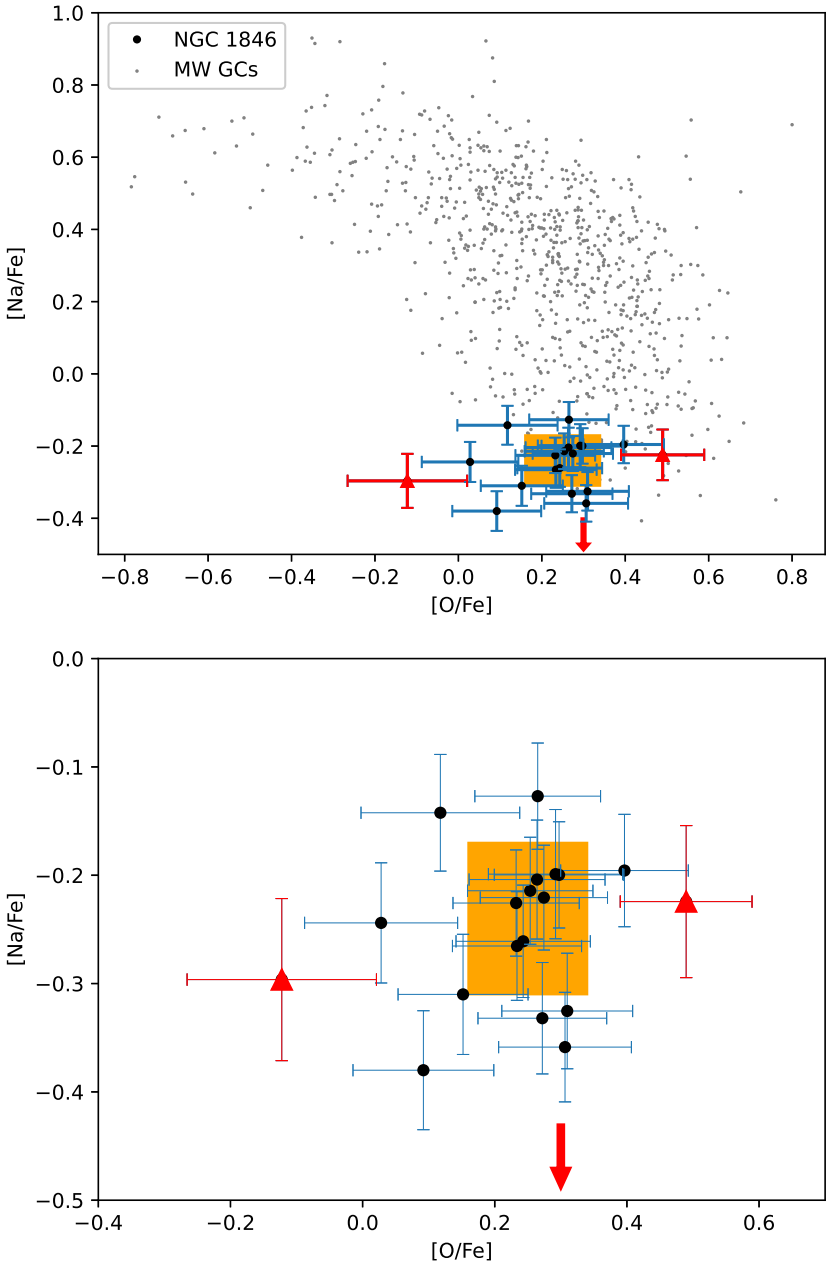

Figure 4.3: The left plot shows the comparison of the Na and O abundances in the NGC 1846 stars with literature globular cluster values (Carretta et al. 2009). Red triangles indicate the outlier points for O, while the red arrow indicates the outlier point for Na. Error bars denote the combined random and systematic uncertainties associated with each measurement. The orange shaded box covers the central 95 % of the likelihood distribution for the intrinsic spread in Na and O. The right plot shows a zoomed in version of the left plot.

One possibility is that differences in the rotation velocities of the stars can lead to varying amounts of mixing. Chanamé et al. (2005) predicts that for old field giants, a $30\,\mathrm{km\,s^{-1}}$ difference in initial rotation can lead to 0.5 dex variations in carbon abundance, with stronger rotation leading to stronger depletion, which is similar to what we observe in Figure 4.6. Moreover, as mentioned in the introduction, Kamann et al. (2020) have shown that the stars in the eMSTO region of NGC 1846 display varying surface rotation rates (60–180 $\mathrm{km\,s^{-1}}$). Inspection of our highest resolution spectra, however, show no indication of surface rotation higher than $10\,\mathrm{km\,s^{-1}}$ in any of our RGB stars. Nevertheless, even though rotation stops on the surface as the star evolves from MS to RGB, it could continue in the core, leading to mixing effects in the upper layers of the star. We note that while Chanamé et al. (2005) only predicted significant depletion of carbon in their rotating models, modern calculations do so even in non-rotating models. As discussed by Karakas & Lattanzio (2014), it is not necessarily true that diffusion coefficients from thermohaline mixing and rotation simply add together – it is possible that rotation actually inhibits thermohaline mixing, and so the effect of rotation on RGB surface abundances may be the opposite of what is discussed above.

Therefore, our results show that it is possible to have a significant intrinsic spread of surface carbon abundance in a cluster without any star-to-star variations in most of the other element abundances (including O and Na that are the characteristic signature of MPs in ancient GCs). However, we cannot rule out N variations in our sample. Since hydrogen burning conserves the sum C+N, these stars must also have varying [N/Fe]. These variations may be what has been detected in past photometric surveys of RGB stars. Measuring nitrogen abundances for our sample would thus be an important follow-up project.

4.6 NGC 1846 in the LMC context

Comparing our abundances for the NGC 1846 sample to past studies of the LMC field stars (bar and inner disc) from Van der Swaelmen et al. (2013) and the LMC intermediate-age cluster stars from Mucciarelli et al. (2008) in Figure 4.7 and 4.8, our results indicate that the chemical composition of NGC 1846 is consistent with that of the LMC, resembling more the LMC disc than the bar. This is in line with what we know about NGC 1846, since this cluster is kinematically an LMC disk object [3]. This also indicates that all the NGC 1846 stars observed are 1G rather

[3]The line-of-sight velocity of NGC 1846 (v_{rad} ∼240 $\mathrm{km\,s^{-1}}$; Mackey et al. 2013) is comparable with the LMC field's line-of-sight velocity at the position angle of the cluster with the prediction of disk rotation (van der Marel et al. 2002).

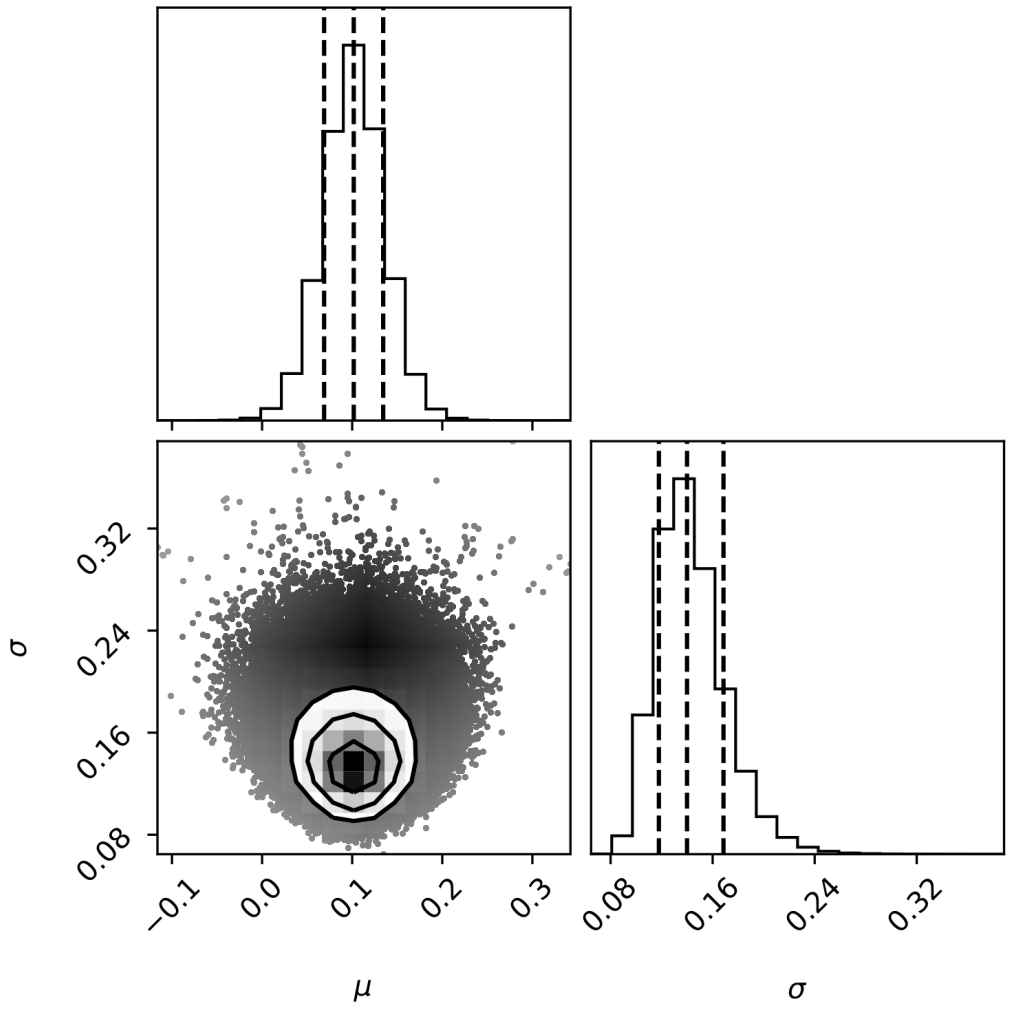

Figure 4.4: Corner plot showing the mean abundance (μ) and abundance dispersion ($\sigma_{\rm int}$) of carbon in NGC 1846. The dashed lines indicate the 25, 50 and 75 percentiles of the intrinsic spread of carbon. The median spread of carbon is 0.140 ± 0.051.

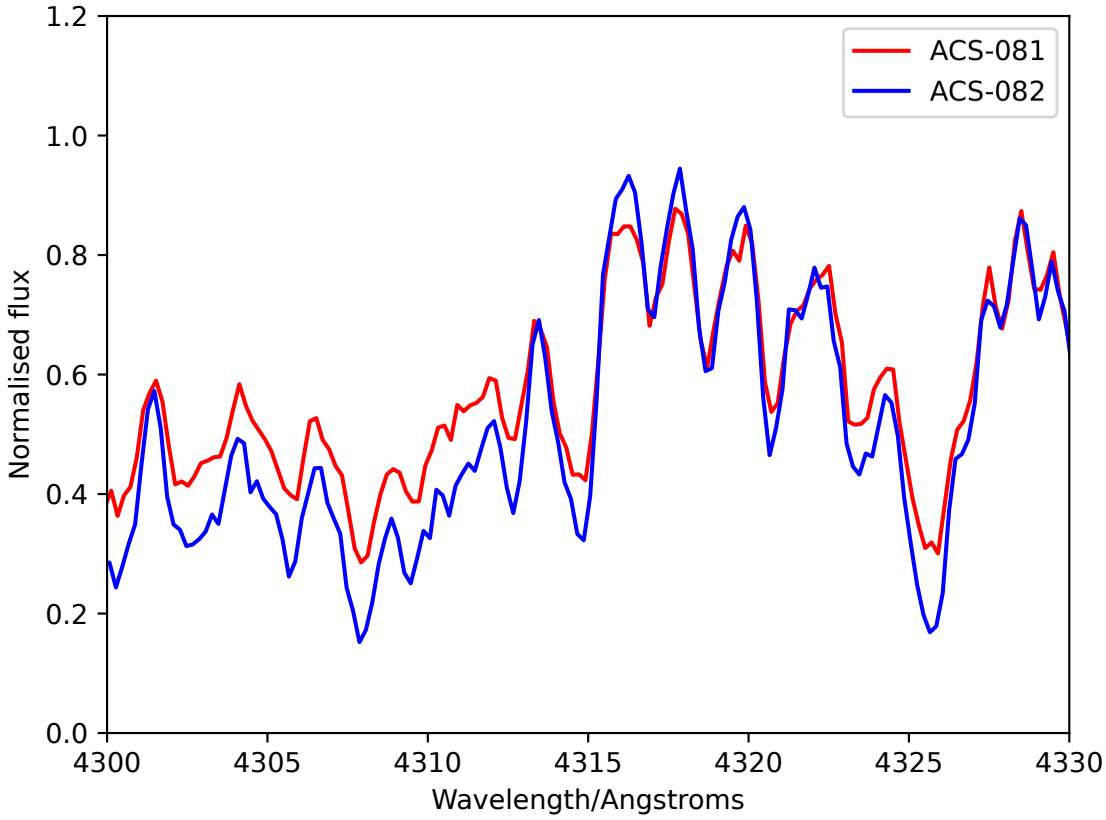

Figure 4.5: G-band spectral segment showing the difference in CH feature strength for the NGC 1846 RGB stars ACS-081 ($T_{\rm eff}$ = 4216 K) and ACS-082 ($T_{\rm eff}$ = 4231 K). The determined [C/Fe] values from synthetic spectra fits are –0.25 and +0.20, respectively.

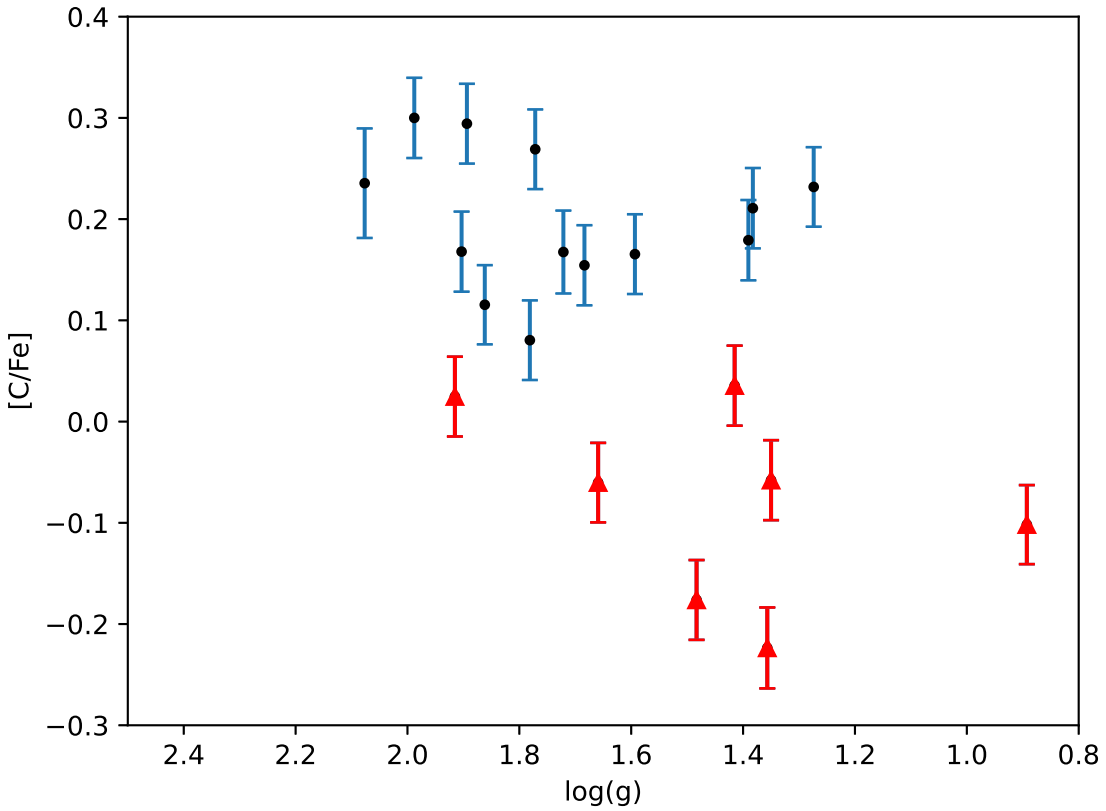

Figure 4.6: [C/Fe] vs log(g) plot for the NGC 1846 RGB sample. The red triangles indicate carbon depleted stars while the black points indicate carbon normal stars. The error bars show the combined random and systematic errors of the [C/Fe] abundance measurements for every star.

than 2G.

Our results also agree with abundances from other LMC intermediate-age clusters (NGC 1651, 1783, 1978 and 2173), with the exception of V and O. However, our NGC 1846 O abundance measurements interestingly show that they are located in the same region as the bar sample rather than with the disk. This could be due to the NLTE corrections that we used for our O abundance analysis that Van der Swaelmen et al. (2013) did not. In addition, they were only able to measure [O/Fe] in a very small number of disk stars, thus it is unclear if our abundance difference is significant or not.

4.7 Conclusions

We present detailed C, O, Na, Mg, Si, Ca, Ti, V, Zr, Ba, and Eu abundance measurements for 20 RGB stars in the LMC star cluster NGC 1846. This cluster is 1.95 Gyr old and lies just below the supposed lower age limit (2 Gyr) for the presence of multiple populations in clusters. Our measurements are based on high and low-resolution VLT/FLAMES spectra combined with photometric data from HST. Corrections for non-local thermodynamic equilibrium effects are also included for O, Na, Mg, Si, Ca, Fe and Ba. Our results show that there is no significant evidence for multiple populations in this cluster based on the lack of star-to-star spread in the Na and O abundances. However, we do detect a significant carbon abundance spread, indicating varying amounts of evolutionary mixing occurring on the RGB. This could be attributed to varying amounts of rotation which alters the amount of mixing from star to star. The general abundance patterns for NGC 1846 are similar to those seen in previous studies of LMC clusters and field stars.

Past studies on multiple populations in intermediate age clusters with similar masses ($\sim 10^5 M_\odot$) have found differing results. Mucciarelli et al. (2008) showed using VLT/UVES spectra that 4 of these clusters (NGC 1651, 1783, 1978 and 2173) spanning 1.5 to 2 Gyr in age (Goudfrooij et al. 2014; Martocchia et al. 2018) do not display obvious chemical inhomogeneities. However, in the recent decade, at least two studies have shown that some of these clusters display evidence for MPs. One example is found in the Saracino et al. (2020) study, where Na variations (~ 0.07 dex) have been found using VLT/MUSE spectra in NGC 1978, which has a similar age to NGC 1846. Furthermore, Kapse et al. (2022) recently found that NGC 2173 (~ 1.7 Gyr) also exhibits light-element abundance variations using HST photometry. Therefore, in light of our findings, further high-res spectroscopic analysis is required to confirm the above-mentioned results. Hence, the jury is still out on the extent

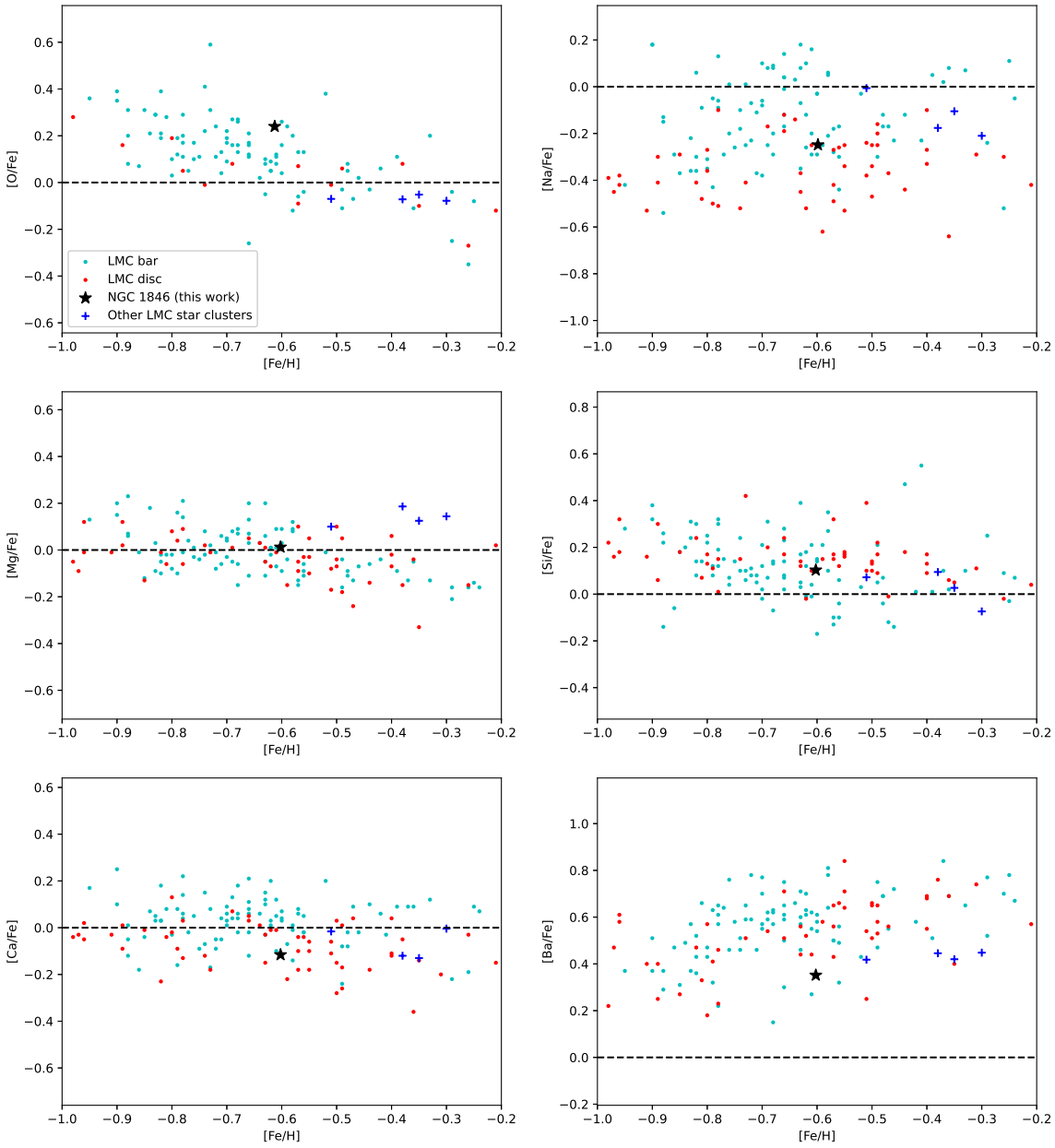

Figure 4.7: Comparison of our abundances for stars in NGC 1846 (black star) to past studies of LMC field stars (bar - cyan and inner disc - red; Van der Swaelmen et al. 2013) and for other LMC ∼2 Gyr old star clusters (blue crosses; Mucciarelli et al. 2008). Corrections for non-local thermodynamic equilibrium effects were included for these elements. The black dashed line shows the solar abundance level.

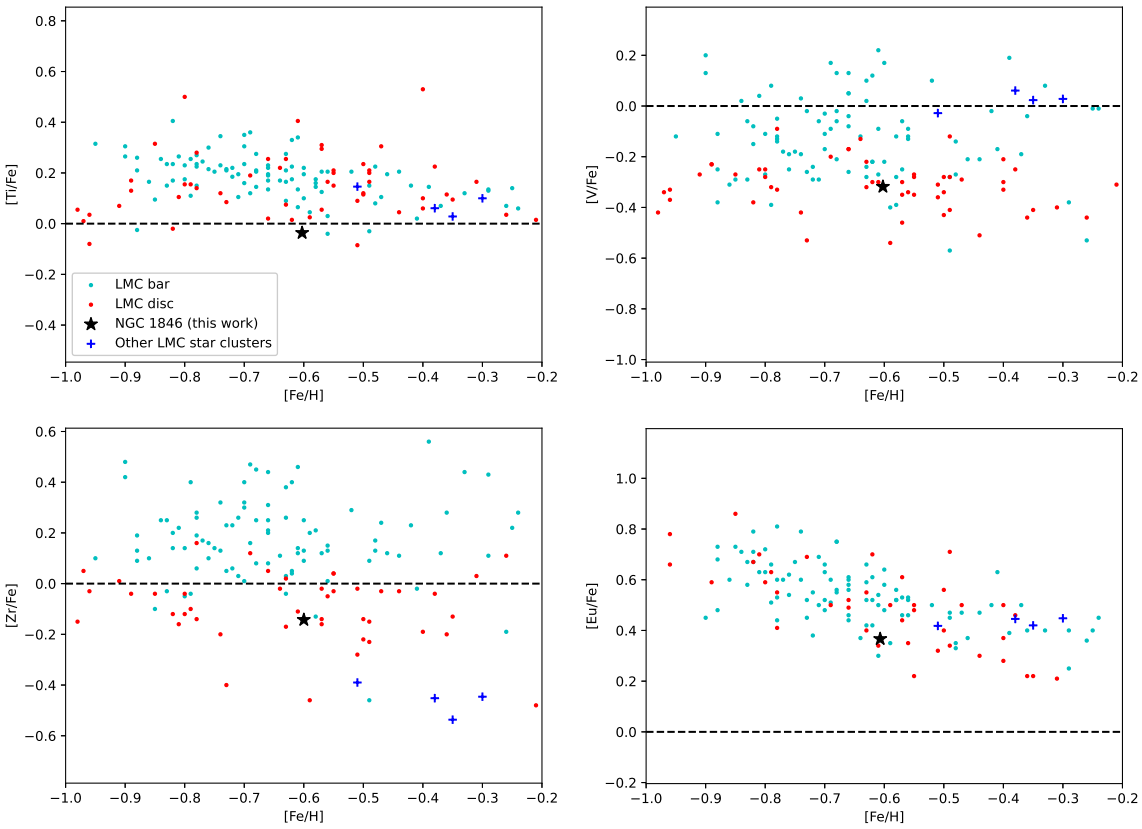

Figure 4.8: Comparison of our abundances for stars in NGC 1846 (black star) to past studies of LMC field stars (bar - cyan and inner disc - red; Van der Swaelmen et al. 2013) and for other LMC ∼2 Gyr old star clusters (blue crosses; Mucciarelli et al. 2008). No corrections for non-local thermodynamic equilibrium effects were included for these elements. The black dashed line shows the solar abundance level.

Table 4.6: Slopes of $T_{\rm eff}$-[X/Fe] for raw abundance measurements for each element.

Element	Slope (dex/1000 K)
[C/Fe]	0.454
[O/Fe]	−0.097
[Na/Fe]	0.027
[Mg/Fe]	−0.022
[Si/Fe]	0.126
[Ca/Fe]	−0.070
[Ti/Fe]	0.022
[Fe/H]	0.146
[V/Fe]	0.010
[Zr/Fe]	−0.170
[Ba/Fe]	−0.136
[Eu/Fe]	−0.290

to which detections of putative multiple populations in younger systems match the variations seen in ancient clusters.

4.8 Appendix - Additional figures

Figure 4.9 shows corner plots representing the mean abundance and abundance dispersion for Na, Mg and O in NGC 1846.

4.9 Appendix - Additional tables

We show in Table 4.6 the slopes of $T_{\rm eff}$-[X/Fe] for our raw abundance measurements. We applied calibrations to all the raw abundance measurements except for carbon.

In Table 4.7, we show calibrated abundances of the measured elements. In the online version, we also provide another table with the raw abundances in the same format.

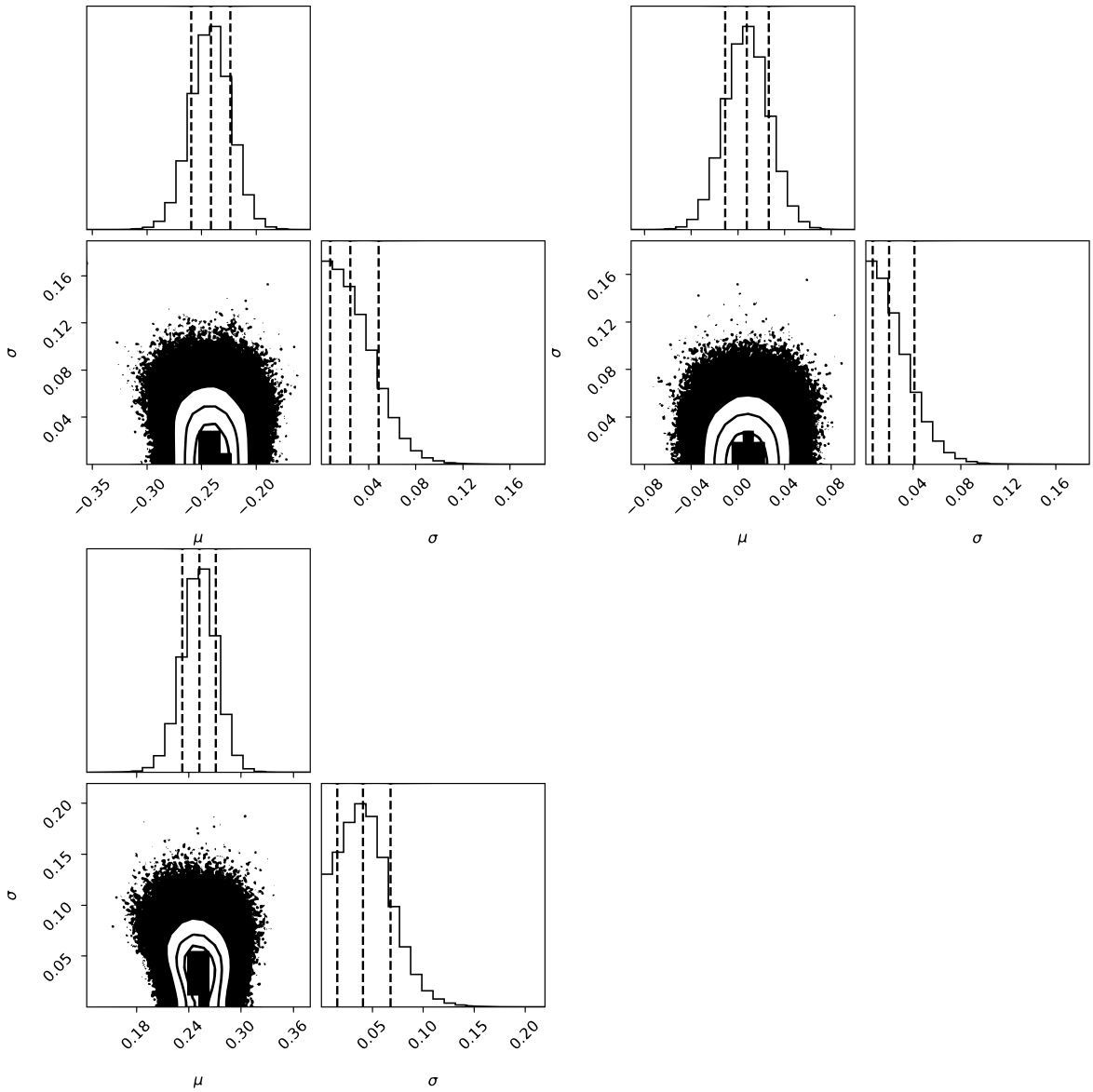

Figure 4.9: Corner plots showing the mean abundance and abundance dispersion of Na (top-left), Mg (top-right) and O (bottom) in NGC 1846. The dashed lines indicate the 25, 50 and 75 percentiles of the intrinsic spread of the different elements.

Table 4.7: Abundance table showing the calibrated abundance measurement for each star. The random and systematic errors are given for each element.

Name	$[Fe/H]_{calib}$ $[Ca/Fe]_{calib}$	$[C/Fe]_{calib}$ $[Ti/Fe]_{calib}$	$[O/Fe]_{calib}$ $[V/Fe]_{calib}$	$[Na/Fe]_{calib}$ $[Zr/Fe]_{calib}$	$[Mg/Fe]_{calib}$ $[Ba/Fe]_{calib}$	$[Si/Fe]_{calib}$ $[Eu/Fe]_{calib}$
ACS-001	$-0.565 \pm 0.008 \pm 0.100$	$0.094 \pm 0.002 \pm 0.139$	$0.112 \pm 0.032 \pm 0.068$	$-0.299 \pm 0.031 \pm 0.075$	$-0.053 \pm 0.069 \pm 0.078$	$-0.063 \pm 0.100 \pm 0.085$
	$-0.059 \pm 0.019 \pm 0.077$	$0.106 \pm 0.023 \pm 0.020$	$-0.346 \pm 0.008 \pm 0.062$	$0.040 \pm 0.025 \pm 0.062$	$0.400 \pm 0.007 \pm 0.051$	$0.246 \pm 0.050 \pm 0.062$
ACS-013	$-0.602 \pm 0.008 \pm 0.087$	$0.325 \pm 0.004 \pm 0.033$	$0.247 \pm 0.020 \pm 0.057$	$-0.122 \pm 0.017 \pm 0.066$	$0.071 \pm 0.067 \pm 0.070$	$0.277 \pm 0.053 \pm 0.067$
	$-0.218 \pm 0.019 \pm 0.029$	$-0.121 \pm 0.024 \pm 0.037$	$-0.372 \pm 0.005 \pm 0.094$	$-0.234 \pm 0.016 \pm 0.092$	$0.349 \pm 0.001 \pm 0.083$	$0.325 \pm 0.064 \pm 0.055$
ACS-017	$-0.554 \pm 0.012 \pm 0.086$	$0.091 \pm 0.007 \pm 0.028$	$0.223 \pm 0.022 \pm 0.057$	$-0.223 \pm 0.017 \pm 0.066$	$-0.027 \pm 0.040 \pm 0.051$	$0.102 \pm 0.049 \pm 0.064$
	$-0.063 \pm 0.017 \pm 0.046$	$0.039 \pm 0.023 \pm 0.036$	$-0.132 \pm 0.013 \pm 0.094$	$0.047 \pm 0.017 \pm 0.081$	$0.380 \pm 0.011 \pm 0.082$	$0.312 \pm 0.065 \pm 0.050$
ACS-025	$-0.580 \pm 0.009 \pm 0.077$	$-0.140 \pm 0.006 \pm 0.013$	$0.292 \pm 0.031 \pm 0.058$	$-0.198 \pm 0.017 \pm 0.065$	$0.035 \pm 0.061 \pm 0.055$	$0.002 \pm 0.067 \pm 0.073$
	$-0.098 \pm 0.020 \pm 0.040$	$0.062 \pm 0.028 \pm 0.028$	$-0.228 \pm 0.006 \pm 0.103$	$0.000 \pm 0.018 \pm 0.093$	$0.314 \pm 0.013 \pm 0.089$	$0.397 \pm 0.062 \pm 0.052$
ACS-030	$-0.631 \pm 0.011 \pm 0.079$	$0.172 \pm 0.006 \pm 0.031$	$0.398 \pm 0.026 \pm 0.047$	$-0.196 \pm 0.024 \pm 0.00$	$0.037 \pm 0.050 \pm 0.057$	$0.079 \pm 0.061 \pm 0.070$
	$-0.147 \pm 0.023 \pm 0.040$	$-0.111 \pm 0.036 \pm 0.037$	$-0.367 \pm 0.007 \pm 0.090$	$-0.191 \pm 0.030 \pm 0.092$	$0.372 \pm 0.015 \pm 0.088$	$0.445 \pm 0.078 \pm 0.048$
ACS-036	$-0.555 \pm 0.012 \pm 0.078$	$0.140 \pm 0.013 \pm 0.044$	$0.252 \pm 0.041 \pm 0.050$	$-0.263 \pm 0.024 \pm 0.066$	$-0.057 \pm 0.041 \pm 0.049$	$0.043 \pm 0.054 \pm 0.060$
	$-0.097 \pm 0.021 \pm 0.037$	$-0.044 \pm 0.035 \pm 0.038$	$-0.285 \pm 0.007 \pm 0.091$	$-0.076 \pm 0.026 \pm 0.093$	$0.281 \pm 0.023 \pm 0.106$	$0.409 \pm 0.085 \pm 0.048$
ACS-043	$-0.536 \pm 0.010 \pm 0.086$	$0.228 \pm 0.005 \pm 0.030$	$0.321 \pm 0.034 \pm 0.053$	$-0.328 \pm 0.027 \pm 0.073$	$-0.011 \pm 0.050 \pm 0.050$	$0.085 \pm 0.058 \pm 0.064$
	$-0.106 \pm 0.025 \pm 0.036$	$0.003 \pm 0.035 \pm 0.032$	$-0.244 \pm 0.008 \pm 0.089$	$-0.149 \pm 0.037 \pm 0.094$	$0.294 \pm 0.022 \pm 0.101$	$0.359 \pm 0.108 \pm 0.052$
ACS-046	$-0.613 \pm 0.012 \pm 0.087$	$-0.055 \pm 0.006 \pm 0.038$	$0.048 \pm 0.069 \pm 0.070$	$-0.249 \pm 0.031 \pm 0.074$	$0.061 \pm 0.057 \pm 0.052$	$0.128 \pm 0.083 \pm 0.071$
	$0.075 \pm 0.031 \pm 0.028$	$0.042 \pm 0.041 \pm 0.035$	$-0.394 \pm 0.011 \pm 0.097$	$-0.246 \pm 0.081 \pm 0.096$	$0.316 \pm 0.020 \pm 0.069$	$0.164 \pm 0.200 \pm 0.059$
ACS-047	$-0.541 \pm 0.015 \pm 0.082$	$0.050 \pm 0.003 \pm 0.077$	$0.309 \pm 0.041 \pm 0.055$	$-0.203 \pm 0.038 \pm 0.067$	$0.004 \pm 0.055 \pm 0.047$	$0.011 \pm 0.076 \pm 0.067$
	$-0.160 \pm 0.036 \pm 0.041$	$-0.053 \pm 0.057 \pm 0.043$	$-0.264 \pm 0.010 \pm 0.093$	$0.032 \pm 0.050 \pm 0.090$	$0.422 \pm 0.024 \pm 0.068$	$0.333 \pm 0.135 \pm 0.049$
ACS-053	$-0.676 \pm 0.014 \pm 0.076$	$0.221 \pm 0.006 \pm 0.035$	$0.286 \pm 0.046 \pm 0.047$	$-0.673 \pm 0.065 \pm 0.075$	$-0.122 \pm 0.068 \pm 0.047$	$-0.004 \pm 0.080 \pm 0.066$
	$-0.117 \pm 0.035 \pm 0.04$	$-0.053 \pm 0.047 \pm 0.046$	$-0.336 \pm 0.012 \pm 0.091$	$-0.308 \pm 0.096 \pm 0.096$	$0.221 \pm 0.046 \pm 0.118$	$0.337 \pm 0.194 \pm 0.041$
ACS-059	$-0.503 \pm 0.021 \pm 0.081$	$0.202 \pm 0.007 \pm 0.028$	$-0.122 \pm 0.109 \pm 0.064$	$-0.296 \pm 0.059 \pm 0.078$	$-0.014 \pm 0.060 \pm 0.050$	$0.073 \pm 0.097 \pm 0.068$
	$-0.143 \pm 0.051 \pm 0.044$	$-0.029 \pm 0.077 \pm 0.047$	$-0.228 \pm 0.013 \pm 0.099$	$-0.314 \pm 0.117 \pm 0.107$	$0.322 \pm 0.037 \pm 0.064$	$-1.460 \pm 5.316 \pm 0.984$
ACS-066	$-0.497 \pm 0.019 \pm 0.081$	$0.115 \pm 0.038 \pm 0.042$	$0.490 \pm 0.036 \pm 0.045$	$-0.224 \pm 0.053 \pm 0.074$	$0.011 \pm 0.089 \pm 0.054$	$-0.206 \pm 0.089 \pm 0.076$
	$-0.176 \pm 0.047 \pm 0.035$	$-0.381 \pm 0.083 \pm 0.070$	$-0.251 \pm 0.014 \pm 0.104$	$0.047 \pm 0.063 \pm 0.103$	$0.397 \pm 0.031 \pm 0.076$	$0.299 \pm 0.237 \pm 0.052$
ACS-080	$-0.624 \pm 0.007 \pm 0.091$	$0.014 \pm 0.006 \pm 0.036$	$0.272 \pm 0.029 \pm 0.063$	$-0.332 \pm 0.023 \pm 0.079$	$0.008 \pm 0.046 \pm 0.062$	$0.023 \pm 0.053 \pm 0.076$
	$-0.125 \pm 0.017 \pm 0.036$	$0.024 \pm 0.022 \pm 0.027$	$-0.327 \pm 0.005 \pm 0.096$	$-0.100 \pm 0.019 \pm 0.087$	$0.447 \pm 0.012 \pm 0.069$	$0.469 \pm 0.051 \pm 0.057$
ACS-081	$-0.599 \pm 0.008 \pm 0.086$	$-0.153 \pm 0.009 \pm 0.038$	$0.274 \pm 0.025 \pm 0.060$	$-0.221 \pm 0.015 \pm 0.066$	$0.010 \pm 0.046 \pm 0.057$	$0.038 \pm 0.060 \pm 0.069$
	$-0.149 \pm 0.018 \pm 0.039$	$-0.038 \pm 0.025 \pm 0.029$	$-0.307 \pm 0.005 \pm 0.090$	$-0.119 \pm 0.018 \pm 0.085$	$0.383 \pm 0.013 \pm 0.083$	$0.503 \pm 0.056 \pm 0.052$
ACS-082	$-0.674 \pm 0.009 \pm 0.08$	$0.275 \pm 0.007 \pm 0.019$	$0.254 \pm 0.019 \pm 0.058$	$-0.214 \pm 0.018 \pm 0.065$	$0.059 \pm 0.042 \pm 0.052$	$0.242 \pm 0.067 \pm 0.059$
	$-0.121 \pm 0.022 \pm 0.044$	$-0.068 \pm 0.028 \pm 0.032$	$-0.375 \pm 0.006 \pm 0.094$	$-0.121 \pm 0.024 \pm 0.089$	$0.283 \pm 0.021 \pm 0.102$	$0.570 \pm 0.057 \pm 0.047$
ACS-085	$-0.610 \pm 0.009 \pm 0.083$	$0.241 \pm 0.007 \pm 0.030$	$0.306 \pm 0.038 \pm 0.059$	$-0.359 \pm 0.021 \pm 0.076$	$0.121 \pm 0.088 \pm 0.058$	$0.251 \pm 0.049 \pm 0.057$
	$-0.112 \pm 0.022 \pm 0.036$	$-0.058 \pm 0.029 \pm 0.033$	$-0.320 \pm 0.006 \pm 0.099$	$-0.186 \pm 0.023 \pm 0.098$	$0.319 \pm 0.017 \pm 0.090$	$0.340 \pm 0.083 \pm 0.055$
ACS-090	$-0.595 \pm 0.011 \pm 0.082$	$-0.071 \pm 0.005 \pm 0.027$	$0.264 \pm 0.044 \pm 0.053$	$-0.204 \pm 0.030 \pm 0.063$	$-0.063 \pm 0.042 \pm 0.054$	$0.167 \pm 0.065 \pm 0.065$
	$-0.094 \pm 0.025 \pm 0.045$	$-0.083 \pm 0.032 \pm 0.037$	$-0.310 \pm 0.007 \pm 0.084$	$-0.113 \pm 0.031 \pm 0.086$	$0.312 \pm 0.016 \pm 0.084$	$0.457 \pm 0.072 \pm 0.046$
ACS-092	$-0.575 \pm 0.011 \pm 0.083$	$0.137 \pm 0.007 \pm 0.032$	$0.234 \pm 0.030 \pm 0.051$	$-0.265 \pm 0.020 \pm 0.073$	$-0.096 \pm 0.104 \pm 0.053$	$0.176 \pm 0.078 \pm 0.064$
	$-0.147 \pm 0.025 \pm 0.035$	$-0.053 \pm 0.040 \pm 0.034$	$-0.409 \pm 0.009 \pm 0.098$	$-0.350 \pm 0.040 \pm 0.104$	$0.389 \pm 0.018 \pm 0.071$	$0.254 \pm 0.112 \pm 0.053$
ACS-102	$-0.610 \pm 0.015 \pm 0.079$	$0.091 \pm 0.007 \pm 0.017$	$0.118 \pm 0.076 \pm 0.054$	$-0.142 \pm 0.028 \pm 0.067$	$0.091 \pm 0.058 \pm 0.046$	$0.271 \pm 0.104 \pm 0.055$
	$-0.113 \pm 0.034 \pm 0.036$	$-0.075 \pm 0.061 \pm 0.046$	$-0.473 \pm 0.014 \pm 0.099$	$-0.213 \pm 0.073 \pm 0.098$	$0.405 \pm 0.031 \pm 0.072$	$0.416 \pm 0.114 \pm 0.046$
ACS-112	$-0.651 \pm 0.014 \pm 0.082$	$0.037 \pm 0.005 \pm 0.050$	$0.092 \pm 0.052 \pm 0.051$	$-0.380 \pm 0.030 \pm 0.075$	$0.173 \pm 0.096 \pm 0.056$	$0.304 \pm 0.095 \pm 0.052$
	$0.011 \pm 0.038 \pm 0.049$	$0.143 \pm 0.051 \pm 0.027$	$-0.390 \pm 0.012 \pm 0.095$	$-0.139 \pm 0.067 \pm 0.089$	$0.376 \pm 0.033 \pm 0.061$	$0.248 \pm 0.200 \pm 0.049$

Chapter 5

Paper II: The SkyMapper search for extremely metal-poor stars in the Large Magellanic Cloud

This chapter is published as W. S. Oh, T. Nordlander, G. S. Da Costa, M. S. Bessell and A. D. Mackey, 2023. The SkyMapper search for extremely metal-poor stars in the Large Magellanic Cloud. MNRAS, 524, 577. The paper is reproduced here in full with minor formatting changes to make it consistent with the rest of the work in this thesis. The initial candidate selection from the SkyMapper data base was done by Dr. Dougal Mackey, and information on the (non)-uniformity of the v-band coverage within our selected sky area was provided by Dr. Chris Onken (RSAA, ANU). The reduction of the WiFeS spectra and the subsequent spectrophotometric fitting, yielding estimates for effective temperature (Teff), surface gravity (log g), and metallicity ([Fe/H]), were expertly conducted by Prof. Mike Bessell. The subsequent analysis and composition of the research paper were undertaken by myself, incorporating valuable insights and contributions from co-authors.

5.1 Abstract

We present results of a search for extremely metal-poor (EMP) stars in the Large Magellanic Cloud, which can provide crucial information about the properties of the first stars as well as on the formation conditions prevalent during the earliest stages of star formation in dwarf galaxies. Our search utilised SkyMapper photometry, together with parallax and proper motion cuts (from Gaia), colour-magnitude cuts (by selecting the red giant branch region) and finally a metallicity-sensitive cut. Low-resolution spectra of a sample of photometric candidates were taken using the ANU 2.3m telescope/WiFeS spectrograph, from which 7 stars with [Fe/H] ≤ -2.75 were identified, two of which have [Fe/H] ≤ -3. Radial velocities, derived from the

CaII triplet lines, closely match the outer rotation curve of the LMC for the majority of the candidates in our sample. Therefore, our targets are robustly members of the LMC based on their 6D phase-space information (coordinates, spectrophotometric distance, proper motions and radial velocities), and they constitute the most metal-poor stars so far discovered in this galaxy.

5.2 Introduction

The oldest stars in the Universe are important chemical specimens as they can potentially shed light on the formation and evolution of galaxies during the earliest epochs of star formation. One way to search for these very old stars is by looking for extremely metal-poor (EMP) stars ([Fe/H] ≤ -3.0) amongst the field populations of the Milky Way and of nearby galaxies. These second-generation stars with extremely low abundances of elements (e.g. Fe) were formed out of the gas enriched by the supernovae of their metal-free predecessors, and are able to live long enough to be observable at the present day due to their low mass. Thus, EMP stars can provide us with important, otherwise inaccessible information about the properties of some of the first stars in the Universe, as well as about the initial conditions of star formation found in young galaxies. Moreover, in the Milky Way, we can investigate how some of these stars may have entered the Galactic halo through the accretion of their original host system (see, for example, the review of Frebel & Norris 2015).

EMP stars have also been found in dwarf galaxy satellites of the Milky Way. However, such stars are often less well studied than EMP stars in the Galactic halo mainly because the large distances (20-200 kpc) of their host systems means that only the brightest red giants can currently be observed at sufficiently high signal-to-noise with high-resolution spectrographs (e.g. Frebel & Norris 2015). An example of this can be found in Skúladóttir et al. (2021), where EMP stars with metallicities down to [Fe/H] $= -4.11$ have been found in the Sculptor dwarf spheroidal galaxy. The EMP stars in dwarf galaxies are generally similar in terms of the element abundance ratios when compared to the Milky Way halo. However, there appears to be some interesting trends in key elements that appear to correlate with the mass of the galaxy. One example is found in the carbon measurements, whereby a large proportion of C-enhanced stars have been found in the Milky Way halo and ultra-faint dwarf galaxies, but only a handful of such stars have been found in classical dwarf galaxies. (e.g. Tafelmeyer et al. 2010; Ishigaki et al. 2014; Mashonkina et al. 2017; Spite et al. 2018). Additionally, while the metallicity range spanned by the bulk of stars in the Milky Way and in all classes of dwarf galaxies is similar (reaching below

[Fe/H] = −4), the ultra-faint dwarf galaxies seem to lack stars with [Fe/H] ≥ −1.5 (Chiti et al. 2018).

The Large and Small Magellanic Clouds are the largest Milky Way satellites. Despite their importance to many fields of galactic archaeology (e.g. Nidever et al. 2017), not much is known about their EMP star populations. The lowest metallicities of current Magellanic samples do not reach the same extremely low metallicities seen in either the Milky Way halo or in the less massive dwarf satellites. The most metal-poor star known in the LMC, as reported in the literature, has [Fe/H] = −2.7 (Reggiani et al. 2021). Interestingly, this study also found that the most metal-poor Magellanic stars in their sample are r-process enhanced relative to the Milky Way, implying differences in chemical enrichment processes or timescales. This emerging field of chemical abundance analysis has motivated us to initiate a dedicated, sensitive search for EMP stars in the Magellanic Clouds.

Currently, one of the most efficient ways of searching for EMP stars is by using the SkyMapper telescope, which is conducting an imaging program spanning the entire southern sky in 6 filters (Onken et al. 2019). A unique feature of SkyMapper is its v filter, which allows the identification of stars with [Fe/H] ≤ −2.5 by means of a metallicity-sensitive colour-colour diagram. This has been used to search for EMP stars in the Milky Way with very high efficiency (≥ 40% of photometrically-selected candidates having [Fe/H] ≤ −2.75; e.g., Da Costa et al. 2019; Chiti et al. 2020; Yong et al. 2021a), leading to the discovery of several ultra-metal poor stars ([Fe/H] ≤ −4.0), including the lowest ever detected abundance of iron in a star (SMSS J160540.18–144323.1; [Fe/H] = −6.2; Nordlander et al. 2019) and the most iron-poor star known (SMSS J031300.36–670839.3; [Fe/H] ≤ −6.5; Keller et al. 2014).

In this study, we used SkyMapper photometry to conduct a search for EMP stars across the Magellanic system. In particular, we focused on the LMC as it is closer compared to the SMC, which allows us to obtain better quality data. Our photometric EMP selection imposed parallax and proper motion cuts (from Gaia), colour-magnitude diagram (CMD) cuts (by selecting the RGB region) and finally a metallicity-sensitive cut. We obtained low-resolution spectra of a sample of photometric candidates, and used a spectrophotometric analysis to yield metallicity measurements with a precision of ≤0.3 dex. Radial velocities, derived from the CaII triplet lines, have also been determined for all candidates in our sample to compare with the systemic velocity of the LMC.

We present the selection method for the EMP candidates in Section 5.3 and our observation, data reduction and spectrophotometric analysis methods in Section 5.4.

In Section 5.5, we present the abundance results for our EMP candidates, and confirm that they are likely members of the Large Magellanic Cloud.

5.3 Photometric selection

5.3.1 Initial selection

The LMC EMP candidates were chosen from the SkyMapper Southern Sky Survey Data Release DR3[1], which consists of photometry for over 600 million objects covering a total area of more than 24,000 deg^2 across all six SkyMapper optical filters: u, v, g, r, i, z (Wolf et al. 2018; Onken et al. 2019). We focused on a region that is 5–20 degrees in radius from the LMC centre (Equation 5.1) to avoid crowding in the inner parts of the dwarf galaxy.

The initial selection from the DR3 database used similar parameters to the ones used in Da Costa et al. (2019) for consistency. The only difference is in the brightness cut, where $g_{\rm psf} \leq 16.5$ so that the LMC candidates can be observed at high dispersion on 8m-class telescopes with sensible integration times.

In addition, we have an advantage in our selection as we know that our desired targets should be located in the LMC. Therefore, we cross-matched our photometric EMP selection sample with Gaia DR2 (Gaia Collaboration et al. 2018a), updated to DR3 (Gaia Collaboration et al. 2021) after data acquisition, to impose further cuts using parallax and proper motion information. The adopted cuts are shown in Equations 5.2 and 5.3, respectively. In particular, Equation 5.3 was determined quantitatively, where we measured the average proper motion and spread for stars located $2^\circ - 6^\circ$ from the LMC centre (to avoid kinematics from the core and contamination from the Milky Way halo). We selected the central 90 percentiles of the proper motion distribution. The cuts we adopted were as follow,

$$5^\circ \leq \cos^{-1}(\sin(\delta)\sin(\delta_c) + \cos(\delta)\cos(\delta_c)\cos(\alpha - \alpha_c)) \leq 20^\circ \tag{5.1}$$

where $\delta_c = -69.78^\circ$ and $\alpha_c = 81.28^\circ$,

$$-0.2'' \leq \pi \leq 0.2'' \tag{5.2}$$

$$\sqrt{1.7(\mu_\alpha - 1.80)^2 + 0.8(\mu_\delta - 0.37)^2} \leq 1.0. \tag{5.3}$$

We note that the centres of the distributions are offset from the Gaia DR2 mean

[1]The data can be accessed via `https://skymapper.anu.edu.au`

values as provided in Gaia Collaboration et al. (2018b). This is due to asymmetries in the proper motion distribution.

5.3.2 Final adopted selection

Given our EMP selection method is a tried and tested method as demonstrated in Da Costa et al. (2019, see Fig. 3), we have adopted a similar final selection window in terms of the colour as well as the metallicity index of our candidates (Fig. 4.1). In particular, we have selected targets with $0.7 \leq (g-i)_0 \leq 1.2$ since the RGB at lower metallicities ([Fe/H] ≤ -2.5) does not go beyond $(g-i)_0 \approx 1.2$ mag for an old age ($\geq \sim$10 Gyr) population. The blue colour cut is applied because we want to avoid contamination from young approximately solar metallicity disc dwarfs in the bluer parts of the CMD. As for the metallicity index cut, we have decided to use $m_i \geq -0.2$ as previous studies have shown that stars with metallicity indices more negative than this value are often young stars with Ca II H+K emission, or extragalactic objects such as QSOs and active galactic nuclei (Da Costa et al. 2019). The upper (positive) bound on the metallicity index selection was set by the location of the [Fe/H] $= -2$ Dartmouth isochrone for an age of 12.5 Gyr and [α/Fe] $= 0.4$ (Dotter et al. 2008) in this colour-colour diagram.

From a total of around 20,000 candidates in our initial selection, our final adopted selection trims the list down to just 30 candidates. Candidates were prioritised for observing based on their brightness, their relative distance to the [Fe/H] $= -4$ isochrone in the metallicity-sensitive diagram and on their location in the CMD as shown in Fig. 5.1. As shown in Fig. 5.2, the depth of the DR3 v-band coverage within our annular selection region is not by any means uniform. In particular, the v-band coverage in terms of depth reached for e_v_psf < 0.2 mag is significantly worse on the western side of the selection region, particularly for $\alpha \leq 4$ hrs and $-75^\circ \leq \delta \leq -57^\circ$ (Fig. 5.2). There are also patches of sky with similar reduced v-band depth scattered across the entire region. Consequently, we cannot in any sense claim to have generated a complete sample of LMC EMP candidates.

5.4 Observations and Data Reduction

5.4.1 Observation using ANU 2.3m/WiFeS

Spectroscopic observations of our EMP candidate stars were obtained with the ANU 2.3m telescope at Siding Spring Observatory over twelve nights, spanning from November 2020 to December 2021. Due to bad weather, useful data were obtained

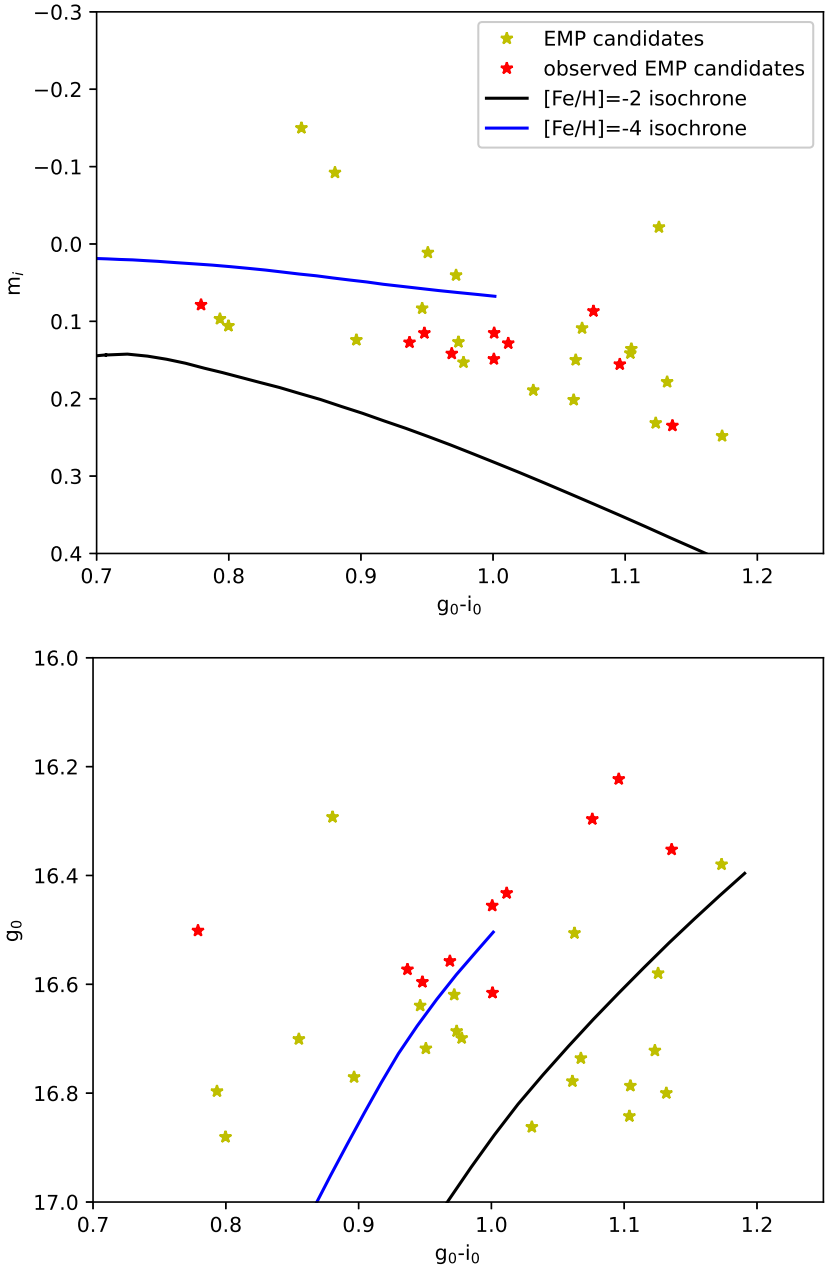

Figure 5.1: Top: Metallicity-sensitive diagram showing the Magellanic EMP candidates from our final adopted selection. The red stars represent the candidates that have been observed. The blue and black curves represent [Fe/H] = −4 and −2 Dartmouth isochrones for an age of 12.5 Gyr and [α/Fe] = 0.4 (Dotter et al. 2008). Both isochrones have been calibrated with reference to the SkyMapper DR3 data as described in Da Costa et al. (2019). Bottom: CMD with the same description as above. The isochrones have been shifted in distance modulus by 18.5 to match the LMC distance.

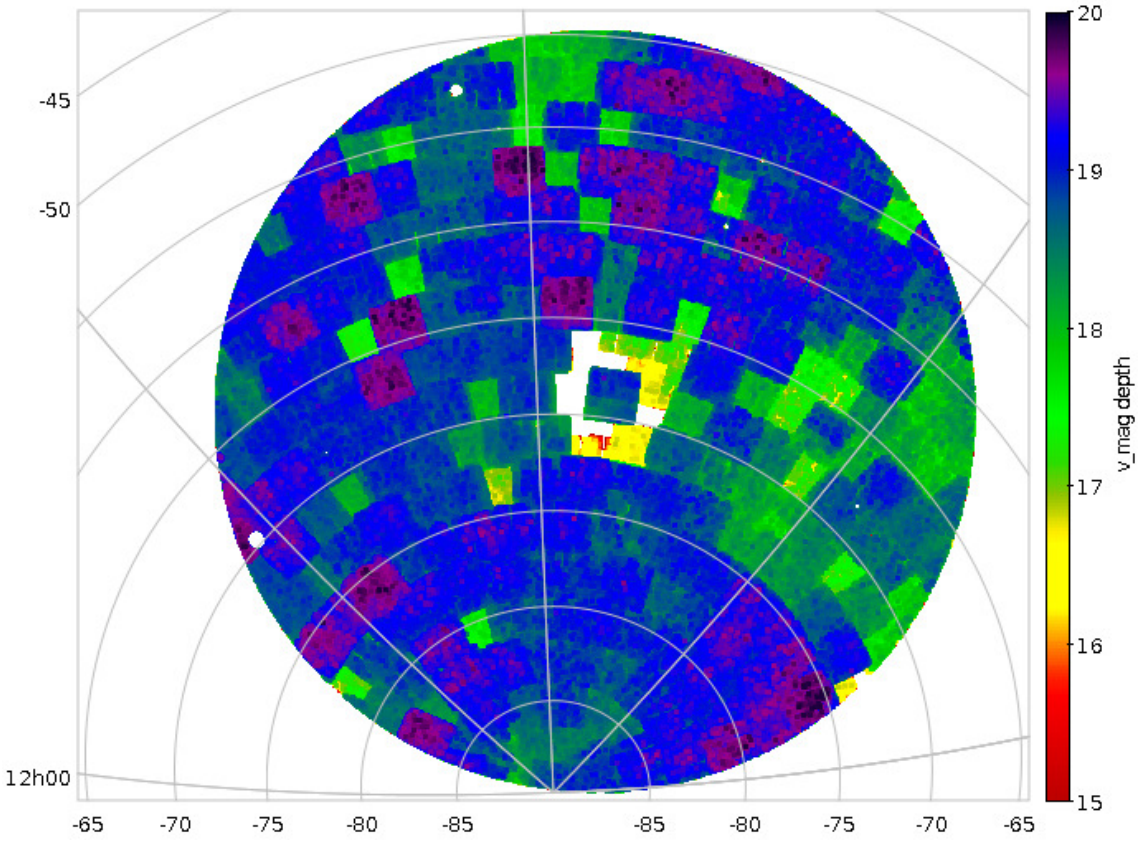

Figure 5.2: The SkyMapper DR3 v-filter coverage in the vicinity of the LMC (20 degree radius). The darker patches show areas with deeper coverage.

on about 60 percent of the allocated nights. As a result we were able to successfully observe only 10 of the 30 candidates.

The 2.3m observations were conducted with the WiFeS integral field (IFU) spectrograph (Dopita et al. 2010) using the B3000 and I7000 gratings, which cover the wavelength intervals 3200–5900 Å and 6830–9120 Å, respectively. The number behind the letter represents the spectral resolution of the gratings. Multiple 1800 s exposures were used to yield a signal-to-noise ratio (S/N) per pix in the final summed spectra of ≥ 20 for the blue spectra at the H and K lines of Ca II, and ≥ 30 for the red spectra at the Ca II triplet lines. Because WiFeS is an integral field spectrograph, useful spectra were still obtained in poor-seeing conditions.

5.4.2 Spectrophotometric fits

Similar to the process described in Da Costa et al. (2023), the raw observed spectra of each candidate were sky-subtracted, wavelength-calibrated, combined, and crucially, flux-calibrated using observations of several flux standards each night. These standards are found in Bohlin et al. (2014), and have well established flux distributions at optical wavelengths.

The flux-calibrated spectra are then compared to an extension of the grid of model fluxes discussed in Nordlander et al. (2019) using the FITTER code (Norris et al. 2013) to determine the best fit. The grid of model spectra is interpolated to a final grid step of 25 K in $T_{\rm eff}$, and 0.125 dex in log g and [Fe/H], and the results are rounded off to a maximum of 2 decimal places.

Given that the EMP candidates are assumed to be in the LMC, we utilised the LMC distance to calculate fundamental $\log g$ values which we can then compare to the $\log g$ values obtained from the spectrophotometric analysis. The fundamental $\log g$ calculation is shown by Equation 5.4 below:

$$\log\left(\frac{g}{g_{\odot}}\right) = \log\left(\frac{M}{M_{\odot}}\right) + 4\log\left(\frac{T_{\rm eff}}{T_{\odot}}\right) + 0.4(M_{\rm bol} - M_{\rm bol\odot}). \tag{5.4}$$

The steps we took were: assuming masses of $\sim 0.8\mathrm{M}_{\odot}$ for the EMP candidates, calculating the bolometric magnitudes using the V magnitudes (which was converted from G and $(G_{bp} - G_{rp})$ from Gaia DR2), bolometric corrections described in Alonso et al. (1999), using LMC reddening information from Skowron et al. (2021) and assuming the LMC distance modulus to be 18.52 ± 0.1 mag (Kovacs 2000). The solar bolometric reference value and effective temperature were taken to be 4.74 (Mamajek et al. 2015) and 5770 K respectively. The effective temperature ($T_{\rm eff}$) estimates used

were taken from the spectrophotometric analysis as described above. Our results show that the fundamental and spectrophotometric $\log g$ values display a mean offset (fundamental minus spectrophotometric) of 0.11 ± 0.03 (standard error of mean) with a standard deviation of $\sigma = 0.23$ dex. The dispersion value is comparable to the spectrophotometric $\log g$ uncertainties discussed in (Da Costa et al. 2019). The overall agreement between the $\log g$ values calculated assuming the stars are at the distance of the LMC, and the distance independent spectrophotometric values, indicates that the observed stars are indeed likely LMC members.

Apart from the EMP candidates, stars with known metallicities from high-resolution spectroscopic studies were also observed and analysed in the same way as our targets to verify the accuracy and precision of our measurements. The outcome is shown in Table 5.2. The $T_{\rm eff}$, $\log g$ and [Fe/H] values determined for these stars were compared with the ones obtained from the literature, and the mean offsets, standard error of the mean and sigma values for each stellar parameter were calculated to be 181 ± 68K ($\sigma = 84K$), 0.10 ± 0.04 ($\sigma = 0.30$) and 0.20 ± 0.07 ($\sigma = 0.38$) respectively. We note that the reference temperatures are derived either directly from photometric methods (Barklem et al. 2005; Hansen et al. 2013), or from spectroscopic methods with corrections to achieve agreement with the photometric temperature scales (Jacobson et al. 2015). Nevertheless, the dispersion values are still comparable to the ones found in Da Costa et al. (2019).

5.4.3 Radial velocities

The Ca II triplet spectral region (8580-8720 Å) was used to measure the radial velocities of the stars. This was done using fxcor in IRAF with two NGC 7099 stars (S1 & 12917) as templates. We then evaluated the zero point of our velocities by deriving radial velocities for the metallicity reference stars and comparing the velocities with their known values. The mean offset (measured minus reference) and dispersion are -0.1 km s^{-1} and 3.8 km s^{-1} respectively, indicating that the zero point uncertainty in our velocities is small. The uncertainties in the candidate velocities range from 2–11 km s^{-1}, which is derived from the fxcor velocity error. The radial velocities of our sample were then compared to the LMC rotation curve to confirm their Magellanic membership, which will be elaborated more in Section 5.5.1.

Table 5.1: Comparing the mean radial velocity rv, its standard deviation, and the residual dispersion $\sigma_{\rm res}$ (radial velocity minus rotation curve), for our sample and that of Reggiani et al. (2021). The number of stars in each sample is also given.

Sample	N	rv ($\mathrm{km\,s^{-1}}$)	$\sigma_{\rm res}$ ($\mathrm{km\,s^{-1}}$)
This work	10	284.8 ± 34.6	43.5
Reggiani et al. (2021)	9	293.7 ± 47.0	52.4

5.5 Results and Discussion

5.5.1 Magellanic membership

The radial velocity measurements of our EMP candidates were used to investigate LMC membership. As shown in Fig. 5.3, our candidates' radial velocity measurements follow the rotation curve of the outer parts of the LMC ($9^\circ - 13^\circ$ radius; van der Marel et al. 2002), which is appropriate given that our targets lie in the LMC outskirts. The agreement is quantified by the results given in Table 5.1, which compares the standard deviation of the radial velocities to the standard deviation of the residuals (radial velocity minus rotation curve). The equivalent results for the LMC members discussed in Reggiani et al. (2021) are also given in the Table. These dispersion values are comparable to the dispersion values of 30-40 $\mathrm{km\,s^{-1}}$ in the LMC outskirts given in van der Marel et al. (2002), which are based on radial velocities for ∼20 LMC carbon-star members.

We note that one star in our sample, 499901368, shows a larger divergence from the rotation curve (123 $\mathrm{km\,s^{-1}}$), and is also the star that lies substantially to the blue of the RGB in the CMD shown in the lower panel of Fig. 4.1. At 19.3°, this star is also the one with the largest angular distance from the centre of the LMC. However, it is currently unknown if the disk rotation model still applies for such large distances from the LMC centre. Cullinane et al. (2022) showed that the outer disk of the LMC is highly perturbed, leading to significant spreads in both proper motions and radial velocities (refer to Table 1 of that paper). Therefore, given that the star's radial velocity measurement is only ~ 40 $\mathrm{km\,s^{-1}}$ higher than the systemic velocity of the LMC (~ 262 $\mathrm{km\,s^{-1}}$; van der Marel et al. 2002), we are still confident that 499901368 is a member of the LMC.

Therefore, we can conclude that our candidates are likely to be LMC members due to following reasons as summarised: Targets match the systemic LMC circular velocity at their position angle; Proper motions are consistent with that of the LMC; $\log g$ values calculated under the assumption of lying at the LMC distance agree with distance-independent spectrophotometric $\log g$ values.

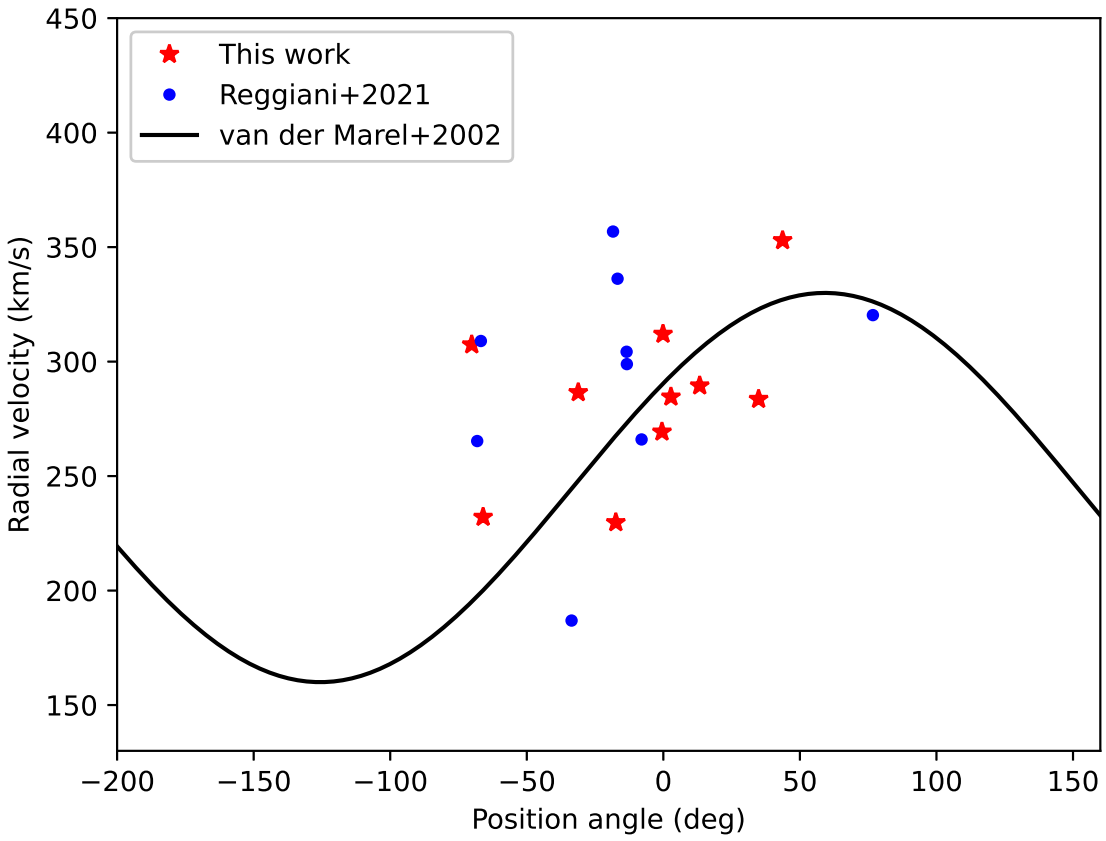

Figure 5.3: Radial velocity as a function of position angle in the LMC (measured east of north) for our LMC sample. The LMC targets from Reggiani et al. (2021) have also been plotted for reference. The black sinusoid shows the LMC rotation model derived from carbon stars in the outer LMC disk (van der Marel et al. 2002) that sit at radii similar to the majority of our EMP sample.

5.5.2 Stellar metallicities

As mentioned in Section 5.4.2, we observed a set of stars with known metallicities from high dispersion analyses to verify the accuracy of our metallicity analysis. Overall, our low-resolution spectrophotometric measurements are comparable with that of the literature as shown in Table 5.2 and Figure 5.4. We found a mean [Fe/H] difference (measured minus reference) of 0.20 ± 0.07 dex ($\sigma = 0.38$ dex). This shows that the metallicity results for our EMP candidates are consistent. The level of uncertainty is similar to that listed in Da Costa et al. (2019) and Yong et al. (2021a), where the spectrophotometric metallicities are shown to have uncertainties at the ± 0.3 dex level.

Table 5.3 shows the stellar parameters of the Magellanic EMP candidates, including their metallicities, from the spectrophotometric fits. Also given are the coordinates, radius from the LMC centre, position angle, reddening, photometry and radial velocity information. We have identified 7 stars with [Fe/H] ≤ -2.75, of which two have [Fe/H] ≤ -3. The B3000 and I7000 spectra of the most metal-poor star in our sample (499901368: [Fe/H] $= -3.25$) are shown in Fig. 5.5, with the left panel also showing the spectrophotometric fit for this star. The right panel compares the spectrum of the candidate with that for CS 31072-118 which has similar stellar parameters. Our sample thus reveals the most metal-poor stars so far discovered in the LMC.

5.5.3 Selection efficiency

Of the 10 EMP candidates that we observed, 7 (or 70%) have [Fe/H] ≤ -2.75, while 2 (or 20%) have [Fe/H] ≤ -3.00. Overall, all of the stars observed have [Fe/H] ≤ -2.00. These numbers are comparable to the ones found in Da Costa et al. (2019), and they confirm the high selection efficiency of SkyMapper photometry for identifying candidate metal-poor stars.

5.5.4 Carbon abundances

By inspecting the G-band (CH) region of the spectrophotometric fits to the blue spectra, which employ [C/Fe] $= 0$, we find no evidence of carbon enhancement in any of our EMP candidates. This is similar to the results found in Da Costa et al. (2019), which determined that the selection of metal-poor stars based on SkyMapper filters may be biased against highly carbon-rich EMP stars. As discussed in Da Costa et al. (2019), this is most likely due to large carbon enhancements affecting the metallicity index, making CEMP objects appear to be more metal-rich, and

hence not selected as potential EMP candidates.

Table 5.2: Comparing stellar parameters of the reference stars from our study with that of the literature. The reference stellar parameters are provided by 1. Barklem et al. (2005), 2. Hansen et al. (2013), 3. Jacobson et al. (2015) and 4. Harris (1996).

Object	$T_{eff,low}$	$T_{eff,lit}$	ΔT_{eff}	$\log g_{low}$	$\log g_{lit}$	$\Delta \log g$	$[Fe/H]_{low}$	$[Fe/H]_{lit}$	$\Delta [Fe/H]$	Ref
HE 0008-3842	4450	4327	123	1.00	0.65	−0.35	−3.63	−3.35	−0.28	1
CS 31072-118	4700	4606	94	1.00	1.25	0.25	−3.00	−3.06	0.06	1
CS 29491-053	4850	4700	150	1.00	1.30	0.30	−2.63	−3.04	0.41	2
SMSS J022410.38−534659.9	4800	4630	170	1.13	0.90	−0.23	−3.13	−3.40	0.27	3
SMSS J040148.04−743537.3	5100	4900	200	1.88	1.90	0.02	−2.50	−3.09	0.59	3
SMSS J022423.27−573705.1	5200	4846	354	1.13	1.60	0.47	−3.25	−3.97	0.72	3
CD -38° 245	4975	4800	175	1.25	1.50	0.25	−3.75	−4.19	0.44	2
NGC 7099-12917	4075	-	-	1.00	-	-	−2.63	−2.27	−0.36	4
NGC 7099-S1	4550	-	-	1.00	-	-	−2.38	−2.27	−0.11	4

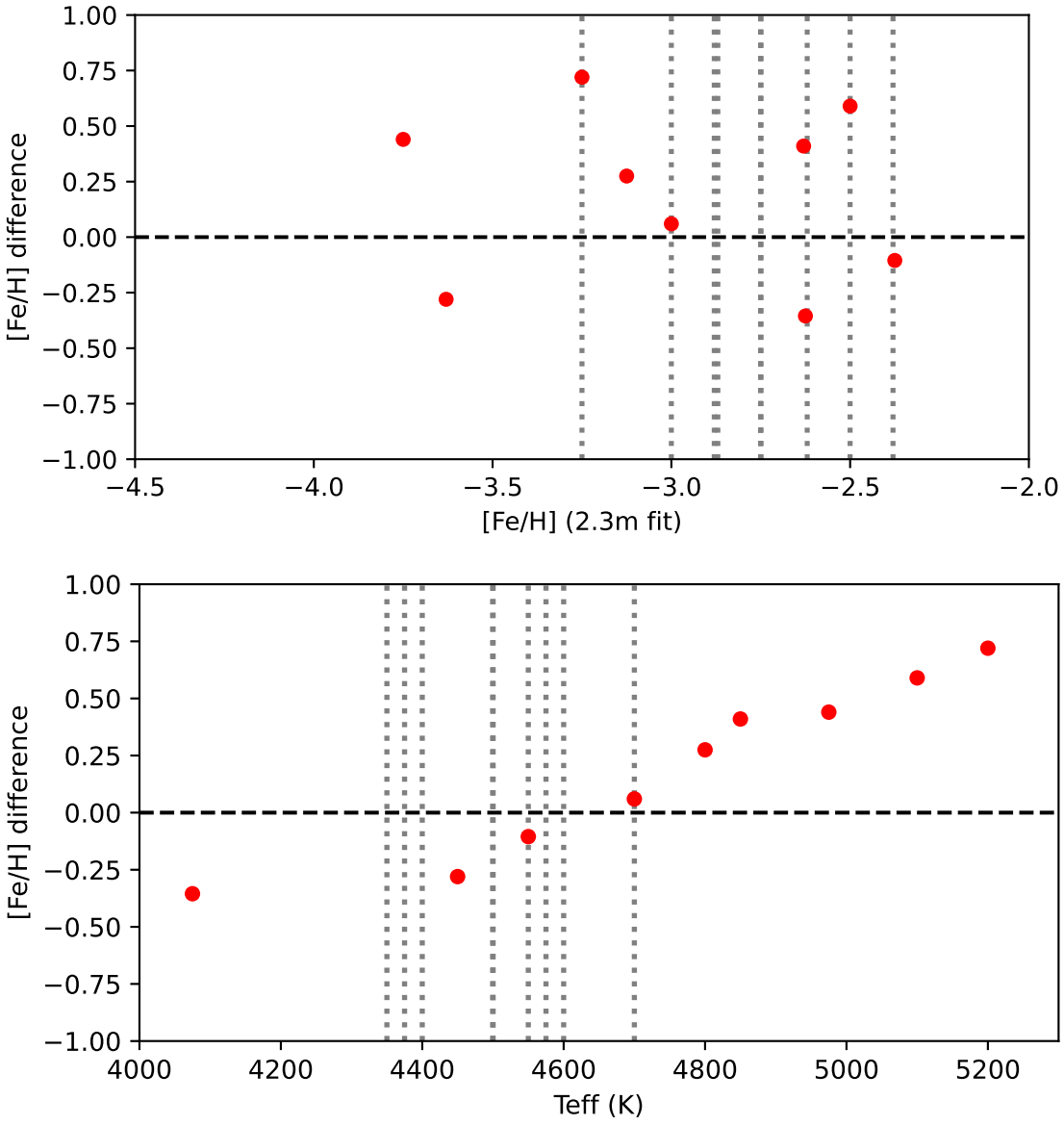

Figure 5.4: Differences in [Fe/H] between our measurements and the literature vs [Fe/H] (top panel) and $T_{\rm eff}$ (bottom panel) for the reference stars. The vertical dotted lines indicate the stellar parameters of our sample.

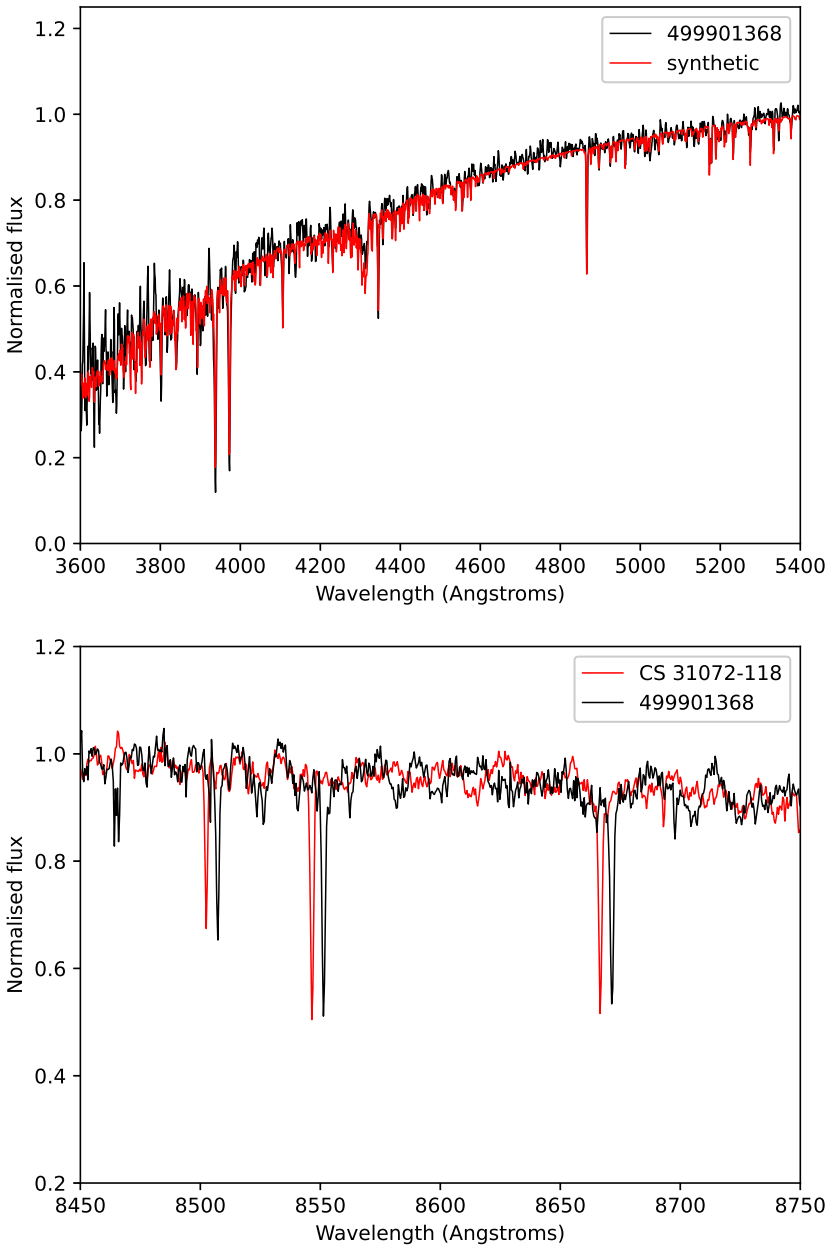

Figure 5.5: *Left*: The B3000 spectrum (black line) from the 2.3m WiFeS observations of the most metal-poor EMP candidate 499901368. The relative flux values have been normalized to unity at 5500 Å. The spectrophotometric fitting process yields 4700/1.63/−3.25 for $T_{\rm eff}$, $\log g$ and [Fe/H], respectively, and the best-fitting model spectrum is overplotted in red. *Right*: The I7000 spectrum (black line) of the same star as above, showing the Ca II triplet region. The spectrum of reference star CS 31072-118 ($[{\rm Fe/H}]_{\rm lit} = -3.06$) is overplotted in red. The spectra have not been corrected for radial velocities. Our spectrophotometric analysis of the B3000 spectrum indicates similar stellar parameters for both stars (CS 31072-118: 4700/1.00/−3.00). The close similarity of the Ca II triplet line strengths in the two observed spectra confirms the similarity of the metallicities.

Table 5.3: Complete table showing full spectrophotometric information of the LMC EMP candidates. The radius is given relative to the LMC centre at $(\alpha, \delta) = (81.28°, -69.78°)$, and the position angle is measured east of north. The photometric data was retrieved from SkyMapper DR3, including the metallicity-sensitive index $m_i = (v-g)_0 - 1.5(g-i)_0$, and was dereddened using E(B-V) derived from OGLE-IV reddening maps (Skowron et al. 2021). Stellar parameters were derived from our spectrophotometric analysis.

SMSS DR3	RA	Dec.	Radius	Angle	g_0	$(g-i)_0$	E(B-V)	m_i	$T_{\rm eff}$ (K)	$\log g$	[Fe/H]	rv ($\mathrm{km\,s^{-1}}$)
500263380	05 24 59.3	−62 48 07.4	7.0°	−0.1°	16.352	1.136	0.052	0.235	4350	0.50	−2.38	312.0 ± 2.2
471817979	06 29 57.1	−60 24 33.3	11.5°	43.7°	16.296	1.076	0.070	0.087	4375	0.50	−2.50	352.9 ± 2.5
500206265	05 43 35.5	−59 50 43.2	10.1°	13.3°	16.432	1.001	0.059	0.149	4400	1.00	−2.62	289.5 ± 7.7
471915910	06 08 14.9	−62 07 23.5	8.8°	34.9°	16.600	0.948	0.049	0.115	4575	1.00	−2.75	283.6 ± 6.9
497519424	04 54 53.6	−64 07 52.2	6.4°	−31.2°	16.616	1.001	0.036	0.115	4500	1.00	−2.75	286.5 ± 9.6
500382880	05 24 24.1	−59 16 05.5	10.5°	−0.5°	16.456	1.001	0.032	0.149	4550	1.00	−2.75	269.3 ± 6.3
497682788	04 03 47.0	−64 30 55.7	9.4°	−66.0°	16.557	0.969	0.047	0.142	4500	1.00	−2.87	232.1 ± 8.1
500287810	05 28 29.6	−61 26 49.6	8.3°	2.8°	16.223	1.096	0.050	0.155	4500	0.50	−2.88	284.6 ± 2.6
500766372	04 59 15.4	−58 54 16.0	11.2°	−17.4°	16.573	0.937	0.023	0.127	4600	1.00	−3.00	229.7 ± 6.8
499901368	03 02 07.9	−57 53 20.2	19.3°	−70.2°	16.501	0.779	0.015	0.079	4700	1.63	−3.25	307.4 ± 3.0

5.6 Conclusions

We present results of our search for extremely metal-poor (EMP) stars in the Large Magellanic Cloud via SkyMapper photometry. Our photometric selection of EMP stars involved applying cuts on parallax and proper motion (from Gaia), on the color-magnitude diagram (by selecting the red giant branch region), and a metallicity-sensitive cut. To confirm the EMP status of our photometric candidates, we obtained low-resolution spectra using the ANU 2.3m telescope/WiFeS spectrograph combination. We identified seven stars with [Fe/H] ≤ -2.75, including two with [Fe/H] ≤ -3. Radial velocities, derived from the CaII triplet lines, generally match well with the outer rotation curve of the LMC for the candidates in our sample, confirming that our targets are probable LMC members. Our results constitute the most metal-poor stars found so far in the LMC. We have obtained high-resolution spectra of the most metal-poor sample and will present our findings in a future paper.

Chapter 6

Paper III: High-resolution spectroscopic study of extremely metal-poor stars in the Large Magellanic Cloud

This chapter presents the content of W. S. Oh, T. Nordlander, G. S. Da Costa, M. S. Bessell and A. D. Mackey, 2023. High-resolution spectroscopic study of extremely metal-poor stars in the Large Magellanic Cloud. The paper is currently undergoing a review by the Monthly Notices of the Royal Astronomical Society. Support in terms of the spectroscopic analysis methods were kindly provided by Dr. David Yong and Madeleine McKenzie. The subsequent analysis and composition of the research paper were undertaken by myself, incorporating valuable insights and contributions from co-authors.

6.1 Abstract

We present detailed abundance results based on UVES high dispersion spectra for 7 very and extremely metal-poor stars in the Large Magellanic Cloud. We confirm that all 7 stars, two of which have [Fe/H] $\leq$ –3.0, are the most metal-poor stars discovered so far in the Magellanic Clouds. The element abundance ratios are generally consistent with Milky Way halo stars of similar [Fe/H] values. We find that 2 of the more metal-rich stars in our sample are enhanced in r-process elements. This result contrasts with the literature, where all nine metal-poor LMC stars with higher [Fe/H] values than our sample were found to be rich in r-process elements. The absence of r-process enrichment in stars with lower [Fe/H] values is consistent with a minimum delay timescale of ∼100 Myr for the neutron star binary merger process to generate substantial r-process enhancements in the LMC. We find

that the occurrence rate of r-process enhancement (r-I or r-II) in our sample of very and extremely metal-poor stars is statistically indistinguishable from that found in the Milky Way's halo, although including stars from the literature sample hints at a larger r-II frequency the LMC. Overall, our results shed light on the earliest epochs of star formation in the LMC that may be applicable to other galaxies of LMC-like mass.

6.2 Introduction

Extremely metal-poor (EMP) stars ([Fe/H] ≤ -3.0) are some of the oldest stars that we can currently observe in the Universe. Although they are not the first-generation stars formed out of the original gas from the Big Bang, EMP stars still play a key role in terms of uncovering the properties of the first stars in the Universe. This is because they are second-generation stars that were formed out of gas enriched by the supernovae of their metal-free predecessors. EMP stars can help us understand the formation and evolution of galaxies during the early epochs of star formation, as they can reveal information about the properties of the first stars and the initial conditions of star formation in young galaxies (e.g. Frebel & Norris 2015).

Dwarf galaxies, which are smaller and less massive than their larger counterparts, serve as ideal laboratories for the study of EMP stars. Due to their relatively simple stellar populations, low metallicities and low stellar densities, dwarf galaxies provide an optimal environment for identifying and investigating these rare stars. However, the study of EMP stars in this environment has generally been quite limited due to observational challenges in terms of analysing stars in these distant objects (20-200 kpc) relative to the Milky Way. As such, EMP stars with metallicities down to only [Fe/H] $= -4.11$ have been discovered in dwarf galaxies (Skúladóttir et al. 2021). This is in contrast to the study of EMP stars in the Galactic halo, where the lowest ever detected iron abundance in a star (SMSS J160540.18–144323.1; [Fe/H] $= -6.2$; Nordlander et al. 2019) and the most iron-poor star known (SMSS J031300.36–670839.3; [Fe/H] ≤ -6.5; Keller et al. 2014) have been found. Furthermore, EMP stars in dwarf galaxies have been found to show some significant differences in key elements (e.g. C, Na, and n-capture elements) compared to the Milky Way halo, which could be attributed to the lower masses (e.g. Tafelmeyer et al. 2010; Ishigaki et al. 2014; Mashonkina et al. 2017; Spite et al. 2018).

Ultra-faint dwarf galaxies (UFDs), which are smaller and less luminous compared to the Milky Way's other dwarf galaxy satellites, present another interesting envi-

ronment to study EMP stars. While the metallicity range of the Milky Way halo and dwarf galaxies is comparable, there seems to be a notable absence of stars with [Fe/H] ≥ -1.5 in the UFDs (Chiti et al. 2018). Additionally, investigations of the Grus I and Triangulum II UFDs revealed a significant deficiency in neutron capture elements, leading to the inference that the primary source of these elements lies in infrequently occurring processes (Ji et al. 2019). In contrast, the UFD Reticulum II was found to be r-process enhanced (Ji et al. 2016; Ji et al. 2023), implying that the chemical enrichment and star-formation history timescales for these objects, compared to more luminous dwarfs and Milky Way-type galaxies, have not yet been adequately constrained.

The Large and Small Magellanic Clouds are two of the most prominent Milky Way satellites, but little is known about their EMP star populations despite their significance in various fields of galactic archaeology (e.g. Nidever et al. 2017). Currently, the lowest metallicities found in the Magellanic Clouds are not as extreme as those observed in the Milky Way halo or dwarf satellites (e.g. Reggiani et al. 2021, Oh et al. 2023). Additionally, Reggiani et al. (2021) found that all of the metal-poor Magellanic stars in their sample, which range from -2.4 to -1.5 in [Fe/H], are r-process enhanced. In particular, their sample was found to display significant offsets ($\sim 4\sigma$) in the r-process element europium relative to the Milky Way at comparable [Fe/H]. This has significant implications, suggesting that the Magellanic clouds experienced r-process enrichment events on timescales longer than core-collapse supernovae timescales but shorter than Type Ia supernovae timescales (Reggiani et al. 2021). This result might also be a consequence of the isolated evolution and prolonged history of accretion from the cosmic web of the Magellanic Clouds. This growing field of chemical abundance analysis has thus prompted a thorough analysis of EMP stars in the Magellanic Clouds.

In this paper, we conduct a high-resolution spectroscopic analysis with UVES on the ESO VLT of a sample of seven LMC stars that were initially selected based on SkyMapper photometry. Using a method similar to that of Da Costa et al. (2023), the stars were followed up using low-resolution spectroscopy on the ANU 2.3m telescope, which produced a list of seven stars with metallicities [Fe/H] ≤ -2.75 (Oh et al. 2023). These stars constitute the most metal-poor stars so far discovered in this dwarf galaxy.

We present our sample selection, observations and data reduction in Section 6.3. In Section 6.4, we present the stellar parameter determination and the spectroscopic analysis methods for our EMP candidates. In Section 6.5, the abundance results of our measurements are presented and discussed, including interpreting the results in

terms of nucleosynthesis timescales.

6.3 Sample Selection, Observations and Data Reduction

6.3.1 Sample selection

As described in Oh et al. (2023), the targets were chosen based on SkyMapper photometry. Parallax and proper motion cuts (from Gaia), colour-magnitude cuts (by selecting the red giant branch region) and a metallicity-sensitive cut were also applied to the sample. The stars were subsequently observed at low resolution using the WiFeS integral field spectrograph at the ANU 2.3m telescope (Oh et al. 2023). Additional information regarding the photometric selection and WiFeS spectroscopy process can be found in Da Costa et al. (2019). To determine estimates of effective temperature ($T_{\rm eff}$), surface gravity ($\log g$), and metallicity ([Fe/H]), a spectrophotometric flux fitting method was applied to the WiFeS spectra, using the methodology first described in Bessell (2007) and Norris et al. (2013). The LMC membership of our candidates was also determined using their measured radial velocities (Oh et al. 2023).

6.3.2 Observations and Data Reduction

Our 7 best candidates (most metal-poor based on the WiFeS spectra) were then observed (Programme ID: 108.22D8) using the high-resolution Ultraviolet and Visual Echelle Spectrograph (UVES; Dekker et al. 2000) mounted on the Very Large Telescope (VLT) operated by the European Southern Observatory. The wavelength range, slit width and resolving power for the blue arm were 3289–4525 Å, 1.0 arcsec and 40,000 respectively. For the red arm, the values were 4780–6801 Å, 0.6 arcsec and 67,000. The spectroscopic observations were obtained over a few nights in service mode, spanning from August 2021 to January 2022. Each star was observed for 3 hours and 20 minutes in total, resulting in a final S/N per binned pixel of around 20 and 38 at 3360 Å and 3900 Å respectively for the blue arm, and 46 and 70 at 5006 Å and 6296 Å respectively for the red arm.

We extracted the reduced data, processed with UVES pipeline version 5.10.13, from the ESO portal. The pipeline executes a comprehensive set of reduction procedures, encompassing bias correction, spectrum tracing, flat fielding, wavelength calibration as well as sky and cosmic ray removal. A single continuous spectrum was then generated for each star by coadding and merging multiple exposures. Finally, the

spectra were continuum normalised by fitting high-order polynomials to the fluxes. Further information on the reduction and continuum normalisation process can be found in Yong et al. (2021a).

6.4 Analysis

6.4.1 Stellar parameters

We first obtained the spectrophotometric temperatures of our LMC stars from Oh et al. (2023). We then corrected these values by 50 K to account for the systematic offset between the spectrophotometric low-resolution analysis and accurate temperatures from Balmer lines and the infrared flux method. See Norris et al. (2013) and Yong et al. (2021a) for more information.

Given that the EMP candidates are assumed to be in the LMC, we utilised the LMC distance to calculate fundamental $\log g$ values. This was calculated by using the canonical formula as shown in Oh et al. (2023). The $\log g$ error was then estimated by assuming an error in mass of 0.2 $M_{\odot}$, 100 K in $T_{\rm eff}$, 0.2 mag in distance modulus and 0.02 mag in E(B-V). Given that the maximum uncertainty contribution to $\log g$ from each term is ~ 0.05 dex, we have decided to adopt a conservative uncertainty estimate of 0.3 dex.

6.4.2 Spectroscopic analysis

The set of model atmospheres utilised in this study was obtained from the α-enhanced ($[\alpha/\mathrm{Fe}] = +0.4$), NEWODF grid of ATLAS9 models developed by Castelli & Kurucz (2003). We adopt solar abundances from Asplund et al. (2009). The equivalent widths of a specific set of lines were determined for all the stars in our sample by fitting a Gaussian line profile according to the method described in McKenzie et al. (2022). More information about the model atmosphere and the list of lines analysed in this work can be found in Yong et al. (2021a).

We used the MOOG LTE stellar line analysis program to determine the iron abundances using Fe I and Fe II lines. The microturbulent velocity, $v_{\rm mic}$, was determined by ensuring that the abundances from Fe I lines exhibit no trend relative to the reduced equivalent width, $\log(W_{\lambda}/\lambda)$.

Our method also compared the inferred metallicity from MOOG with the assumed metallicity used to generate the model atmosphere. If the difference between the two exceeded 0.2 dex, an updated model atmosphere using the new [Fe/H] value was computed. This was iterated until the derived stellar metallicities converged.

Additionally, Fe I lines that deviated from the median abundance by more than 0.5 dex or 3σ (based on the line-to-line scatter) were removed.

With the metallicities of our 7 stars obtained, we then computed the abundances for 24 elements. For Na, Mg, Al, Si, Ca, Sc, Ti (Ti I & Ti II), Cr, Mn, Co, Ni, Sr, and Ba, this was done by measuring the equivalent widths of the lines and using MOOG to infer the abundances of each element. For the remaining 11 elements that were analysed, namely C (CH), N (CN), O, Zn, Zr, Y, La, Nd, Sm, Eu, and Dy, we measured the abundances by generating synthetic spectra via MOOG and adjusting their abundances until the synthetic spectra best fit the observed spectra. For Zn, Zr, Y, La, Nd, Sm, Eu, and Dy (which were not measured in Yong et al. 2021a), the list of lines analysed was based on Sneden & Cowan (2003).

Despite the potential effects of non-local thermodynamic equilibrium (NLTE) on abundance ratios, we opted to adopt LTE results for our analysis. This was due to the fact that our comparison studies also analysed their samples using LTE (Jönsson et al. 2020; Yong et al. 2021a; Reggiani et al. 2021). While NLTE corrections can be crucial for accurately determining abundances in certain cases, we aimed to maintain consistency with the existing literature to allow a more meaningful comparison.

6.4.3 Error analysis

The statistical error was calculated by first estimating the uncertainty in the equivalent width measurement, using an analytic formula from Cayrel (1988):

$$\sigma_{\mathrm{w}} = \frac{2.3\sqrt{\mathrm{w} * \mathrm{p}}}{\mathrm{S/N}} \tag{6.1}$$

where w is the line full width at half maximum (FWHM), p is the pixel wavelength step and S/N is the signal-to-noise ratio per pixel. Then, we calculated the change in abundance measurements by re-running the abundance analysis using the equivalent width that was adjusted by the uncertainty value.

We also estimate the systematic impact on abundances from random errors in stellar parameters ($T_{\mathrm{eff}} \pm 100\,\mathrm{K}, \log g \pm 0.3\,\mathrm{dex}, v_{\mathrm{mic}} \pm 0.3\,\mathrm{km\,s^{-1}}, [\mathrm{M/H}] \pm 0.3$), which are based on Oh et al. (2023), Da Costa et al. (2023) and Yong et al. (2021a). The random uncertainty in the abundance and abundance ratios were then calculated by first perturbing, in turn, each adopted stellar parameter by its estimated uncertainty, and then combining the effects into a total random error via a sum of squares process. The typical values for the random errors are ~ 0.15 dex.

We found that the statistical errors were, in general, at least an order of magnitude

smaller than the random errors due to the uncertainties in stellar parameters and the line-to-line scatter. Hence, we only use and present the latter errors, including in the supplementary material provided with the online version.

6.4.4 Radial velocities

The radial velocities were determined by comparing the observed wavelengths of the lines (which come from the line centre of the fitted Gaussian profiles), for which equivalent widths were measured, with their corresponding rest wavelengths. The average standard deviation of these measurements was found to be 0.7 $\mathrm{km\,s^{-1}}$. We also evaluated the zero point of our velocities by comparing our measurements with that of Oh et al. (2023) which measured radial velocities for the same stars but using the Ca II triplet region with medium-resolution ($R \approx 7,000$) spectra. The mean offset (measured minus medium-resolution reference) and standard deviation are -1.2 $\mathrm{km\,s^{-1}}$ and 10.8 $\mathrm{km\,s^{-1}}$ respectively, indicating that the medium-resolution velocities used for membership selection are reliable with a small zero point uncertainty. Table 6.1 provides the IDs, adopted atmospheric parameters and the radial velocities of our targets.

6.5 Results and Discussion

6.5.1 Stellar metallicities

We have analysed high-resolution UVES spectra of 7 stars that are likely members of the LMC. We find metallicities in the range [Fe/H] = -2.49 to -3.13, including two stars with [Fe/H] < -3. The typical metallicity uncertainties are ~ 0.09 dex. In comparison to our low-resolution metallicities, the offsets between the two types of measurements (high-resolution minus low-resolution) show a mean and standard deviation of 0.04 and 0.24 dex respectively. This is in line with the results from Oh et al. (2023) and Da Costa et al. (2019), which state that the low-resolution metallicity measurements are precise to the 0.3 dex level. Thus, we can confirm that our medium-resolution selection reliably selects the most metal-poor stars, and all 7 stars are the most metal-poor stars analysed at high resolution in the LMC, and 2 are revealed as the first LMC EMP stars.

6.5.2 General comparison with the Milky Way halo

Table 6.2 and Figures 6.4 to 6.8 show the results of our abundance measurements compared to the results from a Milky Way halo sample (Cayrel et al. 2004; Jacobson

Table 6.1: Coordinates and stellar parameters of the LMC very and extremely metal-poor stars.

SMSS DR3	Gaia DR3	RA/H:M:S	Dec./deg:min:sec	g_0	$(g-i)_0$	E(B-V)	$T_{\rm eff}$/K	$\log g$	$v_{\rm mic}$/km s^{-1}	[Fe/H]	rv/km s^{-1}
500287810	4757943093811987072	05 28 29.6	-61 26 49.6	16.223	1.096	0.050	4550	0.95	2.40	-2.49	284
500382880	4762709889033585024	05 24 24.1	-59 16 05.5	16.456	1.001	0.032	4600	1.08	2.45	-2.65	268
497682788	4670107885871109760	04 03 47.0	-64 30 55.7	16.557	0.969	0.047	4550	1.10	2.60	-2.80	233
471915910	5481017880523468800	06 08 14.9	-62 07 23.5	16.600	0.948	0.049	4625	1.15	2.80	-2.90	266
500766372	4762322654782102272	04 59 15.4	-58 54 16.0	16.573	0.937	0.023	4650	1.17	2.75	-2.90	235
497519424	4664660389875115392	04 54 53.6	-64 07 52.2	16.616	1.001	0.036	4500	1.11	2.90	-3.13	290
499901368	4727018642084375936	03 02 07.9	-57 53 20.2	16.501	0.779	0.015	4750	1.23	1.80	-3.13	326

et al. 2015; Marino et al. 2019; Yong et al. 2021a) and a slightly more metal-rich sample in the LMC (Jönsson et al. 2020; Reggiani et al. 2021). For the Jönsson et al. (2020) sample, we applied the same cuts to the data as the ones for Oh et al. (2023) in terms of radius from LMC centre, parallax, proper motion and radial velocity. In this subsection, we will go through the abundance results in more detail. The abundance measurements of r-process elements will, however, be discussed in Section 6.5.3 as they constitute the key results of our paper.

Light Elements

The light elements measured in our study include carbon, nitrogen, oxygen, sodium and aluminium.

We have successfully measured carbon abundances for all of our stars, and examples are shown in Fig. 6.1. Since our stars are located on the upper part of the RGB (beyond the bump), they have therefore likely undergone first dredge-up. With evolutionary corrections from Placco et al. (2014), we can correct for this effect to recover estimates of their initial chemical composition. The typical correction value is $\sim +0.6$ dex. Our corrected carbon abundances have a mean and observed standard deviation of $\langle$[C/Fe]$\rangle = 0.16 \pm 0.33$ dex, and span a range of [C/Fe] $= -0.26$ to 0.63. Thus none of the sample meet the conventional definition of carbon-enhanced metal-poor stars ([C/Fe] > 0.7, Placco et al. 2014). Interestingly, the 2 stars with the highest (uncorrected and corrected) [C/Fe] values are also the ones with the lowest [Fe/H] in our sample. As regards to the other 5 stars in our sample, these have slightly lower [C/Fe] values compared to MW stars with similar metallicities; the difference is ~ 0.5 dex for the corrected abundances. Nevertheless, the values for these stars are similar to those of Jönsson et al. (2020) who find predominantly solar (corrected) [C/Fe] values in their LMC stars, which have metallicities down to [Fe/H] $= -2$. Our data extends this trend to [Fe/H] ≈ -3, as shown in the upper left and upper right panels of Fig. 6.4.

For nitrogen, due to the high levels of noise in the near-UV part of the spectra, we were only able to definitively measure nitrogen for one star, 497519424, as shown in Fig. 6.2, using the CN bands at 3883 Å. The upper limits for the other stars

range from [N/Fe] < 0.5 to < 1.1. Star 497519424 is strongly enhanced in nitrogen, [N/Fe] $= 1.7 \pm 0.11$, relative to MW stars at similar [Fe/H] values and to those for LMC at higher metallicities. From Placco et al. (2014), we can deduce that in such stars with much larger nitrogen abundances as compared to carbon, dredge-up causes [C/Fe] to become depleted as usual but [N/Fe] does not change much. Thus, we can confirm that this star has a high N abundance and a relatively low uncorrected C abundance ([C/Fe] $= 0.0$). This makes it a Nitrogen Enhanced Metal Poor (NEMP) star as defined in the literature ([N/Fe] > 0.5 and [C/N] < -0.5; Johnson et al. 2007). This is thus the first NEMP star to be identified in the LMC. Yong et al. (2021a) found a NEMP fraction of $55\% \pm 21\%$ for the stars in their sample in which [N/Fe] could be measured. Our fraction (one NEMP star from one [N/Fe] measurement) is consistent with that in Yong et al. (2021a) but clearly a larger sample of [N/Fe] measurements in LMC very and extremely metal-poor stars is required to better establish the consistency, especially as our non-detections have upper limits that are near or even above the discriminant limit for nitrogen enhancement at [N/Fe] $= 0.5$. Nevertheless, the existence of a least one NEMP star in the LMC, along with those in the MW, shows that whatever process is responsible for the generation of such stars, it is evidently not dependent on the environment.

For oxygen, the O I 6300 Å feature was partially or fully affected by telluric features in the spectra for 4 of the 7 stars in our sample. Hence, we were only able to measure oxygen abundances for the 3 remaining stars. The oxygen spectra for the most O abundant star (500382880) is shown in Fig. 6.3. We found that our average oxygen abundance value ($\langle$[O/Fe]$\rangle = 1.0 \pm 0.18$) for the 3 stars with [O/Fe] determinations is slightly higher than that for the MW ($\langle$[O/Fe]$\rangle = 0.69$; Cayrel et al. 2004) across roughly the same [Fe/H] range. On the other hand, our average [O/Fe] value for these 3 stars is apparently much larger than the LMC value at higher metallicities ($\langle$[O/Fe]$\rangle = 0.13$; Jönsson et al. 2020). We note, however, that significant systematic differences may exist between measurements from the O I line in this work and from the molecular near-infrared lines of OH in that work.

For sodium, the average abundance measurement for most of our stars ($\langle$[Na/Fe]$\rangle = 0.10 \pm 0.11$) is generally similar to those for the MW halo and the LMC at higher metallicities, and, with the exception of one star (the NEMP star 497519424 that has an exceptionally high [Na/Fe] value), there is no evidence for an intrinsic [Na/Fe] scatter for these stars. We note that the enhancement in [Na/Fe] in the NEMP star 497519424 exceeds that in any of the stars in Yong et al. (2021a) or Reggiani et al. (2021). This star will be further discussed in Section 6.5.4.

For aluminium, our average abundance results ($\langle$[Al/Fe]$\rangle = -0.27 \pm 0.20$) are generally higher than that of the MW halo, but similar to the LMC at higher metallicities. Given the size of the error bars for [Al/Fe], there does not seem to be any intrinsic scatter in our aluminium measurements.

α Elements

The elements magnesium, silicon, calcium and titanium are commonly denoted as α elements. This refers to elements that are primarily produced through nuclear fusion reactions involving successive α-particle captures, such as stellar nucleosynthesis in core collapse supernovae. Our analysis shows that the measured abundances of the α elements are generally consistent with the observed α abundances in metal-poor stars within the Milky Way and in the LMC.

For magnesium, there is good agreement with the MW halo for 6 out of 7 stars in terms of our average abundance measurements ($\langle$[Mg/Fe]$\rangle = 0.33 \pm 0.08$). These stars extend to lower [Fe/H], the [Mg/Fe] vs [Fe/H] relation for the LMC seen in the results from Reggiani et al. (2021) and Jönsson et al. (2020). One star, 500766372, appears Mg depleted with a low value of [Mg/Fe] $= -0.02 \pm 0.09$, which is 0.3 dex below the average of the other stars in our sample.

For silicon, our average abundance and scatter ($\langle$[Si/Fe]$\rangle = 0.47 \pm 0.31$) are similar to that of the MW halo. The star-to-star scatter is significantly larger than the typical error bar, implying that the abundance dispersion is real. In addition, the average measurement of our 4 most silicon abundant stars ($\langle$[Si/Fe]$\rangle = 0.68 \pm 0.25$) are consistent with the high [Si/Fe] seen in the Reggiani et al. (2021) sample, while the average measurement for the other 3 ($\langle$[Si/Fe]$\rangle = 0.20 \pm 0.08$) are more consistent with the lower [Si/Fe] values seen in the Jönsson et al. (2020) sample at higher [Fe/H]. Interestingly, the silicon abundances from Reggiani et al. (2021), like our results, have a large scatter, while the results from Jönsson et al. (2020) have a small scatter, even in the region where they overlap in metallicity. This could be due to the fact that, like us, Reggiani et al. (2021) used optical spectra, as opposed to the near-infrared H-band data of Jönsson et al. (2020).

For calcium, our average abundance ($\langle$[Ca/Fe]$\rangle = 0.25 \pm 0.09$) shows excellent agreement with the MW halo and with most of the LMC stars from Reggiani et al. (2021) and Jönsson et al. (2020). However, unlike the case for the other LMC samples, we do not see any evidence for a large scatter in [Ca/Fe] similar to that exhibited at higher [Fe/H] values. Specifically, in our sample there are no stars with very high [Ca/Fe] values comparable to those seen in the Reggiani et al. (2021) results. Additionally, at our [Fe/H] values, we see no stars with sub-solar [Ca/Fe] comparable to

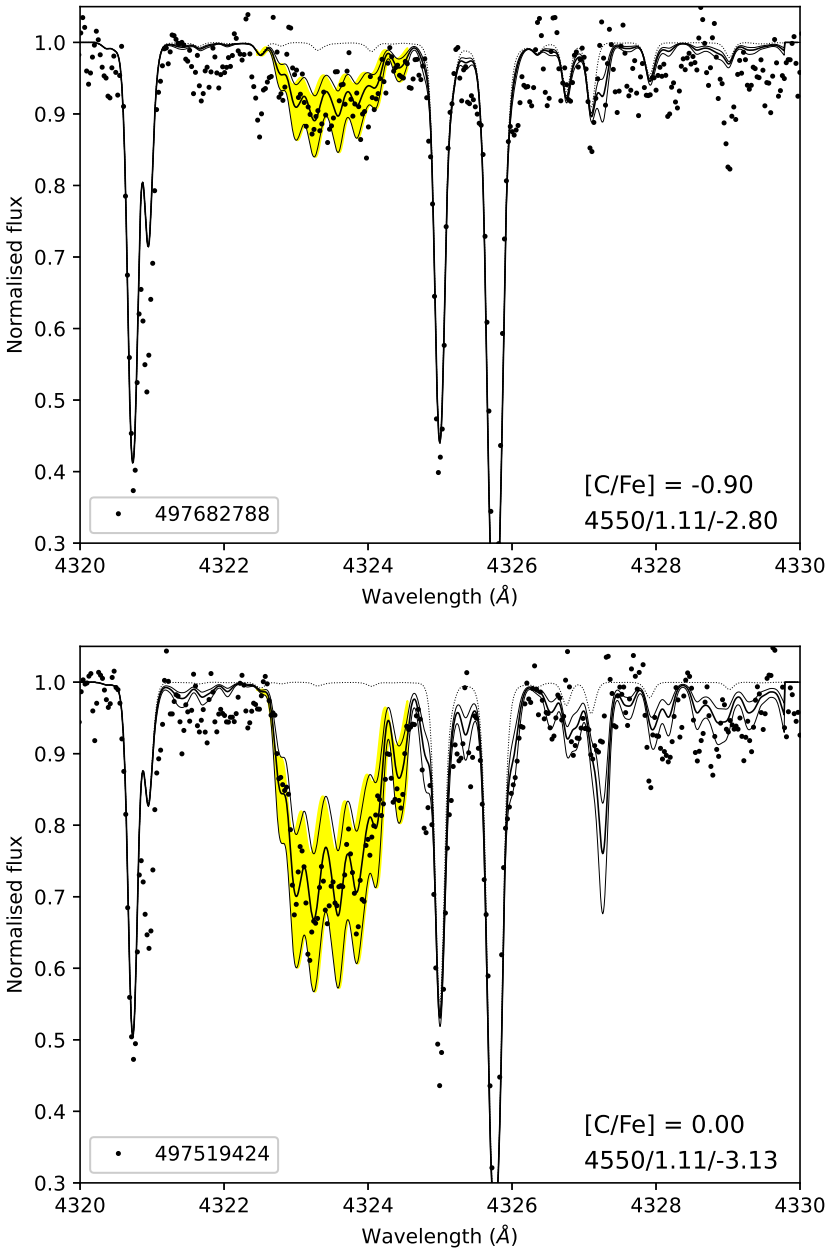

Figure 6.1: Comparison of observations (black dots) and synthetic spectra in the vicinity of the CH G-band at 4323 Å for our least carbon abundant star (top: 497682788) and most carbon abundant star (bottom: 497519424). The synthetic spectra depicted by thin dotted lines correspond to [C/Fe] = −9. The best-fitting synthetic spectra are illustrated by a thick black line, while the yellow shaded regions indicate a range of ±0.2 dex around the best fit. The abundances have not been adjusted for evolutionary effects. The stellar parameters $T_{\rm eff}$/ log g/ [Fe/H] are shown.

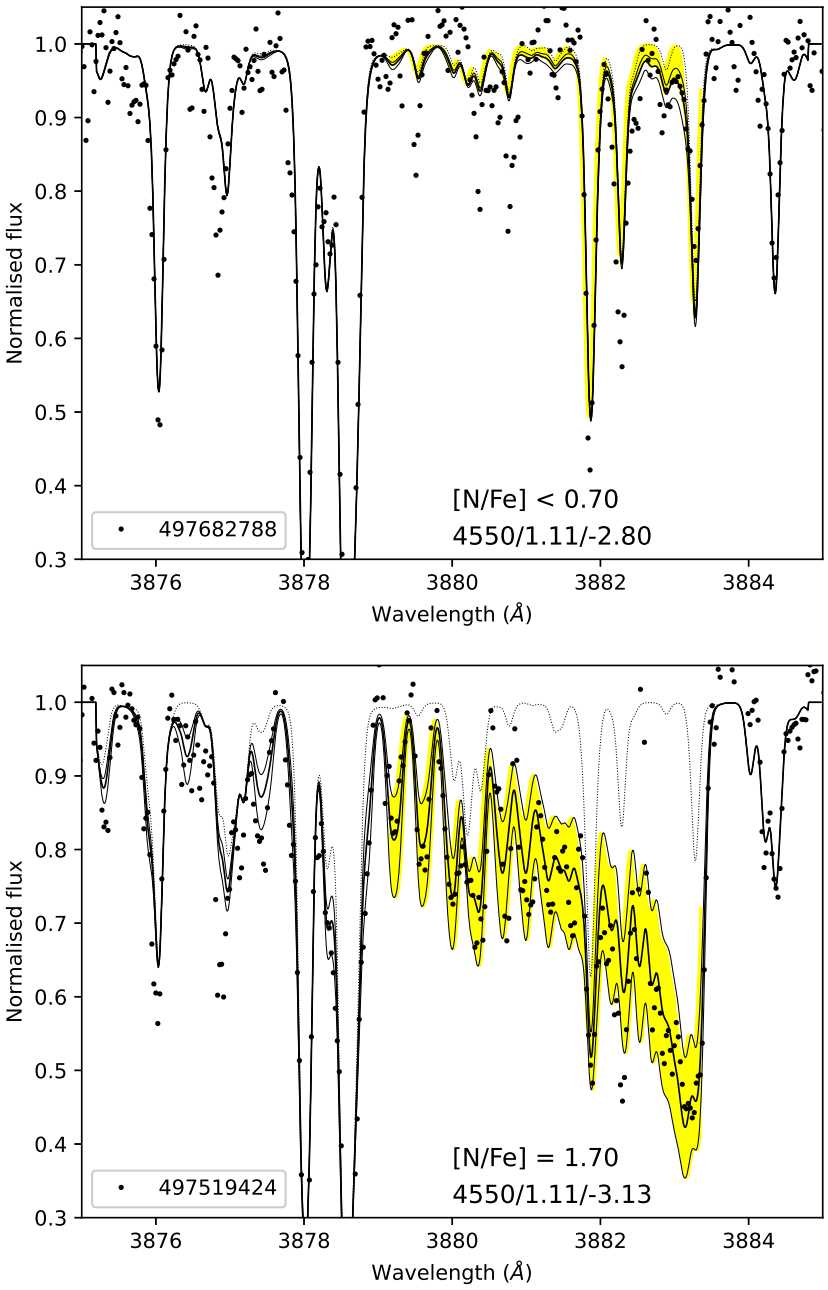

Figure 6.2: Same as Figure 6.1 but for [N/Fe] illustrating the CN 3883 Å feature.

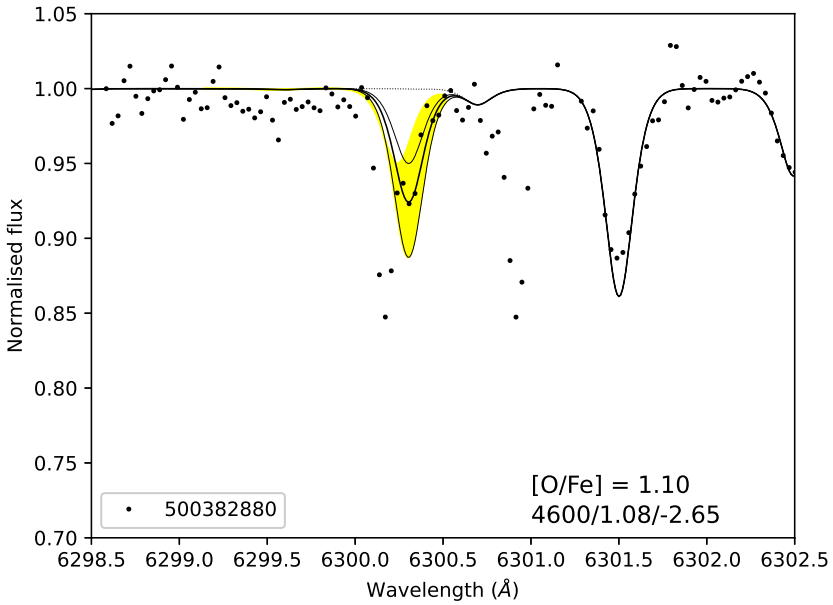

Figure 6.3: Same as Figure 6.1 but for [O/Fe] illustrating the forbidden red line of neutral oxygen ([O I] 6300 Å).

the results of Jönsson et al. (2020) at metallicities exceeding [Fe/H] = −2.0.

For titanium, our abundance results ($\langle$[TiI/Fe]$\rangle = 0.20 \pm 0.11$; $\langle$[TiII/Fe]$\rangle = 0.33 \pm 0.14$) are similar to those for calcium, with good agreement with the MW halo and reasonable agreement with the LMC samples. There is no evidence for any intrinsic scatter in our [Ti I/Fe] and [Ti II/Fe] values, and there are no stars in our sample with [Ti I/Fe] values comparable to the very high [Ti I/Fe] measurement seen in one star in the Reggiani et al. (2021) sample.

Based on the [Mg/Fe] plot in Fig. 6.4, our results seem to provide a low-metallicity anchor to the α-knee[1], which is caused by the occurrence of SNIa that produce large amounts of iron-peak elements relative to α-elements, as compared to core-collapse supernovae. In a similar approach to Reggiani et al. (2021), we used the SEGMENTED package in Python (Muggeo 2003; Pilgrim 2021) to quantitatively determine the α-knee in the LMC. This involved fitting a segmented piece-wise linear model to the [Fe/H]–[Mg/Fe] plot as shown in Fig. 6.9. Our result indicates that the α-knee location is found at around [Fe/H] = -2.3 ± 0.4, and it is not inconsistent with that of Nidever et al. (2020), which used the APOGEE data from Jönsson et al. (2020) to conclude that the α-knee is constrained to about [Fe/H] ≤ -2.2. However, we note that our α-knee determination has a large degree of uncertainty (0.4 dex), and other α-elements, such as calcium and titanium, do not show a clear α-knee. Thus,

[1]The α-knee is defined by the value of [Fe/H] where the [Mg/Fe] or [α/Fe] values starts to decrease from a near constant value at lower [Fe/H].

more abundance measurements across the potential α-knee location are needed to improve the precision of the determination.

Iron-peak Elements

The iron-peak elements include scandium, chromium, manganese, cobalt, nickel and zinc. Since the metallicities of our sample are likely located above the [α/Fe] knee, the SNIa contribution to the iron-peak abundance ratios is very limited. Thus, the main contributor to the synthesis of these elements are core collapse (type II) supernovae.

For scandium, our results agree with that of Jönsson et al. (2020) at higher [Fe/H], but are slightly lower than that of the MW halo. One star, 500766372, has an unusually low [Sc/Fe] value ($[\mathrm{Sc/Fe}] = -0.30 \pm 0.13$). It also has high zinc, and very low strontium and barium abundances, and will be discussed further in Section 6.5.4. After excluding the discrepant star, the average and scatter of the scandium abundances become $\langle[\mathrm{Sc/Fe}]\rangle = 0.08 \pm 0.21$. There is little evidence to suggest that there is an intrinsic spread in [Sc/Fe] relative to the uncertainty of our measurements.

For cobalt and manganese, as our Milky Way comparison sample, we used results from Jacobson et al. (2015) and Marino et al. (2019) instead of Yong et al. (2021a). This is due to the fact that the [Co/Fe] and [Mn/Fe] results from Yong et al. (2021a) appear inconsistent with other datasets, for reasons that are not entirely clear, but which may be related to the implementation of hyperfine structure corrections. No other element ratios are affected.

In general, our iron-peak abundance measurements are consistent with those of the Milky Way halo. The typical measurement error and intrinsic spread in the abundance ratios relative to iron are on the order of 0.1–0.2 dex, which is also mostly consistent with the LMC determinations at higher [Fe/H]. One exception however, is zinc, with one star (500766372) having a high zinc abundance ($[\mathrm{Zn/Fe}] = 0.75 \pm 0.04$) compared to the rest, similar to the highest MW values. For the other stars, 4 have $\langle[\mathrm{Zn/Fe}]\rangle \sim 0.40$ while the remaining two most metal-rich stars have solar [Zn/Fe] comparable to the lowest [Zn/Fe] ratios in the MW halo. The other exception is scandium, where the star with high [Zn/Fe] also has an unusually low [Sc/Fe] value. In addition, the average abundances of Cr and Co are 0.1 dex higher than the MW average, but a little lower than Reggiani's typical abundances and in particular exhibit less scatter.

Sr, Y, Zr and Ba

At solar metallicities, heavy elements such as strontium, yttrium, zirconium and barium are produced by the slow neutron capture process (s-process) that occurs in asymptotic giant branch (AGB) stars, which are low to intermediate-mass stars in the late stages of their evolution (e.g. Karakas & Lattanzio 2007; Kobayashi et al. 2020b). However, at low metallicities such as the ones found in our stars, it is not clear that there has been enough time to allow low to intermediate-mass AGB stars to evolve and distribute these elements into the LMC interstellar medium.

For strontium, our average abundance and standard deviation ($\langle$[Sr/Fe]$\rangle = 0.25 \pm 0.43$) are consistent with the MW halo, particularly in the existence of a large observed range of over 1 dex seen in the [Sr/Fe] measurements.

For yttrium, our average abundance and standard deviation ($\langle$[Y/Fe]$\rangle = -0.24 \pm 0.26$) are also consistent with MW halo and with the stars from Reggiani et al. (2021) that have higher [Fe/H]. There is, however, one star (500766372) in our sample with a very low abundance value ([Y/Fe] ≤ -1.0), as shown by the upper limit in the plot shown in Fig. 6.7. It is important to point out however, that the measurements in our comparison MW sample are lacking due to limited S/N and wavelength coverage in Yong et al. (2021a). The true range of abundances in the MW may therefore be underestimated for yttrium.

For zirconium, similar to the previous two elements, our average abundance and standard deviation ($\langle$[Zr/Fe]$\rangle = 0.04 \pm 0.27$) are consistent with the MW halo. There are also two stars (500287810 & 500766372) with evidently low zirconium abundances ([Zr/Fe] $= -0.39 \pm 0.07$; [Zr/Fe] $= -0.33 \pm 0.08$) as shown in the plot. This again may reflect selection effects in the MW comparison sample, which may suffer from restrictions in S/N and wavelength coverage (Yong et al. 2021a).

For barium, our average abundance and standard deviation ($\langle$[Ba/Fe]$\rangle = -0.54 \pm 0.47$) are again consistent with the MW halo, and they cover a large range in [Ba/Fe] (exceeding 1 dex) as seen in Figure 6.7. While Reggiani et al. (2021) found a fairly flat variation with metallicity, our barium abundances decline toward the lowest metallicities, in good agreement with the MW.

In Figure 6.10, we consider the [Sr/Ba] vs [Ba/H] ratios. Yong et al. (2013) found that at [Ba/H] < -2.5, the intrinsic spead in [Sr/Ba] increases as [Ba/H] decreases. In contrast, our results do not exhibit an increase in intrinsic spread towards lower [Ba/H] values. Instead, the [Sr/Ba] ratios in our sample show a uniformly smaller

spread than the halo at similar [Ba/H]. The low [Ba/H] and [Sr/H] values nevertheless indicate that there has not been sufficient time for AGB enrichment to have affected our stars. Furthermore, the lack of high [Sr/Ba] values also suggests that any contribution from spinstars, which are thought to be a possible source of s-process enrichment at low metallicities (Cescutti & Chiappini 2014), is not significant. Further details on this topic will be discussed in Section 6.5.4.

In general, the star-to-star scatter is larger than the measurement error for all four of these elements. This implies that the production is decoupled from that of the iron-peak, either because a second site is responsible for this production, or that the production depends on an parameter such as rotation (e.g. Frischknecht et al. 2016).

Abundance summary

Figure 6.11 summarises the abundance results for our LMC stars into a single plot. The MW halo results from the literature (Cayrel et al. 2004; Jacobson et al. 2015; Marino et al. 2019; Yong et al. 2021a), which are averaged for $-3.13 \leq$ [Fe/H] ≤ -2.49, are also shown for comparison. The red stars represent abundance measurements that differ by more than 0.5 dex relative to the mean MW values (black dots and lines). Overall, our LMC results are consistent with that of the MW halo for most of the elements measured. We note however, that each star is strongly discrepant, by at least 0.5 dex compared to the MW, in at least one element.

6.5.3 r-process elements

As shown in the [Eu/Fe] plot in Fig. 6.8 and in the spectra in Fig. 6.12, two of our stars are r-process enhanced. Using the customary classifications for r-process enhanced stars ([Eu/Fe] > 1.0 and [Ba/Eu] < 0.0; Barklem et al. 2005), 497682788 is an r-II star. The other one is 500382880, an r-I star ($0.3 <$ [Eu/Fe] < 1.0 and [Ba/Eu] < 0.0). Since the constraint for pure r-process production of Ba and Eu is thought to be [Ba/Eu] $= -0.78 \pm 0.06$ (Mashonkina & Christlieb 2014), our stars' relatively low abundance ratios ($\langle$[Ba/Eu]$\rangle \approx -0.9$) most likely indicates a pure r-process enrichment. For the other 5 stars, only upper limits could be measured for the [Eu/Fe] ratios. Their values clearly show that they are not significantly r-process enhanced. This result is confirmed by comparing the abundance ratios for the other r-process elements (La, Nd, Sm, Dy) in Fig. 6.11; they all paint the same picture in showing that 2 out of the 7 stars are r-process enhanced, and the other 5 are not.

Table 6.2: Abundance results, showing the sample size, mean, standard deviation and average measurement uncertainty of our various abundance measurements, for stars where a given element was detected. Average abundances gathered for the Milky Way from the literature for $-3.13 \leq$ [Fe/H] ≤ -2.49 (Cayrel et al. 2004; Jacobson et al. 2015; Marino et al. 2019; Yong et al. 2021a) have been included for comparison.

Element	N	μ	$\sigma_{\mathrm{dispersion}}$	σ_{err}	$\mathrm{N_{MW}}$	μ_{MW}	σ_{MW}
[C/Fe]	7	0.16	0.33	0.20	57	0.33	0.3
[N/Fe]	1	1.70	0.00	0.11	13	0.53	0.74
[O/Fe]	3	1.00	0.13	0.18	14	0.69	0.17
[Na/Fe]	7	0.27	0.45	0.11	63	0.28	0.31
[Mg/Fe]	7	0.28	0.15	0.06	67	0.27	0.14
[Al/Fe]	7	−0.27	0.20	0.17	44	−0.68	0.21
[Si/Fe]	7	0.47	0.31	0.13	26	0.53	0.16
[Ca/Fe]	7	0.25	0.09	0.06	69	0.28	0.11
[Sc/Fe]	7	0.14	0.20	0.17	37	0.36	0.20
[TiI/Fe]	7	0.20	0.11	0.06	66	0.26	0.16
[TiII/Fe]	7	0.33	0.14	0.17	69	0.30	0.16
[Cr/Fe]	7	−0.24	0.07	0.07	69	−0.35	0.15
[Mn/Fe]	7	−0.39	0.26	0.20	70	−0.40	0.18
[FeI/H]	7	−2.86	0.24	0.09	69	−2.89	0.17
[FeII/H]	7	−2.83	0.20	0.09	68	−2.86	0.18
[Co/Fe]	7	0.25	0.08	0.09	71	0.14	0.26
[Ni/Fe]	7	−0.09	0.11	0.16	68	−0.04	0.16
[Zn/Fe]	7	0.33	0.24	0.06	21	0.20	0.18
[Sr/Fe]	7	−0.57	0.43	0.17	68	−0.43	0.60
[Y/Fe]	6	−0.24	0.26	0.19	14	−0.37	0.21
[Zr/Fe]	7	0.04	0.27	0.07	15	0.12	0.17
[Ba/Fe]	7	−0.54	0.47	0.17	67	−0.62	0.50
[La/Fe]	2	0.39	0.16	0.07	0	-	-
[Nd/Fe]	2	0.58	0.21	0.07	0	-	-
[Sm/Fe]	2	0.70	0.14	0.09	0	-	-
[Eu/Fe]	2	0.91	0.16	0.07	15	0.31	0.41
[Dy/Fe]	2	0.93	0.11	0.08	0	-	-

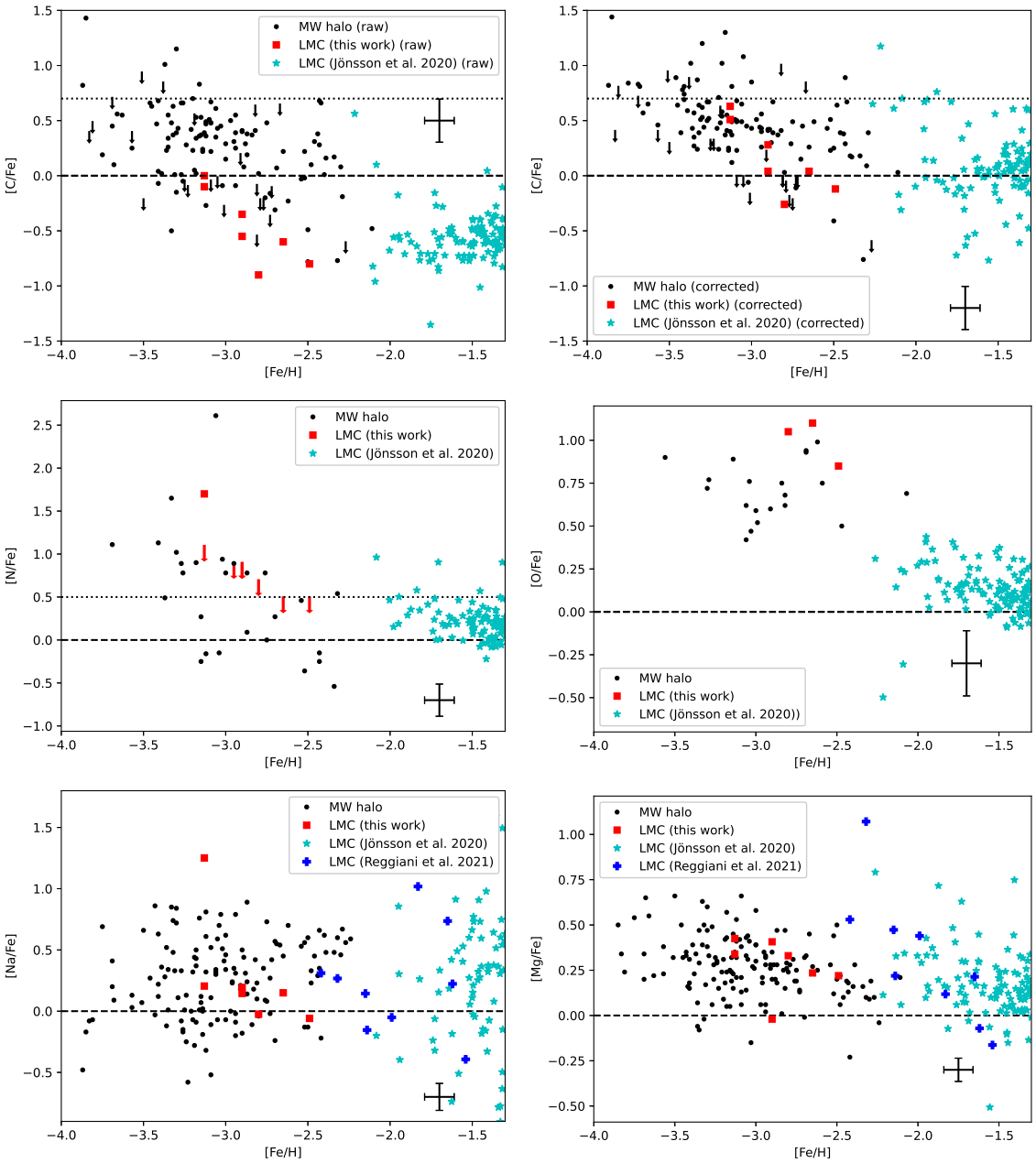

Figure 6.4: [X/Fe] vs [Fe/H] for elements C–Mg, for our Magellanic metal-poor sample (red triangles) compared to a Milky Way halo sample (black dots) from Yong et al. (2021a), LMC giants from Reggiani et al. (2021) (blue plus signs) and Jönsson et al. (2020) (cyan stars). A representative error bar for our data is provided in the bottom right corner. Upper limits to abundances are indicated by arrows. For [C/Fe], both the observed and corrected abundances are shown. For [O/Fe], 4 out of 7 stars were affected by telluric contamination that did not allow estimating an abundance or a meaningful limit. The dotted lines in the [C/Fe] and [N/Fe] plots indicate the lower limits of the CEMP ([C/Fe] > 0.7) and NEMP ([N/Fe] > 0.5) stars respectively.

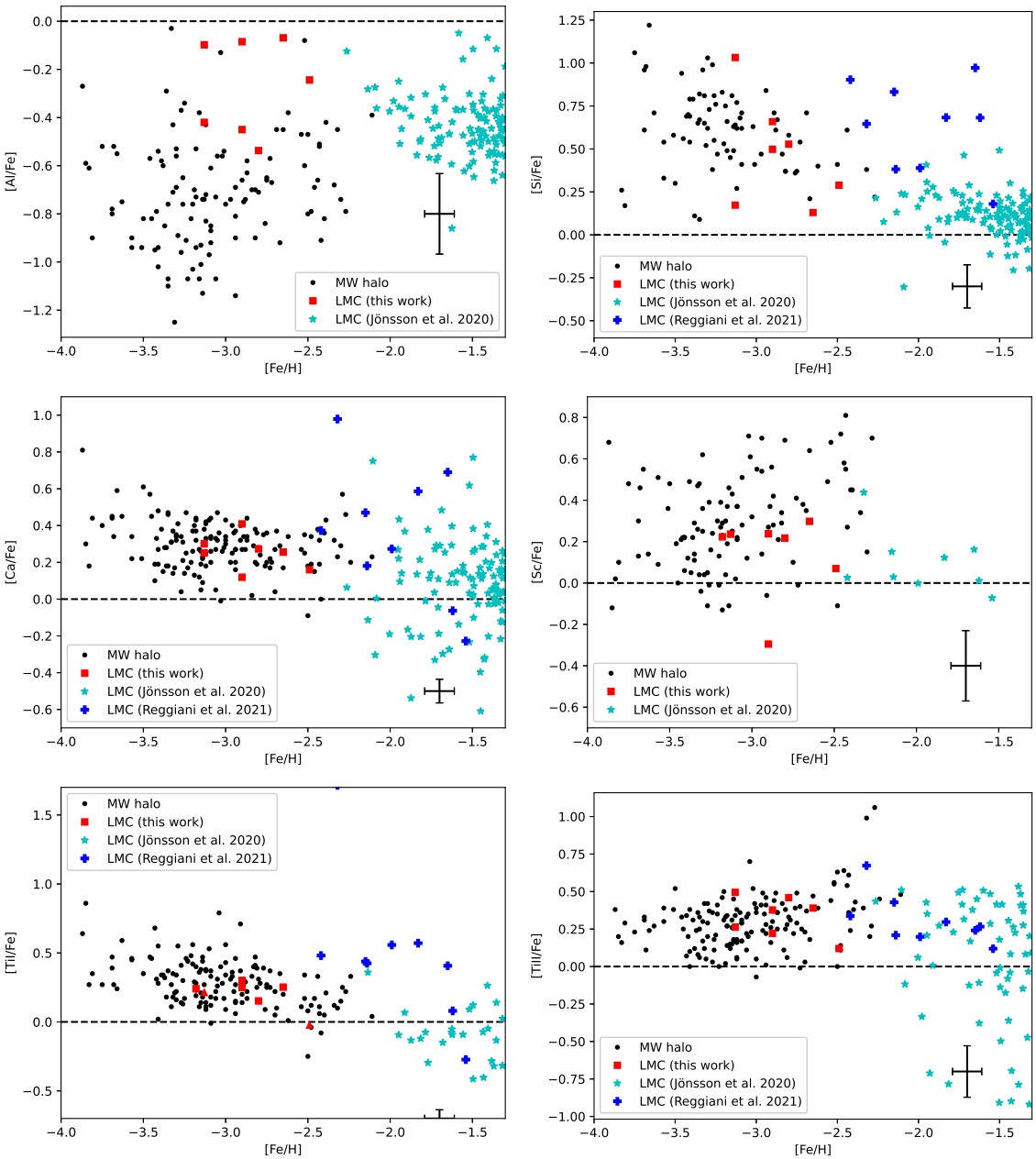

Figure 6.5: Same as Fig. 6.4 but for elements Al–Ti.

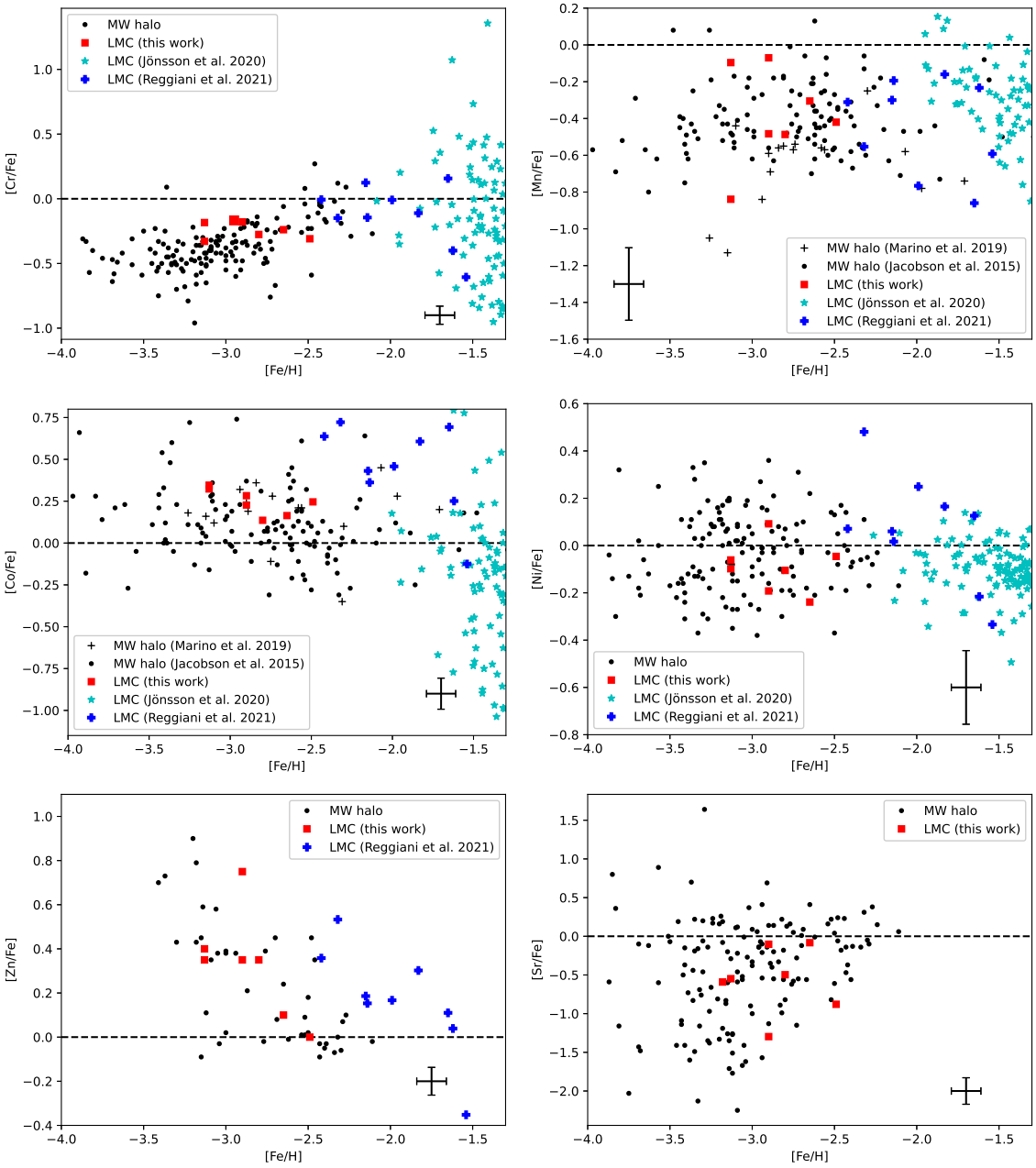

Figure 6.6: Same as Fig. 6.4 but for elements Cr–Sr. For Mn and Co, results from Jacobson et al. (2015) and Marino et al. (2019) were used instead of Yong et al. (2021a) as mentioned in Section 6.5.2.

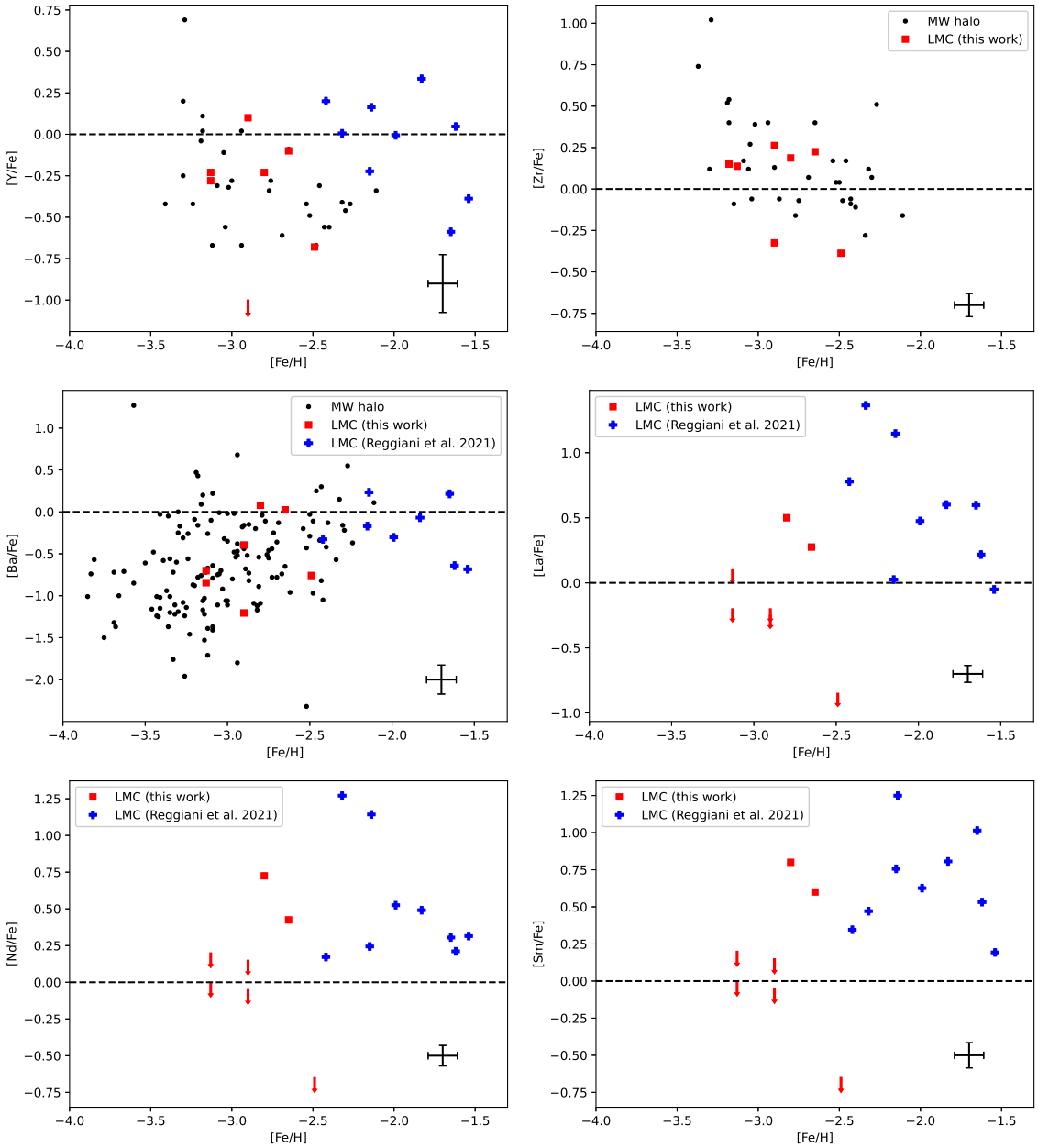

Figure 6.7: Same as Fig. 6.4 but for elements Y–Sm.

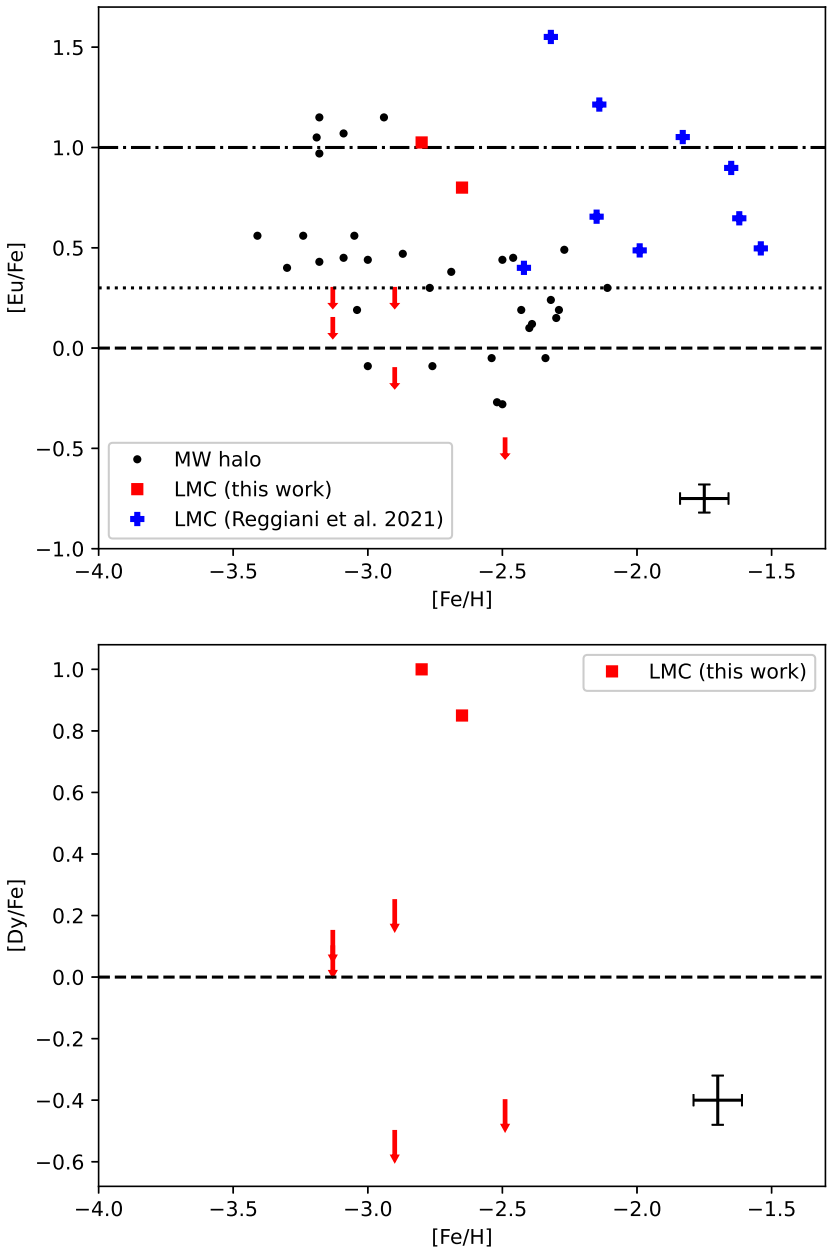

Figure 6.8: Same as Fig. 6.4 but for Eu and Dy. For the Eu plot, the dotted and dash-dot lines represent the lower limit for r-I ([Eu/Fe] $>$ 0.3) and r-II ([Eu/Fe] $>$ 1.0) stars respectively.

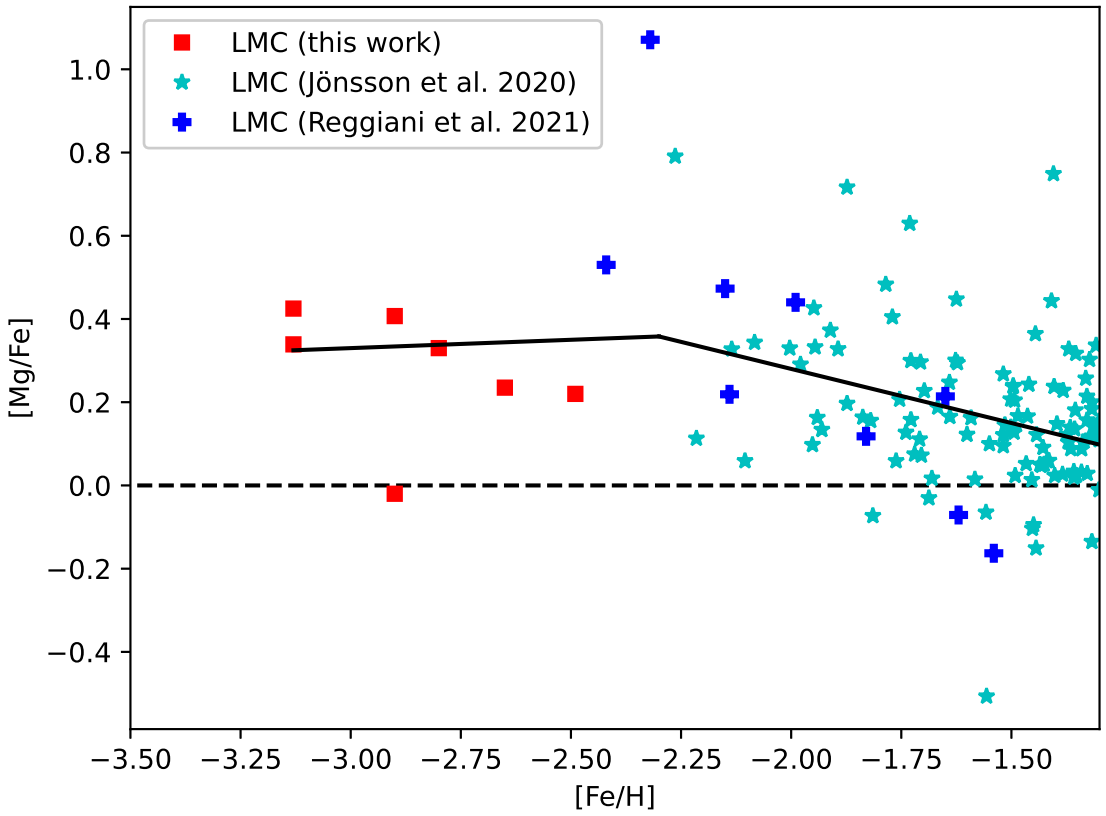

Figure 6.9: [Mg/Fe] for LMC stars together with data from Reggiani et al. (2021) and Jönsson et al. (2020). A piecewise linear fit is overlaid, indicating an α-knee at [Fe/H] $= -2.3 \pm 0.4$.

We also compare the r-I and r-II star occurrences in the LMC and the Milky Way halo. For our sample, the results reveal that the occurrence rates of these stars are statistically indistinguishable in the two environments. Specifically, the LMC sample exhibited occurrence rates of 1/7 (14^{+16}_{-9}%) for r-I stars, 1/7 (14^{+16}_{-9}%) for r-II stars and 2/7 (29^{+17}_{-14}%) for both r-I and r-II stars, while the Milky Way halo sample (Yong et al. 2021a) exhibited occurrence rates of 16/150 (11^{+3}_{-2}%) for r-I stars, 4/150 (3^{+2}_{-1}%) for r-II stars and 20/150 (13^{+3}_{-3}%) for both r-I and r-II stars. The statistical likelihood analysis was performed following the approach of Reggiani et al. (2021). However, if we factor in the 4 very metal-poor stars from Reggiani et al. (2021), the occurrence rates for all the very and extremely metal-poor stars in the combined LMC sample (i.e., stars with $-3.13 \leq$ [Fe/H] ≤ -2.14) increases to 3/11 (27^{+14}_{-11}%) for r-I stars, 3/11 (27^{+14}_{-11}%) for r-II stars and 6/11 (55^{+13}_{-14}%) for both r-I and r-II stars. Our findings indicate that the r-II fraction deviates by more than 2 sigma from the Milky Way value, considering a similar [Fe/H] range as the sample in Yong et al. (2013). To confirm or disprove the potential surplus of r-II stars relative to the Milky Way, a more extensive collection of LMC stars with [Eu/Fe] measurements at [Fe/H] < -2 is essential. These findings provide valuable insights into the similarities and potential differences of stellar populations in the LMC and the Milky Way halo, which becomes more clear at the lowest metallicities.

For the 2 stars in our sample that are r-process enhanced, their r-process element abundance ratios relative to iron are consistent with those of Reggiani et al. (2021) as shown in Fig. 6.13. In addition, their abundances also seem to follow the solar r-process pattern (e.g. Simmerer et al. 2004), as shown in Fig. 6.14. Our result is consistent with that of the literature, where there is a good agreement with scaled solar r-process abundances for heavier elements ($Z \geq 56$) in other r-process rich stars (Ernandes et al. 2023). We also note that just like in the literature, our values do not agree as well with the solar abundance ratios for the lighter neutron-capture elements Sr and Y.

The heavy element abundances reported by Reggiani et al. (2021) exhibit a significant degree of scatter among their sample. While most of this can be attributed to the varying levels of r-process enhancement, it is worth noting that even after normalising by [Eu/Fe] or the average [X/Fe] values for heavy elements, a substantial scatter still remains. To better visualise the comparison, we opted to calculate a straight average of their abundances for each element without any renormalisation.

For our two r-process enhanced stars, the [X/Fe] abundances agree well with the average abundances from Reggiani et al. (2021) as shown in Fig. 6.13, indicating

consistency in the r-process for all these r-process enhanced stars. In addition, their abundances of the two r-process enhanced stars also seem to follow the solar r-process pattern (e.g. Simmerer et al. 2004), as shown in Fig. 6.14. Our result is consistent with that of the literature, where there is a good agreement with scaled solar r-process abundances for heavier elements ($Z \geq 56$) in other r-process rich stars (Ernandes et al. 2023). We also note that just like in the literature, our values do not agree as well with the solar abundance ratios for the lighter neutron-capture elements Sr and Y.

Implication of the r-process abundances

The detection of low levels of barium ([Ba/Fe] ~ -0.8) and strontium ([Sr/Fe] ~ -0.7) in our two most metal-poor stars suggests the presence of some base level of r-process enrichment at the lowest metallicities, most likely originating from some form of core-collapse supernovae (e.g. Ji et al. 2019).

Additionally, the lack of r-process enhancements in those stars may indicate a longer timescale for the site of the r-process nucleosynthesis. There are a number of possible r-process sites, including magneto-rotational supernovae, but the major source is likely to be binary neutron star mergers, although this topic continues to be debated within the community (Kobayashi et al. 2023). Binary neutron star mergers are known to occur on extended timescales, ranging from $\sim$ 30 Myr to several Gyr (Belczynski et al. 2018; Neijssel et al. 2019), while magneto-rotational supernovae are related directly to massive star evolutionary timescales, on the order of 10–20 Myr (Ji et al. 2019). Therefore, based on the absence of r-process enhancements in the most metal-poor stars ([Fe/H] < -2.8) in our sample, it is plausible that magneto-rotational supernovae might have made only a minor contribution in the LMC.

Furthermore, chemical evolution models have noted that the MW reached [Fe/H] ~ -3.5 after about 60 Myr (Kobayashi et al. 2020b). Nidever et al. (2020) found in their model for the Large Magellanic Cloud (LMC) that chemical evolution had advanced no further than [Fe/H] < -2.2 after about 100 Myr. Thus, based on the [Fe/H] $= -2.8$ cutoff for r-process enrichment in our results, and taking into account the chemical evolution models, we postulate a minimum timescale of $\sim$ 100 Myr for the neutron star binary merger process to generate substantial r-process enhancements in the LMC. This finding is in line with the conclusions drawn by Reggiani et al. (2021), whose study focused on stars that are comparatively more metal-rich than those in our sample, and who found that all the stars in their sample exhibited r-process enhancement.

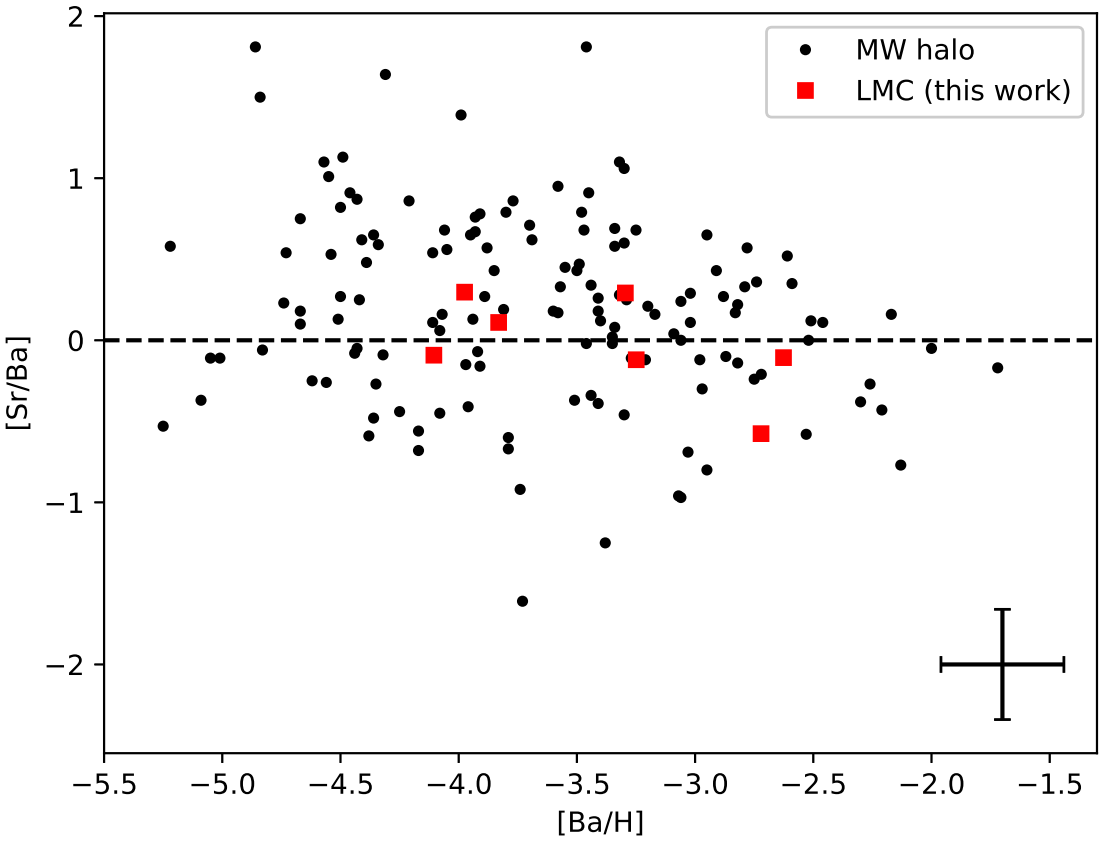

Figure 6.10: [Sr/Ba] vs [Ba/H] ratios for all 7 stars in our sample. The Milky Way halo results from Yong et al. (2021a) have been included for comparison.

Interestingly, the findings from Ji et al. (2016) regarding the UFD Reticulum II (Ret II) are also consistent with our results. Just like our sample, the two most metal-poor stars in Ret II with [Fe/H] < -3 are not r-process enhanced in the way the more metal-rich Ret II stars are (Ji et al. 2016). While we cannot rule out the presence of inhomogeneous metal mixing in such environments, it is plausible that both the LMC and Ret II contain stars at low [Fe/H] that formed before major r-process enrichment events, indicating that significant r-process enrichment did not occur until after a degree of enrichment in the α and iron-peak elements.

However, the study of Skúladóttir et al. (2019) shows continuous r-process enrichment in the Sculptor dwarf galaxy, indicating chemical evolution without a significant time delay relative to core-collapse supernovae. This disparity with our findings highlights the complexity in terms of comprehending r-process enrichment timescales. Additional europium abundance measurements for dwarf galaxies at lower metallicities could prove instrumental in addressing this issue.

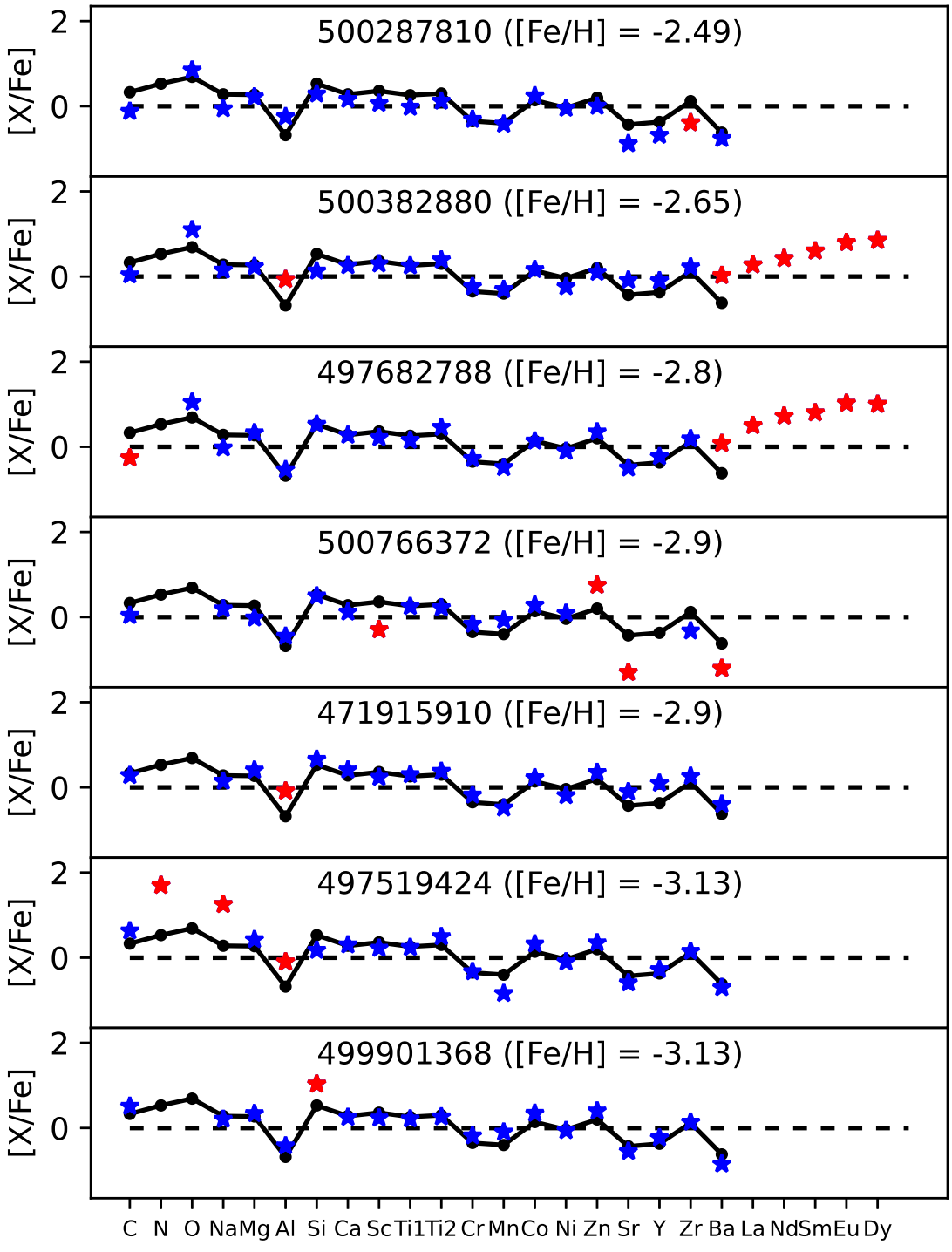

Figure 6.11: Overview of the abundance measurements for individual stars (500287810, 500382880, 497682788, 500766372, 471915910, 497519424, 499901368) with literature values. The stars represent our abundance measurements, and the black dots represent the mean MW values from the literature (Cayrel et al. 2004; Jacobson et al. 2015; Marino et al. 2019; Yong et al. 2021a). The star colours indicate if the abundance is within 0.5 dex of the MW average (blue) or not (red).

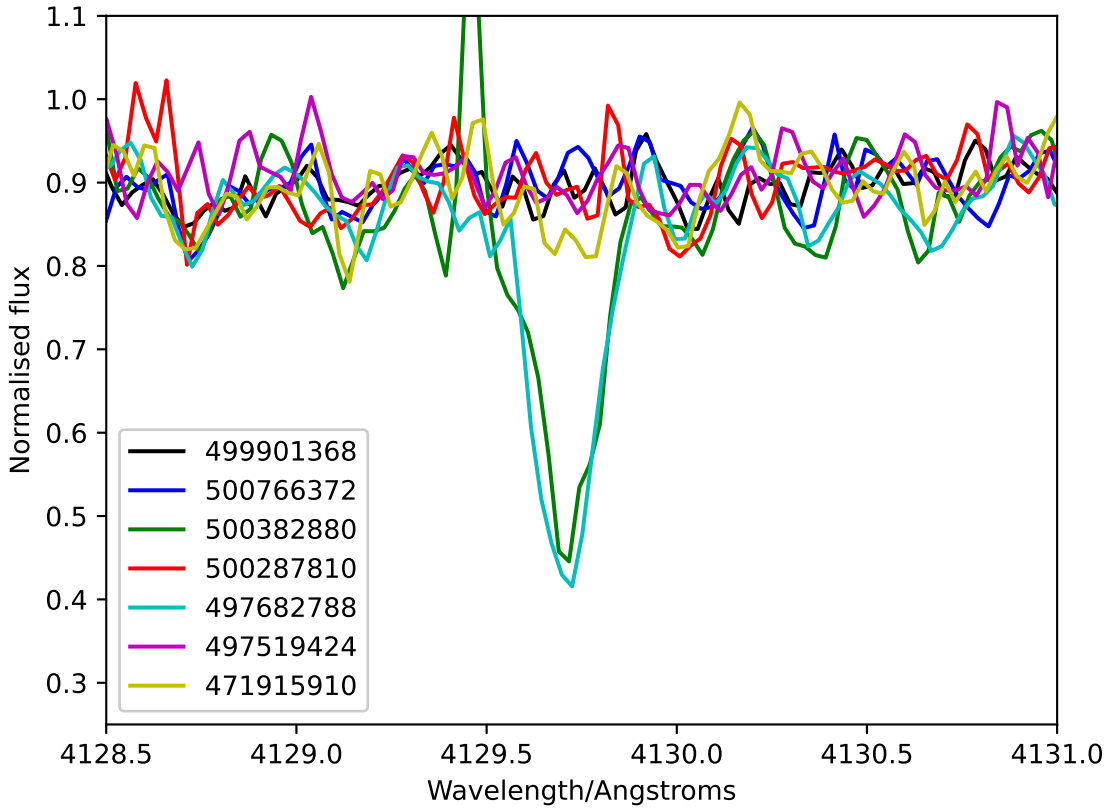

Figure 6.12: The Eu II line at 4129 Å for all 7 stars in our sample. While the line cannot be detected in 5 out of 7 stars, the two stars 497682788 and 500382880 are clearly over-abundant. For these stars, we estimate their Eu abundances to be [Eu/Fe] $= 1.03 \pm 0.06$ and [Eu/Fe] $= 0.80 \pm 0.08$ respectively.

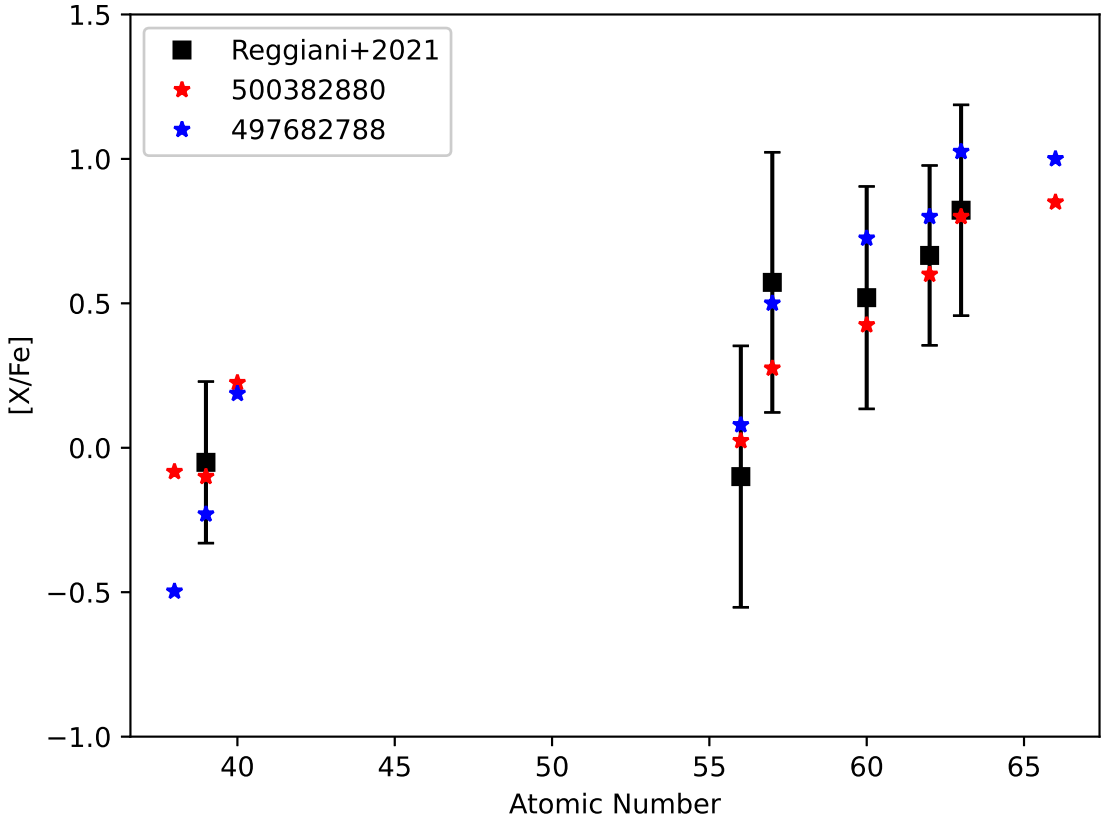

Figure 6.13: [X/Fe] ratios of heavy elements Sr–Dy for our 2 r-process enhanced stars, compared to the mean and scatter of the sample from Reggiani et al. (2021). No rescaling has been applied to the abundances.

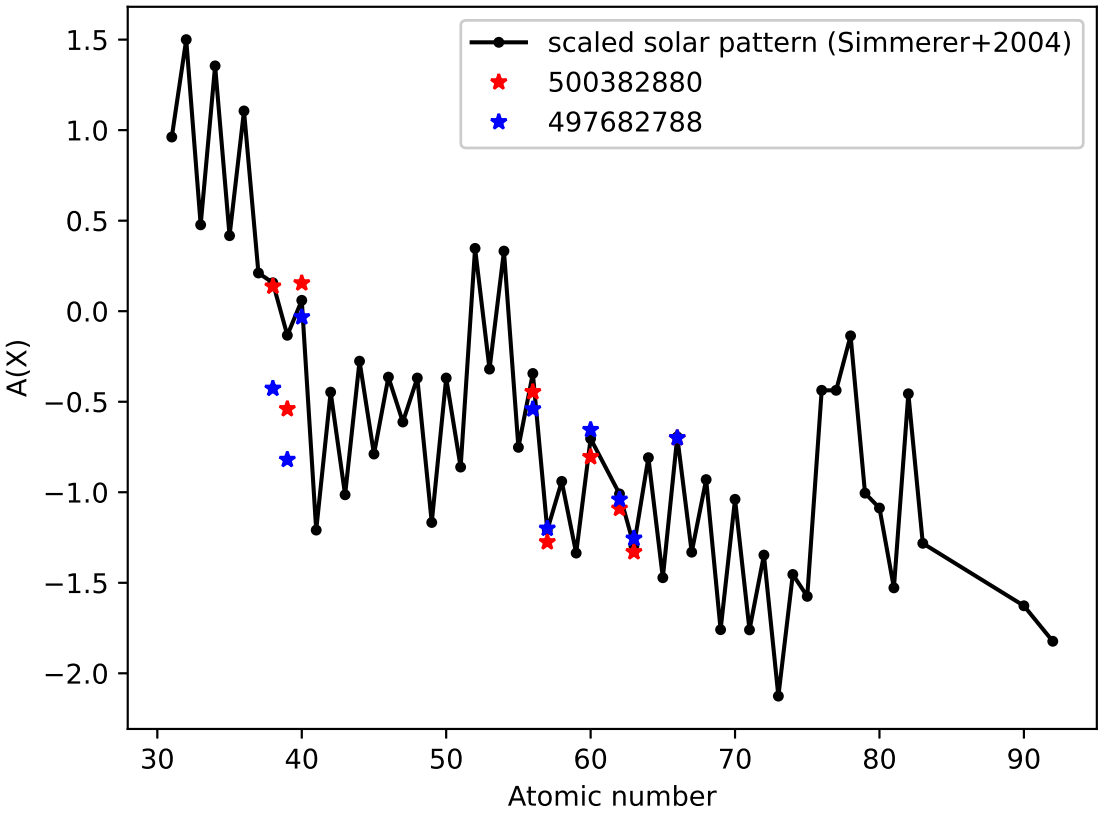

Figure 6.14: Heavy element abundances of Sr–Dy for our 2 r-process enhanced stars (500382880 & 497682788), compared with the scaled solar r-process pattern from Simmerer et al. (2004). The solar pattern has been normalised to the mean of the two A(Eu) values. Our abundances agree well with the solar scaled pattern for heavy elements $Z = 56$–66 as well as $Z = 40$, but less so for the light elements $Z = 38$–39

6.5.4 Individual stars

497519424: NEMP

In Section 6.5.2, we demonstrated that 49751942 is a NEMP star, with elevated levels of sodium and aluminum. Building upon this information, we propose that the chemical abundance pattern observed in this star may be indicative of enrichment from a rapidly rotating progenitor.

Previous studies, such as those conducted by Meynet & Maeder (2002), Hirschi (2007), and Meynet et al. (2010), have revealed that rapid rotation in massive stars plays a pivotal role in facilitating the upward transport of processed materials from the star's inner regions to its surface. This leads to an enhancement of specific elements in the stellar atmosphere, notably nitrogen, sodium, and aluminium, which are derived from distinct processes, namely CNO processing, the Na-Ne cycle, and the Mg-Al cycle, respectively. A massive rapidly rotating star would have ultimately dispersed these elements into the interstellar medium via stellar winds and eventual supernovae, contributing to the chemical evolution of the galaxy.

Comparing 497519424 with other NEMP stars in the Milky Way, we see that out of the 11 such stars in Yong et al. (2021a), only two are also enhanced in both sodium and aluminium. This could indicate that the processes responsible for these stars do not significantly depend on the galactic environment, since it is seen in both the LMC and the Milky Way.

However, it is important to highlight that some models of rapidly rotating stars also typically yield higher quantities of s-process elements via the weak s-process (Pignatari et al. 2010; Cescutti & Chiappini 2014; Frischknecht et al. 2016). This expected enhancement is not detected in 497519424. This could stem from the extremely metal-poor nature of the progenitor star where the comparative lack of iron-peak seeds from which to generate the s-process elements may have hindered their formation.

In a more recent study by Choplin et al. (2018) of massive stars with [Fe/H] $= -1.8$, it was observed that non-rotating ($v/v_{crit} = 0$) and slow-rotating massive ($v/v_{crit} = 0.4$) stars exhibit significant [N/Fe] enhancements. However, this pattern is rarely observed in rapidly rotating massive stars ($v/v_{crit} = 0.7$), where only 1 out of 9 simulations (with different stellar masses) had enhanced [N/Fe]. Therefore, the high N, Na and Al in 497519424 suggest rotation in the progenitor star, but the lack of high Sr, Y and Zr indicates that there has not been substantial accompanying weak s-process enrichment (Pignatari et al. 2010).

500766372: Hypernova signature

The chemical abundance pattern observed in star 500766372 is characterised by low levels of scandium, yttrium, strontium, and barium, but a high zinc abundance. We propose that star was enriched with the nucleosynthetic products from a hypernova (Kobayashi et al. 2014).

Hypernovae are highly energetic supernovae resulting from the core collapse of massive stars. Compared to regular core-collapse supernovae, their significantly higher explosion energies are believed to lead to the production and ejection of large amounts of heavy elements. Studies on supernova nucleosynthesis, such as Nomoto et al. (2013), have shown that hypernovae are potential sites for the production of zinc, which can be efficiently synthesised in the outer layers of the exploding star and then expelled into the interstellar medium.

As a comparison, the EMP star SMSS J200322.54-114203.3 from Yong et al. (2021b) contains high zinc but not low scandium. It also exhibits substantial enhancement in the r-process elements which are hypothesized to originate in a magneto-rotational hypernova (Yong et al. 2021b). As a result, the enhanced zinc abundance together with the low scandium, strontium and barium abundances in 500766372 suggests that this star is not the result of a magneto-rotational hypernova event.

500287810: Spinstar signature

This star has the highest barium to europium ratio amongst our LMC sample ([Ba/Eu] > -0.3). It has fairly low abundances in all the neutron-capture elements ([Eu/Fe] < -0.45; [La/Fe] < -0.85) including those that can be made in the s-process ([Sr/Fe] $= -0.88$; [Ba/Fe] $= -0.76$). Thus, although it did not form sufficiently late for s-process enrichment by AGB stars to become important, based on the [Ba/Eu] limit, the low abundances for the neutron capture elements seem to originate from another type of neutron capture-process enrichment rather than an r-process one. One potential source is spinstars, which are thought to be a possible site for weak s-process enrichment at low metallicities (Cescutti & Chiappini 2014; Choplin & Hirschi 2020). We note that this process often produces low Sr and Ba abundances with a range of [Sr/Ba] ratios, including the solar [Sr/Ba] ratio observed in star 500287810.

A further important result for this star is its lack of r-process enrichment ([Eu/Fe] < -0.45) despite being the most metal-rich star in our sample. This probably suggests that r-process enrichment that happened after [Fe/H] ~ -3 was not spatially homogeneous across the entire LMC as it existed ~ 12 Gyr ago. Otherwise every

star above [Fe/H] ~ -3 would show some level of r-process enrichment as is seen in our two r-process enhanced stars and in those from the Reggiani et al. (2021) sample.

6.6 Summary

In this paper, we have presented abundance results, based on high-resolution spectra, for 7 metal-poor stars that are members of the Large Magellanic Cloud. Our analysis confirms that all 7 stars, including two extremely metal-poor (EMP) stars with [Fe/H] $\leq$ –3, are the most metal-poor stars discovered thus far in the Magellanic Clouds. Although their abundances and abundance ratios generally resemble those found in the Milky Way halo, our investigation reveals several key differences. Out of the seven stars in our sample, three stars potentially exhibit enrichment by rotating massive stars or hypernovae. Together with the results from Reggiani et al. (2021), the absence of r-process enhancement in stars with lower [Fe/H] values suggests a minimum delay timescale of $\sim$100 Myr for the neutron star binary merger process to generate substantial r-process enhancements in the LMC. Furthermore, the occurrence rates of r-I and r-II stars are statistically indistinguishable in the very and extremely metal-poor stars in our LMC sample and the Milky Way halo. However, the r-II star occurrence rate is potentially higher for the LMC when the stars from Reggiani et al. (2021) are added to the comparison sample. Ultimately, these results provide valuable insights into the earliest stages of star formation in the LMC and offer the first comprehensive information on extremely and very metal-poor stars in galaxies of this mass.

Table 6.3: Abundance table showing the abundance measurement for each star. The measurement uncertainties are given for each element.

SMSS DR3	[Fe/H] [Sc/Fe] [Y/Fe]	$[C/Fe]_{raw}$ [Ti I/Fe] [Zr/Fe]	$[C/Fe]_{corr}$ [Ti II/Fe] [Ba/Fe]	[N/Fe] [Cr/Fe] [La/Fe]	[O/Fe] [Mn/Fe] [Nd/Fe]	[Na/Fe] [Fe II/H] [Sm/Fe]	[Mg/Fe] [Co/Fe] [Eu/Fe]	[Al/Fe] [Ni/Fe] [Dy/Fe]	[Si/Fe] [Zn/Fe]	[Ca/Fe] [Sr/Fe]
500287810	-2.49 ± 0.11	-0.80 ± 0.15	-0.12 ± 0.15	< 0.50	0.85 ± 0.12	-0.06 ± 0.13	0.22 ± 0.06	-0.24 ± 0.19	0.29 ± 0.12	0.16 ± 0.05
	0.07 ± 0.19	-0.02 ± 0.08	0.12 ± 0.19	-0.31 ± 0.12	-0.42 ± 0.26	-2.73 ± 0.11	0.25 ± 0.17	-0.05 ± 0.05	0.00 ± 0.06	-0.88 ± 0.19
	-0.68 ± 0.23	-0.39 ± 0.07	-0.76 ± 0.19	< -0.85	< -0.65	....	< -0.45	< -0.40		
500382880	-2.65 ± 0.10	-0.60 ± 0.19	0.04 ± 0.19	< 0.5	1.10 ± 0.27	0.15 ± 0.12	0.24 ± 0.05	-0.07 ± 0.16	0.13 ± 0.13	0.26 ± 0.05
	0.30 ± 0.17	0.25 ± 0.05	0.39 ± 0.16	-0.24 ± 0.09	-0.31 ± 0.21	-2.61 ± 0.10	0.16 ± 0.11	-0.24 ± 0.17	0.10 ± 0.05	-0.08 ± 0.15
	-0.10 ± 0.16	0.23 ± 0.05	0.02 ± 0.17	0.28 ± 0.07	0.43 ± 0.08	0.60 ± 0.09	0.80 ± 0.08	0.85 ± 0.08		
497682788	-2.80 ± 0.10	-0.90 ± 0.13	-0.26 ± 0.13	< 0.70	1.05 ± 0.16	-0.03 ± 0.09	0.33 ± 0.08	-0.54 ± 0.15	0.53 ± 0.10	0.27 ± 0.08
	0.22 ± 0.18	0.15 ± 0.04	0.46 ± 0.22	-0.28 ± 0.05	-0.49 ± 0.17	-2.65 ± 0.10	0.14 ± 0.08	-0.11 ± 0.15	0.35 ± 0.04	-0.50 ± 0.18
	-0.23 ± 0.20	0.19 ± 0.05	0.08 ± 0.19	0.50 ± 0.06	0.73 ± 0.06	0.80 ± 0.08	1.03 ± 0.06	1.00 ± 0.08		
471915910	-2.90 ± 0.07	-0.35 ± 0.26	0.28 ± 0.26	< 0.90	....	0.15 ± 0.14	0.41 ± 0.06	-0.09 ± 0.20	0.66 ± 0.15	0.41 ± 0.06
	0.24 ± 0.16	0.30 ± 0.06	0.38 ± 0.16	-0.18 ± 0.08	-0.48 ± 0.18	-2.83 ± 0.07	0.23 ± 0.09	-0.19 ± 0.16	0.35 ± 0.11	-0.10 ± 0.18
	0.10 ± 0.18	0.26 ± 0.12	-0.40 ± 0.14	< -0.25	< -0.05	....	< 0.3	< 0.25		
500766372	-2.90 ± 0.08	-0.55 ± 0.27	0.04 ± 0.27	< 0.90	....	0.19 ± 0.09	-0.02 ± 0.09	-0.45 ± 0.14	0.50 ± 0.12	0.12 ± 0.08
	-0.30 ± 0.13	0.25 ± 0.06	0.22 ± 0.15	-0.17 ± 0.05	-0.07 ± 0.15	-2.82 ± 0.08	0.28 ± 0.07	0.09 ± 0.13	0.75 ± 0.04	-1.30 ± 0.12
	< -1.00	-0.33 ± 0.08	-1.21 ± 0.17	< -0.20	< 0.15	....	< -0.10	< -0.50		
497519424	-3.13 ± 0.08	0.00 ± 0.14	0.63 ± 0.14	1.70 ± 0.11	....	1.25 ± 0.15	0.43 ± 0.05	-0.10 ± 0.21	0.17 ± 0.19	0.30 ± 0.05
	0.22 ± 0.17	0.24 ± 0.04	0.50 ± 0.15	-0.33 ± 0.05	-0.84 ± 0.12	-3.06 ± 0.08	0.32 ± 0.09	-0.10 ± 0.24	0.35 ± 0.05	-0.59 ± 0.17
	-0.28 ± 0.20	0.15 ± 0.05	-0.70 ± 0.15	< -0.20	< 0.00	....	< 0.15	< 0.15		
499901368	-3.13 ± 0.09	-0.10 ± 0.23	0.51 ± 0.23	< 1.10	....	0.21 ± 0.05	0.34 ± 0.06	-0.42 ± 0.12	1.03 ± 0.07	0.25 ± 0.08
	0.24 ± 0.19	0.21 ± 0.11	0.26 ± 0.17	-0.18 ± 0.05	-0.10 ± 0.29	-3.14 ± 0.09	0.35 ± 0.04	-0.06 ± 0.19	0.40 ± 0.09	-0.55 ± 0.21
	-0.23 ± 0.16	0.14 ± 0.07	-0.85 ± 0.20	< 0.10	< 0.20	....	< 0.30	< 0.10		

6.7 Addendum - In response to comments by two of the thesis examiners; text is not in the published paper

The method of measuring statistical errors on elemental abundances via spectral synthesis involved estimating these errors by calculating the reciprocal of the signal-to-noise ratio (1/SNR) in the relevant spectral region. 1/SNR serves as the detection threshold, roughly equivalent to a 3-sigma detection level, as determined through comparison to equivalent width based uncertainties discussed in the text. Notably, measurement uncertainties were found to be negligible compared to those arising from uncertainties in stellar parameters based on the same tests, and as such, were not quantified. In cases where the central depth of the synthetic line was less than 1/SNR, we adopted an upper limit based on the abundance that yielded a spectral line of depth 1/SNR.

Regarding the derivation of abundances by generating synthetic spectra, I considered the presence of hyperfine splitting structure for the elements measured, including Sc, Mn, Co, Ba and Eu. Isotopic splitting was considered for Eu, but otherwise neglected for the other elements. Heavy elements where isotopic shifts are significant do not exhibit saturated lines in this work, and we therefore expect only minor effects of this omission. The only 2 elemental abundances affected by this error are C and N. I found that the abundances of C are underestimated as a result of not factoring in the proper 12C/13C isotopic ratios. This in turn overestimated the N abundances as well. While I acknowledge the technical error in the derived abundances of C and potentially N, it is unlikely that this will impact the conclusions drawn in the paper or my thesis.

Chapter 7

Summary and Conclusion

7.1 Summary of the 3 projects

The overall goal of this thesis has been to improve the current understanding of the LMC, the largest dwarf galaxy satellite of the Milky Way, by obtaining detailed abundance measurements for various elements in its stellar population, shedding light on its chemical composition and evolution. A key component of this has been the chemical abundance analysis of an intermediate-age LMC cluster to understand the multiple populations phenomenon in massive clusters, whose underlying cause remains a mystery. In Chapter 4, I present a search for multiple populations in the 1.95 Gyr old LMC star cluster NGC 1846, testing the 2 Gyr minimum threshold for massive clusters displaying chemical abundance variations. Our measurements rely on a combination of high and low-resolution VLT/FLAMES spectra, complemented by photometric data from HST. We have incorporated corrections for non-local thermodynamic equilibrium effects for elements such as O, Na, Mg, Si, Ca, Fe, and Ba. Our findings indicate the absence of evidence for multiple populations in this cluster, as demonstrated by the lack of any intrinsic star-to-star spread in the abundances of Na and O. We have established 95% confidence limits on the intrinsic dispersion for these elements, revealing values of ≤ 0.07 and ≤ 0.09 dex, respectively. Nevertheless, a notable spread in carbon abundances was detected, suggesting varying evolutionary mixing during the RGB phase that increases with luminosity. Additionally, the overall abundance patterns observed in NGC 1846 closely resemble those found in prior investigations of intermediate-age LMC star clusters and field stars.

In Chapter 5, I present a search for EMP stars in the LMC, crucial for unraveling insights into the earliest stars and the conditions during the initial phases of star formation in classical dwarf galaxies. By utilising data from SkyMapper DR3 and Gaia DR2, the study employed specific criteria to select EMP candidates based on photometric and kinematic information. Subsequently, low-resolution spectroscopic

observations using ANU 2.3/WiFeS confirmed the presence of seven stars with [Fe/H] $\leq$ –2.75, including two stars with [Fe/H] $\leq$ –3. The consistent radial velocities of these stars with the LMC's outer rotation curve firmly establish their membership within the LMC.

In Chapter 6, I examine the detailed chemical abundances of the seven LMC stars mentioned in the previous investigation. Using high-resolution UVES spectra, these stars are identified as the most metal-poor stars ever observed in the Magellanic Clouds. While their element abundance ratios generally resemble those of similar Milky Way halo stars, only two of the more metal-rich stars in the group show significant enhancement in the rapid neutron-capture process (r-process). The lack of r-process enrichment in stars with lower [Fe/H] values suggests that it takes at least approximately 100 Myr for the neutron star binary merger process to generate significant r-process enhancements in the LMC. Our findings also indicate that the occurrence rate of r-process enhancement in our sample of very and extremely metal-poor stars is comparable to that found in the Milky Way's halo, although the inclusion of stars from the Reggiani et al. (2021) sample suggests a potentially higher frequency of very high r-process enhanced stars in the LMC. Additionally, we observed that each star has a different chemical abundance pattern, indicating inhomogeneous mixing. Certain stars even exhibit interesting abundance patterns, hinting at diverse enrichment sources, including processes such as hypernovae and spinstars. Overall, our results provide insights into the early stages of star formation in the LMC, with potential implications for other galaxies of a similar mass as the LMC.

Together, these studies offer important insights into the chemical composition, evolutionary history, and initial star formation processes within the LMC, advancing our knowledge of stellar and galactic evolution.

7.2 Outlook

Previous research into multiple populations in intermediate-age clusters of comparable masses have yielded inconsistent outcomes. Mucciarelli et al. (2008), utilising VLT/UVES spectra on 4 clusters, did not reveal evident chemical inconsistencies in clusters spanning 1.5–2 Gyr in age. However, studies, like Saracino et al. (2020) and Kapse et al. (2022), have suggested the existence of possible multiple populations in clusters younger than 2 Gyr via VLT/MUSE spectra and HST photometry respectively. Recent work by Cadelano et al. (2022) have also revealed the possible presence of multiple populations in the form of nitrogen spreads through photometry

in main sequence stars within a cluster falling below the 2 Gyr threshold. However, as of now, there is no conclusive evidence indicating sodium variations in this cluster based on high-resolution spectroscopy. Our findings suggest the need for a much greater number of high-resolution spectroscopic analyses and precise age determinations of intermediate-age massive clusters ($M_{\text{present day}} > 10^{4.5}$solar masses) in the LMC and nearby dwarf galaxies. With the results presented by Salgado et al. (2022), there remain approximately 15 clusters yet to be observed with high-resolution spectroscopy. If we consider an observational program utilising VLT/FLAMES exclusively to target Na (via a single spectroscopic setting), observing one cluster per night would require a total of 15 nights to complete the dataset.

Given that the confidence limit on the intrinsic dispersion of sodium (≤ 0.07) closely matches the sodium variation presented by Saracino et al. (2020) within NGC1978 using stacked MUSE spectra, it would be interesting to perform a purely differential analysis on stars with similar luminosities in young/intermediate age clusters. This approach, akin to the methodology employed by Yong et al. (2013) for NGC 6752, aims to eliminate potential systematic errors, enabling us to highlight subtle differences in sodium abundances. Such an analysis is particularly important because previous studies suggest a correlation between the ranges of light-element variations and the age of the cluster (e.g., Martocchia et al. 2018). Therefore, given the expected minimal sodium variations at young ages, conducting a nuanced analysis becomes crucial.

Concurrently, emerging technology (e.g. 4-metre Multi-Object Spectrograph Telescope (4MOST), ESO's Extremely Large Telescope (ELT)) will also significantly contribute to this cause. In particular, 4MOST's One Thousand and One Magellanic Fields (1001MC) survey will obtain high-res spectra for hundreds of thousands of RGB stars in the Magellanic Clouds, including in clusters (Cioni et al. 2019). These large telescopes are also likely well-suited for effectively studying massive clusters located in more distant galaxies like the Andromeda Galaxy. This will significantly aid in confirming the presence of a minimum 2 Gyr age limit for massive clusters.

Moreover, several potentially young to intermediate-age massive clusters have been identified within the Milky Way over the past decade (Davies et al. 2011; Borissova et al. 2018). These clusters present a compelling opportunity to complement the extragalactic intermediate-age massive cluster sample, offering a valuable control within our own galactic environment. Given that they are located within the heavily obscured Galactic plane, analysis using optical spectra will not be possible. Hence, upcoming technological advancements such as the Giant Magellan Telescope Near

Infrared Spectrograph (GMTNIRS) hold significant promise for enhancing our understanding of these massive star clusters.

On the other hand, the study of EMP stars in the LMC and nearby dwarf galaxies holds promising prospects, particularly with the advent of advanced technologies. Ongoing and forthcoming advancements, facilitated by instruments such as SkyMapper, 4MOST and the ELT, are poised to revolutionise our capability to discover and analyse EMP stars. As mentioned earlier, 4MOST's comprehensive survey of the Magellanic Clouds at both high and low resolution is also expected to significantly contribute to our understanding of the metal-poor population in these dwarf galaxies (Cioni et al. 2019). ESO's ELT, scheduled to be operational in 2028, also stands as a key player in this endeavour. One of its proposed instruments that will play a big part in this is ANDES, a modular fibre-fed cross-dispersed echelle spectrograph featuring two ultra-stable spectral arms – visual and near-infrared. These arms collectively cover a simultaneous spectral range from 0.4 to 1.8 μm, achieving a remarkable spectral resolving power of R$\sim$100,000 for a single object (Marconi et al. 2022). ANDES will further enhance its capabilities by incorporating a single-conjugate adaptive optics (SCAO) module. This allows for the correction of atmospheric turbulence-induced blurring effects, ensuring precise observations across the entire spectral range. With these features, we will be able to get better throughput and spatial resolution in crowded areas (e.g. inner regions of massive clusters and MCs). This will allow us to chemically characterise the most metal-poor stars in the LMC with better accuracy and precision, going significantly fainter than what is possible with VLT/UVES.

Anticipating further discoveries of EMP stars in the LMC, the exploration and analysis of more LMC stars will notably increase the sample size of the metallicity distribution function at the lower end. This can tell us directly about the first stages of inhomogeneous chemical enrichment in this dwarf galaxy. At sufficiently low metallicities, stars have been enriched by individual supernovae. Thus, finding and analysing those stars allow us to understand the LMC formation history. Moreover, a larger EMP sample size could help confirm or refute the rarity of stars not enhanced by r-process elements at [Fe/H] ≤ -2.9, shedding light on the prevalence and the timescale of neutron star binary mergers. Furthermore, a more extensive EMP sample could also help pinpoint the exact location of the alpha-knee in the LMC. As our initial findings suggest a similarity between the metallicity at which the alpha-knee appears and that linked to r-process enhancement, determining the alpha-knee location can give us clues as to how the different nucleosynthetic processes might be connected to the star formation history of the system. Finally,

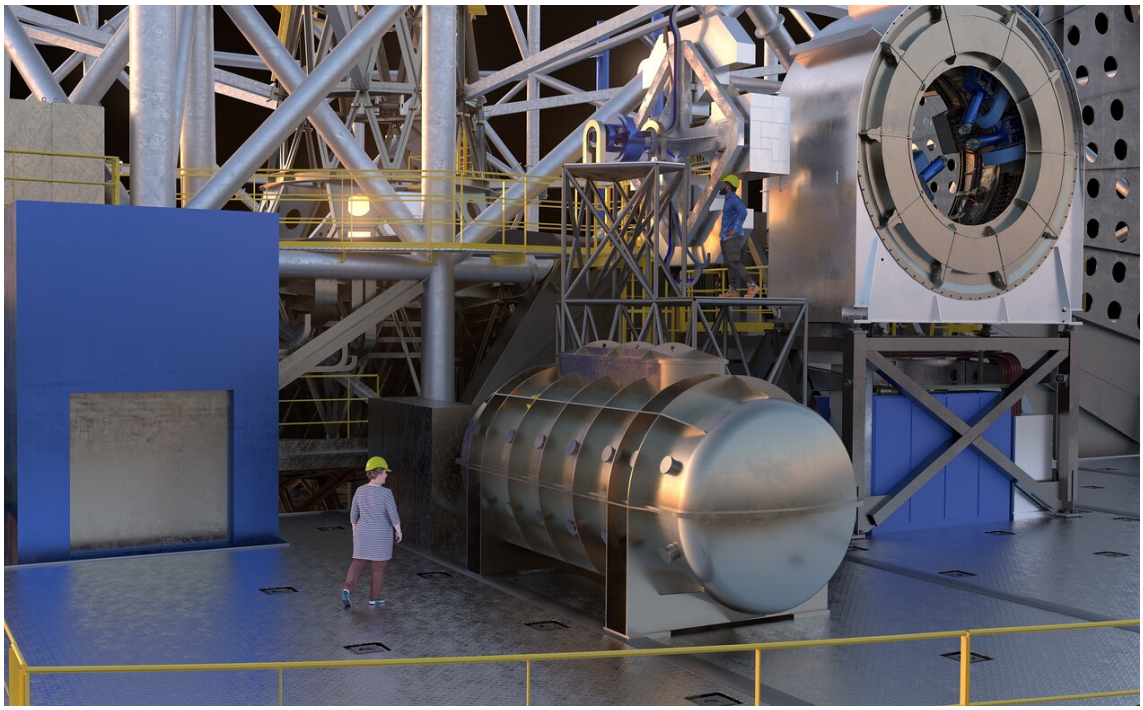

Figure 7.1: An artist's impression of the high-resolution ELT instrument ANDES. Image credit: ESO

investigating the Small Magellanic Cloud (SMC) could prove highly beneficial, serving as a valuable comparison object to enhance our understanding of the broader star-formation history in these dwarf galaxies. This holistic approach not only contributes to understanding the distinctive aspects of the Magellanic Clouds, but also sheds light on the broader cosmic narrative, addressing fundamental questions about the mass-dependent evolution of classical dwarf galaxies and Ultra-Faint Dwarfs in our universe.

Bibliography

Alonso A., Arribas S., Martínez-Roger C., 1999, Astronomy and Astrophysics Supplement Series, 140, 261

Amarsi A. M., et al., 2020, Astronomy & Astrophysics, 642, A62

Amarsi A., Liljegren S., Nissen P., 2022, Astronomy & Astrophysics, 668, A68

Asplund M., Grevesse N., Sauval A. J., Scott P., 2009, ARA&A, 47, 481

Barklem P. S., et al., 2005, A&A, 439, 129

Bastian N., Lardo C., 2018, ARA&A, 56, 83

Bekki K., Couch W. J., Beasley M. A., Forbes D. A., Chiba M., Da Costa G. S., 2004, ApJ, 610, L93

Belczynski K., et al., 2018, A&A, 615, A91

Belokurov V., Koposov S. E., 2016, MNRAS, 456, 602

Bennett M., Bovy J., Hunt J. A. S., 2022, ApJ, 927, 131

Besla G., Kallivayalil N., Hernquist L., Robertson B., Cox T. J., van der Marel R. P., Alcock C., 2007, ApJ, 668, 949

Besla G., Kallivayalil N., Hernquist L., van der Marel R. P., Cox T. J., Kereš D., 2012, MNRAS, 421, 2109

Bessell M. S., 2007, PASP, 119, 605

Blecha A., Cayatte V., North P., Royer F., Simond G., 2000, in Iye M., Moorwood A. F., eds, Society of Photo-Optical Instrumentation Engineers (SPIE) Conference Series Vol. 4008, Optical and IR Telescope Instrumentation and Detectors. pp 467–474, doi:10.1117/12.395507

de Boer T. J. L., et al., 2012, A&A, 539, A103

de Boer T. J. L., Belokurov V., Beers T. C., Lee Y. S., 2014a, MNRAS, 443, 658

de Boer T. J. L., Tolstoy E., Lemasle B., Saha A., Olszewski E. W., Mateo M., Irwin M. J., Battaglia G., 2014b, A&A, 572, A10

Bohlin R. C., Gordon K. D., Tremblay P. E., 2014, PASP, 126, 711

Borissova J., et al., 2018, MNRAS, 481, 3902

Brooke J. S. A., Ram R. S., Western C. M., Li G., Schwenke D. W., Bernath P. F., 2014, The Astrophysical Journal Supplement Series, 210, 23

Cadelano M., Dalessandro E., Salaris M., Bastian N., Mucciarelli A., Saracino S., Martocchia S., Cabrera-Ziri I., 2022, ApJ, 924, L2

Carretta E., et al., 2009, A&A, 505, 117

Casagrande L., et al., 2021, MNRAS, 507, 2684

Castelli F., Kurucz R. L., 2003, in Piskunov N., Weiss W. W., Gray D. F., eds, Journal of Physics Conference Series Vol. 210, Modelling of Stellar Atmospheres. p. A20 (arXiv:astro-ph/0405087), doi:10.48550/arXiv.astro-ph/0405087

Cayrel R., 1988, in Cayrel de Strobel G., Spite M., eds, Vol. 132, The Impact of Very High S/N Spectroscopy on Stellar Physics. p. 345

Cayrel R., et al., 2004, A&A, 416, 1117

Cescutti G., Chiappini C., 2014, A&A, 565, A51

Chan T. K., Kereš D., Oñorbe J., Hopkins P. F., Muratov A. L., Faucher-Giguère C. A., Quataert E., 2015, MNRAS, 454, 2981

Chanamé J., Pinsonneault M., Terndrup D. M., 2005, ApJ, 631, 540

Chilingarian I. V., Asa'd R., 2018, ApJ, 858, 63

Chiti A., Frebel A., Ji A. P., Jerjen H., Kim D., Norris J. E., 2018, ApJ, 857, 74

Chiti A., Hansen K. Y., Frebel A., 2020, ApJ, 901, 164

Choplin A., Hirschi R., 2020, in Journal of Physics Conference Series. p. 012006 (arXiv:2001.02341), doi:10.1088/1742-6596/1668/1/012006

Choplin A., Hirschi R., Meynet G., Ekström S., Chiappini C., Laird A., 2018, A&A, 618, A133

Christlieb N., Schörck T., Frebel A., Beers T. C., Wisotzki L., Reimers D., 2008, A&A, 484, 721

Cioni M. R. L., 2018, Mem. Soc. Astron. Italiana, 89, 35

Cioni M. . R. L., et al., 2019, The Messenger, 175, 54

Conroy C., Spergel D. N., 2011, ApJ, 726, 36

Cottrell P. L., Da Costa G. S., 1981, ApJ, 245, L79

Cullinane L. R., Mackey A. D., Da Costa G. S., Erkal D., Koposov S. E., Belokurov V., 2022, MNRAS, 512, 4798

D'Ercole A., Vesperini E., D'Antona F., McMillan S. L. W., Recchi S., 2008, MNRAS, 391, 825

Da Costa G. S., Held E. V., Saviane I., Gullieuszik M., 2009, ApJ, 705, 1481

Da Costa G. S., et al., 2019, MNRAS, 489, 5900

Da Costa G. S., Bessell M. S., Nordlander T., Hughes A. C. N., Buder S., Mackey A. D., Spitler L. R., Zucker D. B., 2023, MNRAS, 520, 917

Davies B., Bastian N., Gieles M., Seth A. C., Mengel S., Konstantopoulos I. S., 2011, MNRAS, 411, 1386

De Grijs R., Bono G., 2015, AJ, 149, 179

De Marchi G., et al., 2011, ApJ, 739, 27

Dekker H., D'Odorico S., Kaufer A., Delabre B., Kotzlowski H., 2000, in Iye M., Moorwood A. F., eds, Society of Photo-Optical Instrumentation Engineers (SPIE) Conference Series Vol. 4008, Optical and IR Telescope Instrumentation and Detectors. pp 534–545, doi:10.1117/12.395512

Dopita M., et al., 2010, Ap&SS, 327, 245

Dotter A., Chaboyer B., Jevremović D., Kostov V., Baron E., Ferguson J. W., 2008, ApJS, 178, 89

Eggen O. J., Lynden-Bell D., Sandage A. R., 1962, ApJ, 136, 748

Emptage B., 2023, PhD thesis, University of Tasmania, Australia, doi:10.25959/100.00029564, `https://figshare.utas.edu.au/articles/thesis/A_survey_for_stellar_relics_of_galaxy_formation_in_the_large_Magellanic_cloud/23252945`

Ernandes H., Castro M. J., Barbuy B., Spite M., Hill V., Castilho B., Evans C. J., 2023, MNRAS,

Forbes D. A., et al., 2018, Proceedings of the Royal Society of London Series A, 474, 20170616

Foreman-Mackey D., Hogg D. W., Lang D., Goodman J., 2013, Publications of the Astronomical Society of the Pacific, 125, 306

Frebel A., Norris J. E., 2015, ARA&A, 53, 631

Frebel A., et al., 2006, ApJ, 652, 1585

Frebel A., Kirby E. N., Simon J. D., 2010, Nature, 464, 72

Freeman K. C., Rodgers A. W., 1975, ApJ, 201, L71

Frischknecht U., et al., 2016, MNRAS, 456, 1803

Gaia Collaboration et al., 2018a, A&A, 616, A1

Gaia Collaboration et al., 2018b, A&A, 616, A12

Gaia Collaboration et al., 2021, A&A, 649, A1

Gardiner L. T., Noguchi M., 1996, MNRAS, 278, 191

Goudfrooij P., Puzia T. H., Kozhurina-Platais V., Chandar R., 2009, AJ, 137, 4988

Goudfrooij P., et al., 2014, ApJ, 797, 35

Gratton R. G., Carretta E., Bragaglia A., 2012, A&A Rev., 20, 50

Gratton R., Bragaglia A., Carretta E., D'Orazi V., Lucatello S., Sollima A., 2019, A&A Rev., 27, 8

Grocholski A. J., Cole A. A., Sarajedini A., Geisler D., Smith V. V., 2006, AJ, 132, 1630

Gustafsson B., Edvardsson B., Eriksson K., Jørgensen U. G., Nordlund Å., Plez B., 2008, Astronomy & Astrophysics, 486, 951

Hansen C. J., Bergemann M., Cescutti G., François P., Arcones A., Karakas A. I., Lind K., Chiappini C., 2013, A&A, 551, A57

Harris W. E., 1996, AJ, 112, 1487

Helmi A., et al., 2006, ApJ, 651, L121

Hinkle K., Wallace L., Valenti J., Harmer D., 2000, Visible and Near Infrared Atlas of the Arcturus Spectrum 3727-9300 A

Hirschi R., 2007, A&A, 461, 571

Hollyhead K., et al., 2017, MNRAS, 465, L39

Hollyhead K., et al., 2018, MNRAS, 476, 114

Hollyhead K., et al., 2019, MNRAS, 484, 4718

Ibata R. A., Gilmore G., Irwin M. J., 1994, Nature, 370, 194

Ishigaki M. N., Aoki W., Arimoto N., Okamoto S., 2014, A&A, 562, A146

Jablonka P., et al., 2015, A&A, 583, A67

Jacobson H. R., et al., 2015, ApJ, 807, 171

Ji A. P., Frebel A., Simon J. D., Chiti A., 2016, ApJ, 830, 93

Ji A. P., Simon J. D., Frebel A., Venn K. A., Hansen T. T., 2019, ApJ, 870, 83

Ji A. P., et al., 2023, AJ, 165, 100

Johnson J. A., Herwig F., Beers T. C., Christlieb N., 2007, ApJ, 658, 1203

Johnson L. C., et al., 2017, ApJ, 839, 78

Jönsson H., et al., 2020, AJ, 160, 120

Kallivayalil N., van der Marel R. P., Alcock C., 2006, ApJ, 652, 1213

Kallivayalil N., van der Marel R. P., Besla G., Anderson J., Alcock C., 2013, ApJ, 764, 161

Kallivayalil N., et al., 2018, ApJ, 867, 19

Kamann S., et al., 2020, MNRAS, 492, 2177

Kapse S., de Grijs R., Kamath D., Zucker D. B., 2022, ApJ, 927, L10

Karakas A., Lattanzio J. C., 2007, PASA, 24, 103

Karakas A. I., Lattanzio J. C., 2014, Publications of the Astronomical Society of Australia, 31

Keller S. C., et al., 2007, PASA, 24, 1

Keller S. C., et al., 2014, Nature, 506, 463

Kirby E. N., Simon J. D., Geha M., Guhathakurta P., Frebel A., 2008, ApJ, 685, L43

Kobayashi C., Ishigaki M. N., Tominaga N., Nomoto K., 2014, ApJ, 785, L5

Kobayashi C., Leung S.-C., Nomoto K., 2020a, ApJ, 895, 138

Kobayashi C., Karakas A. I., Lugaro M., 2020b, ApJ, 900, 179

Kobayashi C., et al., 2023, ApJ, 943, L12

Kovacs G., 2000, Astronomy and Astrophysics, 363, 19

Kraft R. P., 1979, ARA&A, 17, 309

Krause M. G. H., Charbonnel C., Bastian N., Diehl R., 2016, A&A, 587, A53

Law D. R., Majewski S. R., 2010, ApJ, 714, 229

Legnardi M. V., et al., 2022, MNRAS, 513, 735

Lucchesi R., et al., 2020, A&A, 644, A75

Mackey A. D., Broby Nielsen P., Ferguson A. M. N., Richardson J. C., 2008, ApJ, 681, L17

Mackey A. D., Da Costa G. S., Ferguson A. M. N., Yong D., 2013, ApJ, 762, 65

Majewski S. R., Patterson R. J., Dinescu D. I., Johnson W. Y., Ostheimer J. C., Kunkel W. E., Palma C., 2000, in Noels A., Magain P., Caro D., Jehin E., Parmentier G., Thoul A. A., eds, Liege International Astrophysical Colloquia Vol. 35, Liege International Astrophysical Colloquia. p. 619 (arXiv:astro-ph/9910278), doi:10.48550/arXiv.astro-ph/9910278

Mamajek E. E., et al., 2015, IAU 2015 Resolution B2 on Recommended Zero Points for the Absolute and Apparent Bolometric Magnitude Scales, doi:10.48550/ARXIV.1510.06262, https://arxiv.org/abs/1510.06262

Marconi A., et al., 2022, in Evans C. J., Bryant J. J., Motohara K., eds, Society of Photo-Optical Instrumentation Engineers (SPIE) Conference Series Vol. 12184, Ground-based and Airborne Instrumentation for Astronomy IX. p. 1218424, doi:10.1117/12.2628689

van der Marel R. P., Alves D. R., Hardy E., Suntzeff N. B., 2002, AJ, 124, 2639

Marino A. F., et al., 2012, A&A, 541, A15

Marino A. F., et al., 2019, MNRAS, 485, 5153

Martínez-Barbosa C. A., Casas R. A., 2011, in Revista Mexicana de Astronomia y Astrofisica Conference Series. pp 68–69

Martocchia S., et al., 2017, MNRAS, 468, 3150

Martocchia S., et al., 2018, MNRAS, 473, 2688

Martocchia S., et al., 2019, MNRAS, 487, 5324

Mashonkina L., Christlieb N., 2014, A&A, 565, A123

Mashonkina L., Jablonka P., Sitnova T., Pakhomov Y., North P., 2017, A&A, 608, A89

Masseron T., et al., 2014, Astronomy and Astrophysics, 571, A47

McAlpine S., et al., 2016, Astronomy and Computing, 15, 72

McConnachie A. W., 2012, AJ, 144, 4

McConnachie A. W., et al., 2018, ApJ, 868, 55

McKenzie M., et al., 2022, MNRAS, 516, 3515

Meynet G., Maeder A., 2002, A&A, 390, 561

Meynet G., Hirschi R., Ekstrom S., Maeder A., Georgy C., Eggenberger P., Chiappini C., 2010, A&A, 521, A30

Milone A. P., Bedin L. R., Piotto G., Anderson J., 2009, A&A, 497, 755

Milone A. P., et al., 2012, ApJ, 744, 58

Milone A. P., et al., 2017, MNRAS, 464, 3636

Milone A. P., et al., 2018, MNRAS, 481, 5098

Milone A. P., et al., 2019, MNRAS, 484, 4046

Mucciarelli A., Carretta E., Origlia L., Ferraro F. R., 2008, AJ, 136, 375

Muggeo V., 2003, Statistics in medicine, 22, 3055

Neijssel C. J., et al., 2019, MNRAS, 490, 3740

Nelson D., et al., 2015, Astronomy and Computing, 13, 12

Nidever D. L., Majewski S. R., Butler Burton W., Nigra L., 2010, ApJ, 723, 1618

Nidever D. L., et al., 2017, AJ, 154, 199

Nidever D. L., et al., 2020, ApJ, 895, 88

Niederhofer F., et al., 2017, MNRAS, 465, 4159

Nomoto K., Kobayashi C., Tominaga N., 2013, ARA&A, 51, 457

Nordlander T., et al., 2019, MNRAS, 488, L109

Norris J., 1981, ApJ, 248, 177

Norris J. E., 2004, ApJ, 612, L25

Norris J. E., Da Costa G. S., 1995, ApJ, 447, 680

Norris J., Freeman K. C., 1983, ApJ, 266, 130

Norris J. E., et al., 2013, ApJ, 762, 28

Norris J. E., Yong D., Venn K. A., Gilmore G., Casagrande L., Dotter A., 2017, ApJS, 230, 28

Oh W. S., Nordlander T., Da Costa G. S., Bessell M. S., Mackey A. D., 2023, MNRAS, 524, 577

Onken C. A., et al., 2019, PASA, 36, e033

Osborn W., 1971, The Observatory, 91, 223

Peng E. W., et al., 2008, ApJ, 681, 197

Pfeffer J. L., Trujillo-Gomez S., Kruijssen J. M. D., Crain R. A., Hughes M. E., Reina-Campos M., Bastian N., 2020, MNRAS, 499, 4863

Pignatari M., Gallino R., Heil M., Wiescher M., Käppeler F., Herwig F., Bisterzo S., 2010, ApJ, 710, 1557

Pilgrim C., 2021, Journal of Open Source Software, 6, 3859

Piotto G., et al., 2005, ApJ, 621, 777

Piotto G., et al., 2015, AJ, 149, 91

Piskunov N., Valenti J. A., 2017, Astronomy & Astrophysics, 597, A16

Placco V. M., Frebel A., Beers T. C., Stancliffe R. J., 2014, ApJ, 797, 21

Plez B., 2012, Turbospectrum: Code for spectral synthesis, Astrophysics Source Code Library, record ascl:1205.004 (ascl:1205.004)

Portegies Zwart S. F., McMillan S. L. W., Gieles M., 2010, ARA&A, 48, 431

Primack J. R., 1984, in Particles and Gravity. pp 175–190

Ramírez I., Allende Prieto C., 2011, ApJ, 743, 135

Reggiani H., Schlaufman K. C., Casey A. R., Simon J. D., Ji A. P., 2021, AJ, 162, 229

Renzini A., et al., 2015, MNRAS, 454, 4197

Ryabchikova T., Piskunov N., Kurucz R. L., Stempels H. C., Heiter U., Pakhomov Y., Barklem P. S., 2015, Physica Scripta, 90, 054005

Sakari C. M., 2019, The Globular Star Clusters of the Andromeda Galaxy, doi:10.1088/2053-2571/ab39de.

Salgado C., Da Costa G. S., Yong D., Salinas R., Norris J. E., Mackey A. D., Marino A. F., Milone A. P., 2022, MNRAS, 515, 2511

Saracino S., et al., 2020, MNRAS, 498, 4472

Searle L., Zinn R., 1978, ApJ, 225, 357

Shetrone M., Venn K. A., Tolstoy E., Primas F., Hill V., Kaufer A., 2003, AJ, 125, 684

Simmerer J., Sneden C., Cowan J. J., Collier J., Woolf V. M., Lawler J. E., 2004, ApJ, 617, 1091

Simon J. D., 2019, ARA&A, 57, 375

Skowron D. M., et al., 2021, ApJS, 252, 23

Skúladóttir Á., Hansen C. J., Salvadori S., Choplin A., 2019, A&A, 631, A171

Skúladóttir Á., et al., 2021, ApJ, 915, L30

Skúladóttir Á., et al., 2023, The Messenger, 190, 19

Sneden C., Cowan J. J., 2003, Science, 299, 70

Sneden C., Lucatello S., Ram R. S., Brooke J. S. A., Bernath P., 2014, The Astrophysical Journal Supplement Series, 214, 26

Song Y.-Y., Mateo M., Mackey A. D., Olszewski E. W., Roederer I. U., Walker M. G., Bailey J. I., 2019, MNRAS, 490, 385

Spite M., Spite F., François P., Bonifacio P., Caffau E., Salvadori S., 2018, A&A, 617, A56

Starkenburg E., et al., 2010, A&A, 513, A34

Starkenburg E., et al., 2013, A&A, 549, A88

Starkenburg E., et al., 2017, MNRAS, 471, 2587

Van der Swaelmen M., Hill V., Primas F., Cole A. A., 2013, A&A, 560, A44

Tafelmeyer M., et al., 2010, A&A, 524, A58

Vasiliev E., 2023, MNRAS,

Venn K. A., et al., 2012, ApJ, 751, 102

Villanova S., et al., 2007, ApJ, 663, 296

White S. D. M., Frenk C. S., 1991, ApJ, 379, 52

White S. D. M., Rees M. J., 1978, MNRAS, 183, 341

Williams B. F., Dalcanton J. J., Dolphin A. E., Holtzman J., Sarajedini A., 2009, ApJ, 695, L15

Wolf C., et al., 2018, PASA, 35, e010

Worley C. C., Cottrell P. L., Freeman K. C., Wylie-de Boer E. C., 2009, MNRAS, 400, 1039

Yong D., et al., 2013, ApJ, 762, 26

Yong D., et al., 2021a, MNRAS, 507, 4102

Yong D., et al., 2021b, Nature, 595, 223

Zivick P., et al., 2018, ApJ, 864, 55